An Investigation into the Mass Dependence of Photonuclear Pion Production

Thesis

Submitted by

Douglas Johnstone

for the degree of

Doctor of Philosophy

Department of Physics and Astronomy
University of Edinburgh
1995

Abstract

Measurements of the (γ,π^+n) reaction have been carried out using ^{6}Li, ^{12}C and ^{40}Ca as targets. This work is part of a series of experiments conducted by Edinburgh University in collaboration with the Universities of Glasgow and Tübingen. The experiment was carried out using the 855 MeV MAMI-B electron accelerator at the Institut für Kernphysik, Mainz.

The 855 MeV continuous electron beam was directed onto a 4 μm Nickel radiator producing bremsstrahlung photons which were tagged with a resolution of 2 MeV using a spectrometer. These photons were made to impinge on the target and two detector arrays were used to detect reaction products. PiP, a plastic scintillator hodoscope, was used to detect positive pions; and TOF, a time-of-flight array, was used to detect the neutrons. PiP covered an angular range of $50° < \theta_\pi < 130°$, $-20° < \phi_\pi < 20°$ and an energy range of 30 MeV $< T_\pi <$ 180 MeV. TOF covered an angular range of $10° < \theta_n < 150°$, $160° < \phi_n < 200°$ and had a lower energy limit of $T_n = 30$ MeV. Data were obtained for the photon energy range 240 MeV $< E_\gamma <$ 400 MeV. The overall missing energy resolution of the experiment was $\sim$ 15 MeV.

The data are presented as double differential cross-sections against pion energy. They are compared to a theoretical code developed by Oset *et al.* Agreement between experiment and theory is good at low values of E_γ and low target mass, A, but divergences occur for both increasing E_γ and increasing A. Possible reasons for these results are presented and future work in both theory and experiment is suggested.

Declaration

The data presented in this thesis were obtained in experiments carried out by the Edinburgh University Nuclear Physics group in collaboration with the Universities of Glasgow and Tübingen at the Institut für Kernphysik, Mainz. I participated fully in all aspects of the preparation and execution of the experiment. The data analysis and interpretation is my own work. This thesis has been written by myself.

Acknowledgements

I would like to thank all the members of the Edinburgh Nuclear Physics group who have provided help and support over the last three years. I am particularly grateful to my supervisor Derek Branford for his guidance and encouragement. A special thanks must go to John MacKenzie without whom this thesis would never have happened. Thanks also to Carlos Bain and Jim MacIntosh for making the work bearable.

The experiments have been performed by a large collaboration, and I thank everyone involved from the Universities of Glasgow and Tübingen, as well as everyone at the Institut für Kernphysik at Mainz. The work has been made possible by the financial support of EPSRC.

Finally and most importantly, thanks to all my friends and family for helping me keep my work in perspective.

“ If you steal from one author, it’s plagiarism; if you steal from many, it’s research.”

Wilson Mizner

Contents

List of Figures

Chapter 1

Introduction

1.1 General Remarks

The atomic nucleus is a highly complex system. Conventionally, it is viewed as consisting of neutrons and protons. These two types of nucleons are held together in the nucleus by the strong nuclear interaction. This interaction is generally thought to occur by the exchange of virtual mesons within the nucleus.

Nucleons and mesons possess a sub-structure of their own, namely quarks. Quark interactions are dealt with in the theory of Quantum Chromodynamics (QCD). In principle, a description of nuclei could be achieved using QCD, but in practice the theory is mainly intractable mathematically, and a quark-based theory of complex nuclei is, to say the least, unlikely.

As a result of this, the nuclear physics community has turned to the concept of nuclear models. An early and very successful nuclear model is the Shell Model. This is analogous to Bohr's use of a shell model to describe atomic behaviour. In the nuclear shell model, protons and neutrons move independently in a mean field potential which is generated by the other nucleons. This, combined with the inclusion of a strong spin-orbit interaction accounts well for many nuclear properties and reactions.

At a glance however, the Shell Model would appear to be an inappropriate model to use for nuclei. Unlike the particles in Bohr's atomic shell model, the nucleons interact through the strong interaction. You would therefore expect a lot of nucleon-nucleon scattering within the nucleus. However this scattering is considerably subdued by two factors. Firstly, the short range nature of the nucleon-nucleon interaction reduces the possibility of an interaction taking place. Secondly, the Pauli Exclusion Principle greatly reduces the number of final states a nucleon can scatter into.

In contrast to this approach, more recent theoretical work has been carried out in the study of microscopic models of the nucleus. This has been done to try and discover more about the intrinsic dynamics of the nucleon-nucleon interaction within nuclei. Such microscopic models are based on realistic nucleon-nucleon potentials, and can include meson exchange currents explicitly. This helps to describe how pions, other mesons and isobars (especially the Δ (1232 MeV)) propagate inside the nucleus. These all play important roles in reaction mechanisms at intermediate energies.

It is at such energies that the current experiments have been carried out. The subject of this thesis is an examination of a photopion production experiment on various nuclei. The real photons used for this study make an excellent probe of the nucleus since the interaction is electromagnetic and well understood. Also, unlike the hadronic interaction, they probe the whole nuclear volume, not just the surface.

The remainder of this chapter contains a review of previous experimental work in this field along with a description of recent theoretical advances and a brief description of the current experiments in this context.

1.2 The Interaction of Photons with Nuclei

As briefly mentioned earlier, the photon makes an excellent probe of the nucleus. The electromagnetic interaction between photon and nucleus is well understood through the theory of Quantum Electrodynamics (QED) which should reduce uncertainty in the reaction analysis. The relatively weak nature of the interaction also enables the photon to probe the entire nucleus unlike hadronic probes (protons, pions etc.) which are dominated by surface absorption on the nucleus. Furthermore, this weakness of the interaction reduces the chances of initial state interactions for the photon, and its localisation means it can probe the few-particle structure of the nucleus well. The main disadvantage of using photons as probes is that the reaction cross-sections are low, and therefore long counting times are required to obtain sufficiently good statistics and ensure a useful data set.

Since the photon can probe the whole nucleus, it can "see" not only independent nucleons, but also virtual mesons and nuclear isobars or resonances all of which are interacting. This leads to a complicated mathematical treatment. The interaction of the photon with the nucleus can be represented by an operator such as:-

$$\mathcal{H} = \int \vec{j}(\vec{r},t) \cdot \vec{A}(\vec{r},t) d\vec{r} \tag{1.1}$$

where $\vec{A}(\vec{r},t)$ is the electromagnetic potential and $\vec{j}(\vec{r},t)$ represents the nuclear current, which can be seen as the sum of one-body and many-body terms, where the many-body terms can be brought together in a single exchange term. Thus, photon absorption experiments are used to try and shed some light on this nuclear current, and implicitly on nuclear dynamics.

Having said this, the way in which photons interact with nuclei depends greatly on the photon energy. Figure 1.1 shows the total photoabsorption cross-section per nucleon for a wide range of photon energies. This graph can be (and is) nominally split up into three rough regions. Basically, the photon can be thought of as "seeing" and interacting with an object of comparable size to its own wavelength. Thus at low energies (say a few 10s of MeV), the photon sees the nucleus as a single body, and this region is well described by collective excitations. At the other extreme (a few GeV), the photon can be thought of as interacting with the quark sub-structure of nucleons. It is the region in between we are interested in. At 100 MeV $< E_\gamma <$ 1 GeV ("intermediate energies") the wavelength of the photon is such that it probes single nucleons and small clusters of nucleons.

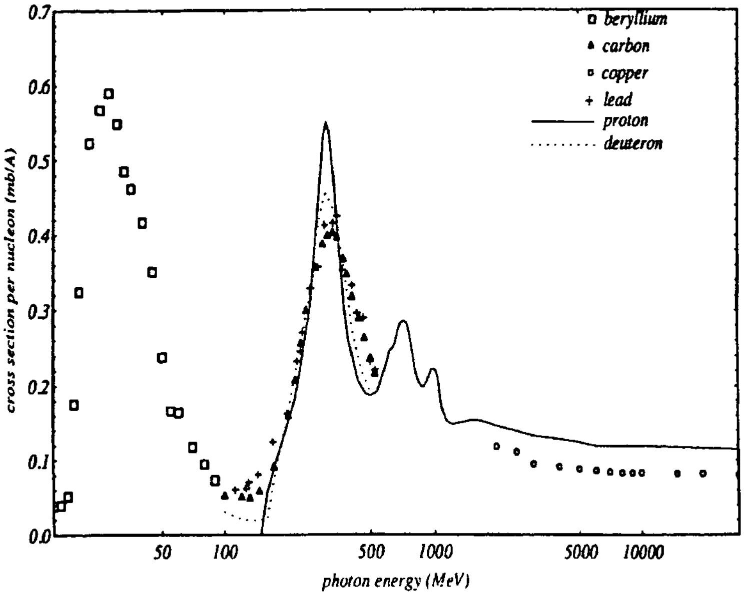

Figure 1.1: *Total photoabsorption cross-section*

Principally the photon can undergo one body or two body absorption. One body absorption is when the photon is absorbed onto a single nucleon, with the rest of the nucleus a spectator. In two body absorption the photon is in some way absorbed onto a correlated pair of nucleons, and virtual meson exchange can occur here. This is known as the Quasi-Deuteron (QD) model due to the similarity of the kinematics with that of photoabsorption on Deuterium. QD absorption is more common at lower photon energies within the intermediate range because the high momentum mismatch means single nucleon knockout is suppressed. However, at higher energies the photon can be absorbed by a single nucleon which could then emit a pion. It can also cause the nucleon to excite, creating the $\Delta(1232)$ resonance which can decay into a pion and a nucleon. In these ways, a real pion can be emitted from the nucleus. This has led to the Quasi-Free Pion Production (QFPP) model.

Some of the one and two body terms involved are shown graphically in figure 1.2. There will be further discussion of both the QD and QFPP models later in this chapter, and a description of how each has been used as building blocks for theoretical work. It is hoped that the current experiments which look at various exclusive photoabsorption experiments (emission of different combinations of nucleons and pions), can give an insight into the relative importance of one body and two body photoabsorption on nuclei.

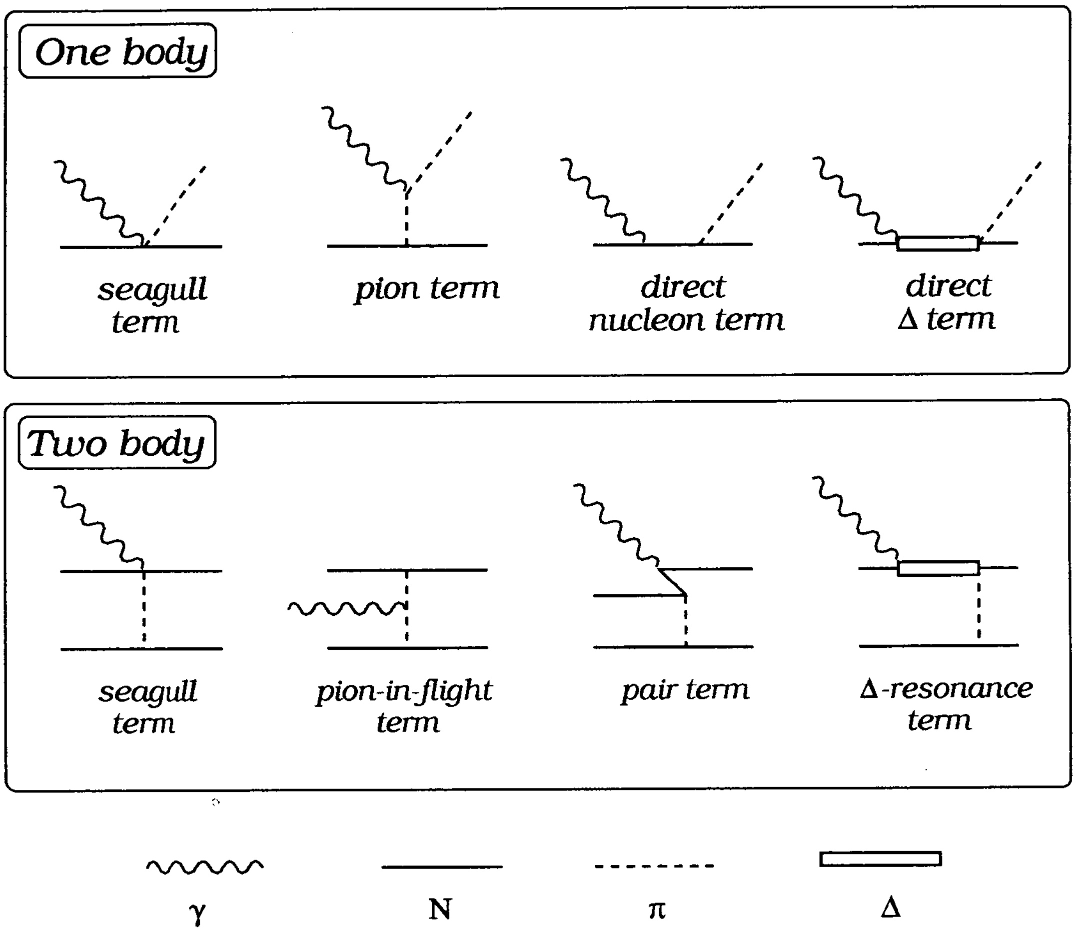

Figure 1.2: *One and two body photoabsorption terms*

1.3 Previous Work

Although there has been a considerable amount of work done in the field of pion photoproduction on nuclei, the vast majority of the work has been carried out at energies near the threshold energy for the production of pions (about 140 MeV). Such experiments have mainly been concerned with examining the exclusive (γ,π)

reaction, with no nucleon being emitted [Nag91]. This lack of an outgoing nucleon means that the definite final state of the residual nucleus can be established simply by measuring the energy and position of the pion. These experiments have primarily been carried out to investigate nuclear structure, as the (γ,π) reaction is highly sensitive to nuclear structure effects.

The higher energies that the current experiments have been carried out at mean we have entered the Delta resonance region. In this region it is possible for one or more nucleons to also be emitted from the nucleus. These reactions have less sensitivity to nuclear structure but can be used to investigate how the nuclear environment might affect the production of pions compared to free pion production. There has been much less work done in this area, and what data there are suffer from restrictions imposed on experimental kinematics, low resolution of results, or inability to detect some of the reaction products. A brief review of these experiments now follows.

1.3.1 The Bonn Experiments

The tagged photon beam of the Bonn 500 MeV Synchrotron has been used by Arends *et al.* to perform charged pion photoproduction experiments on numerous nuclei [Are82, Are91]. Typically for a ^{12}C experiment, the photon energy ranges from 200 to 390 MeV, with 10 MeV resolution.

The pions were detected using a magnetic spectrometer with particle momentum range 80-300 MeV/c and solid angle 80 msr. They were detected at angles of 48, 72, 108 and 128°, with a detector threshold of $T_\pi = 40$ MeV. The results were expressed as double differential cross-sections $\frac{d^2\sigma}{d\Omega_\pi dT_\pi}$ versus pion energy. These were compared to results from a Monte Carlo simulation code PIKI [Are82], which starts from Quasi-Free Pion Production and includes some form of Final State Interactions (FSI). As can be seen from figure 1.3, the results obtained agree fairly well with the PIKI code (solid line) for all the targets.

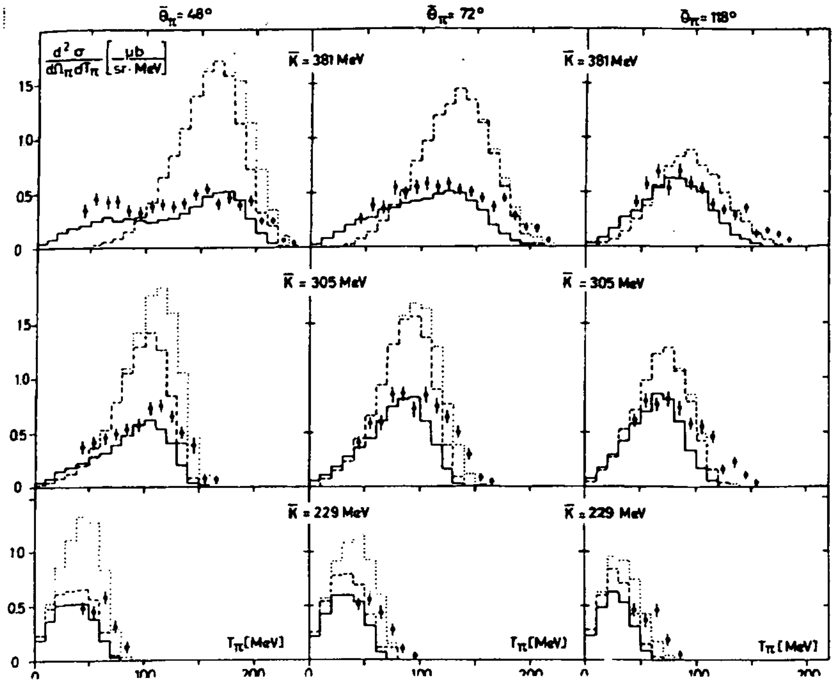

Figure 1.3: *Comparison between Bonn data and PIKI*

1.3.2 The MIT-Bates Experiments

In contrast to the Bonn data, the MIT-Bates experiments studied the exclusive coincidence reaction of (γ,π^-p) on an Oxygen-16 target [Pha92]. The experiment used a bremsstrahlung photon beam with end-point energy of approximately 360 MeV which was obtained at the Bates Linear Accelerator Center.

As in the Bonn experiments, the pions were detected using a magnetic spectrometer, this time with a solid angle of 5.1 msr and with the pion detection angle set at $\theta_\pi = 64°$ and 120°. The energy and out-of-plane angle of the coincident protons were measured using an array of scintillator telescopes, and a lower proton energy threshold of 30 MeV was imposed.

The data from this set-up was subsequently presented as double differential cross-sections $\frac{d^2\sigma}{d\Omega_\pi d\Omega_p}$ versus proton out-of-plane angle, with integration over the pion and proton energies. Despite this, the data still had poor statistics, and also suffered because of complex analysis due to the bremsstrahlung beam. The data was compared to the THREEDEE code [Cha77] which uses the Distorted

Wave Impulse Approximation (DWIA). As figure 1.4 shows, there is reasonable agreement at pion backward angles, but not at forward angles. Pham *et al.* suggested this was due to Δ medium effects, since the THREEDEE code does not include any Δ propagation effects.

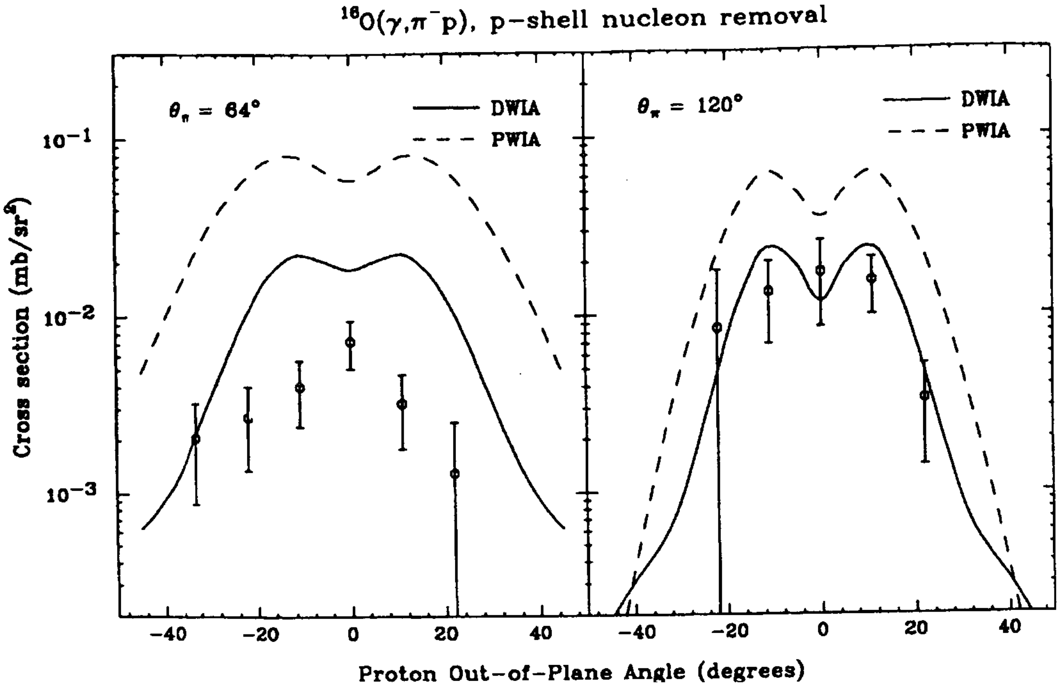

Figure 1.4: *Comparison between MIT-Bates data and THREEDEE*

1.3.3 The Tomsk Experiments

A number of papers published by Glavanokov *et al.* and Anan'in *et al.* provide probably the best data so far in this field. Typically [Gla79a, Gla79b, Gla89, Ana90], the Tomsk electron synchrotron gave a bremsstrahlung photon beam with end-point energies of 350, 370 and 390 MeV. Using this beam, an exclusive (γ,$\pi^- p$) measurement was carried out on Carbon-12.

The coincident pions and protons were detected using a double-arm spectrometer set-up. The pion energies were established from a measurement of their range in a Copper absorber. The pion energy acceptance was 40-180 MeV and the average detection angle was 120°. The proton energies were measured by time-of-flight. This gave a proton energy acceptance of 50-190 MeV and a measured angle of 20°. All measurements took place in coplanar geometry.

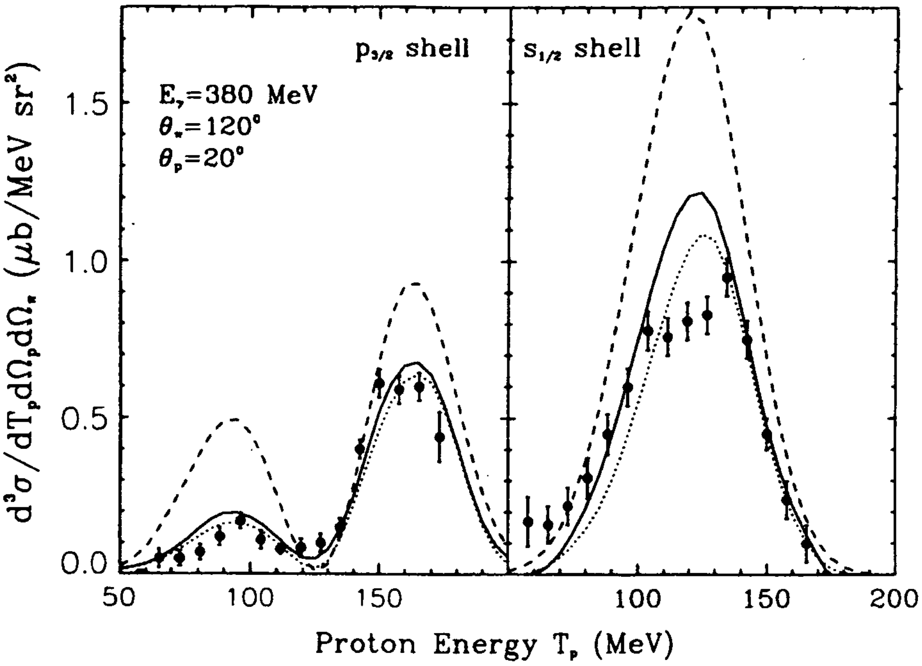

Figure 1.5: *Comparison between Tomsk data and DWIA*

The collected data was presented as triple differential cross-sections $\frac{d^3\sigma}{dT_p d\Omega_\pi d\Omega_p}$ versus proton energy. The resolution of this data was good enough to separate removal from the $p_{3/2}$ and $s_{1/2}$ shells. This data has recently been compared to the DWIA calculations of Li *et al.* [Li93]. The figure above shows a reasonable agreement with the DWIA code (solid line) which tries to account for the final state interactions with the nuclear medium unlike the simpler Plane Wave Impulse Approximation (dashed line) which gives a poorer fit to the data.

1.3.4 Present Work

The various problems apparent in the previous data can all be greatly reduced in the current program of experiments at Mainz. These experiments provide an extensive survey of both (γ,π^+n) and (γ,π^+p) exclusive reactions on several nuclei, including ^{6}Li, ^{12}C and ^{40}Ca over a large region of phase space. This has been done over the whole Delta resonance region thanks to a photon energy range of 150-800 MeV which is tagged to 2 MeV resolution, with an overall experimental resolution of the order of 15 MeV. There is also a much wider angular range for particle detection and lower detector thresholds as can be seen from the table below, along with a maximum pion detection energy of 180 MeV.

Particle Type	Angular Range	Detector Threshold
pion	$50° < \theta_\pi < 130°$	30 MeV
neutron	$10° < \theta_n < 150°$	15 MeV
proton	$10° < \theta_p < 150°$	20 MeV

Table 1.1: *Particle detection details*

All of these factors combine to create a considerable improvement on previous data, which in turn will provide our best yet test of the various theoretical models, as well as highly useful comparisons with already existing data.

1.4 Free Pion Production

To properly understand the motivation behind the current experiment, we must look at the recent theoretical advances in this field. In this section a brief outline is given of the theory of pion photoproduction on a single nucleon. This is expanded on in the next section when we examine the theoretical problems and suggested solutions which occur when considering the production of such pions in the nuclear medium.

When a photon is incident on a nucleon the interaction is electromagnetic. That is, the photon couples with the nucleon's charge and magnetic moment. Assuming the photon's energy is high enough, this causes the nucleon to radiate mesons. In the energy range of interest (100 MeV $< E_\gamma <$ 400 MeV) we are chiefly concerned with the production of pions.

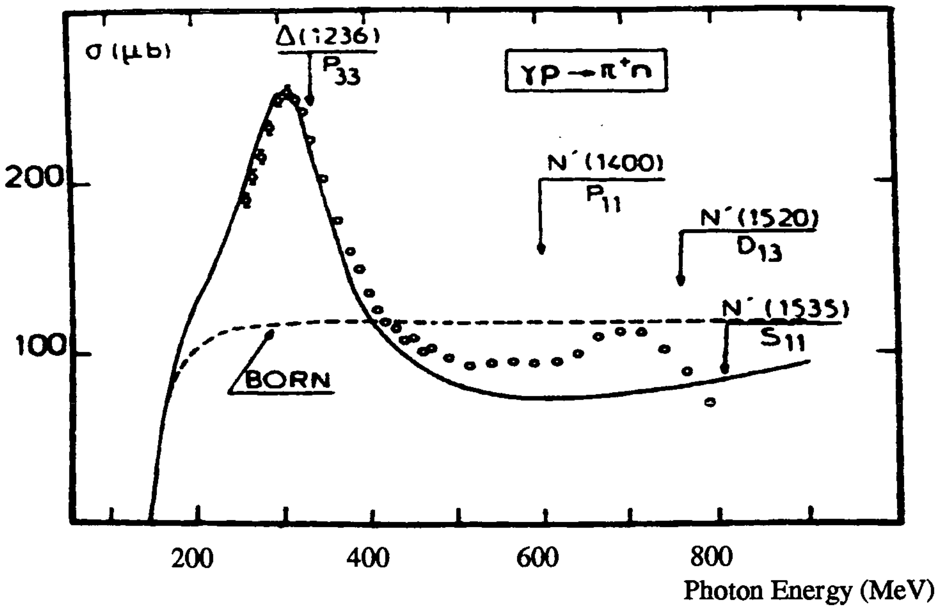

Figure 1.6: *Total cross-section for free pion production*

The total cross-section for the γp→ πn reaction is shown above in figure 1.6. Obviously there is a threshold at the pion mass (~ 140 MeV), and from there the cross-section rises to a resonance at E_γ ~ 340 MeV. This is the Δ(1232) resonance region. In the energy range shown there are in fact four nucleon resonances which interfere with each other and with the background Born terms (dotted line). However the Δ resonance dominates, as can be seen from the solid line which is calculated by taking only the Δ resonance and Born terms into account. The higher resonances are unresolved due to their overlapping widths.

There are two factors in the process of nucleonic pion photoproduction which cause problems in attaining an adequate description of the process. The first is that the nucleon is not point-like, but consists of a sub-structure of quarks. In such a description, the nucleon can be thought of as existing surrounded by a cloud of virtual mesons and this alters its charge distribution and magnetic moment thus rendering the coupling with the photon more complex. Also a problem is the strong interaction between the nucleon and the produced pion. This causes complicated rescattering processes to occur, leading to multiparticle intermediate states. The description of these effects relies on pion scattering data being used phenomenologically in various theories.

The mathematical starting point for the reaction is the Born approximation (the dotted line in the previous diagram) which assumes the particle wave functions are plane waves and does not take into account any terms concerning resonances or multiparticle intermediate states. The subsequently calculated Born terms dominate the reaction at low energies but are insufficient to account for charged pion photoproduction. They are, however, still important, as fifty percent of the cross-section in the Δ resonance is due to them.

We must, therefore, go beyond the Born approximation to adequately describe the reaction in this region. A model must be found which will include nucleon resonances and multiparticle intermediate states in the amplitude. There have been two main theoretical approaches towards this problem, each with their own advantages and disadvantages.

The first of these is the use of dispersion relations. These were first used by Kronig and Kramers in their work on optics. They have since been applied to the current topic, firstly by Chew *et al.* [Che57], and more recently by Berends *et al.* [Ber67]. The dispersion relation for the transition amplitude of the reaction is expressed as a sum of three parts:

- The Born term as described earlier
- A direct particle rescattering term
- A term describing contributions from other pion partial waves

This relation is solvable assuming from Watson's Theorem [Wat54] that the multipole amplitude phase equals that of pion scattering. There is however a problem in using this for nuclear calculations. The fermi motion of a nucleon means the amplitude must be transformed into an invariant form causing mathematical complexities and loss of physical information.

The other approach is to use an effective Lagrangian. Here the non-Born terms are explicitly included in the form of intermediate state particle terms and

Δ resonance terms. This can be done by gleaning relevant information (coupling constants, widths etc.) from pion scattering data. Final state rescattering can be treated by again attributing each multipole with the correct phase. All this has been done by Blomqvist and Laget [Blo77]. Once information from pion scattering was fitted to their calculations, all the Feynmann diagrams for the relevant terms could be calculated and added to the Born terms.

This effective Lagrangian approach has less physical basis than the dispersion relations technique, but does retain information concerning the processes involved. It also has the advantage of being easier to use in the extension to nuclear calculations.

1.5 Pion Production on Nuclei

In this section we shall look at how the nuclear medium changes the process of pion photoproduction with respect to the free nucleon case. These various nuclear effects will be discussed and theoretical models to adequately describe these effects will be examined.

1.5.1 Nuclear Medium Effects

In the nucleus, nucleons are not stationary but move around with a certain amount of momentum. This movement is fermi motion and it causes a general "blurring" of the pion photoproduction process since the nucleon is characterised by its momentum distribution. This leads to a broadening of the resonance in the cross-section.

Pauli's exclusion principle states that no two identical fermions can occupy the same state at the same time in a nucleus. When a photon interacts with a nucleon it transfers some of its energy and momentum to that nucleon. This cannot now happen, however, if it would lead to the nucleon being in a state already occupied by another nucleon. The photon must therefore deliver enough energy to enable the nucleon to reach an unoccupied state. This obviously results in a reduction in the probability of the interaction and consequently in the cross-section of the reaction.

A highly important consequence of the nuclear medium is that its presence greatly changes the nature of the Δ propagation. In the free case, the photon excites a nucleon to create a Δ which decays to a pion and a nucleon. However, in the nucleus, other channels are now open. The photon could meet a pre-formed Δ in the nucleus, or a virtual pion in flight between nucleons, or even interact with the residual nucleus, with the outgoing nucleon being a spectator. Furthermore, once the Δ exists it now has new decay modes e.g. $\Delta N \rightarrow NN$ with no pion produced. These features tend to broaden the resonance and reduce the number of pions produced. In contrast to this, Pauli blocking reduces the possibilities for decay products of the Δ, thus narrowing its width.

Another very important factor is the occurence of Final State Interactions (FSI). This term relates to the interactions between the produced particles in the initial reaction (nucleons and pions) and the residual nucleus. It assumes that the initial and subsequent interactions can be treated as separate occurrences, which is not always as clear-cut an assumption as it may seem. Essentially, these initial reaction products can undergo elastic or inelastic scattering or be reabsorbed back into the nucleus. The mathematical treatment of this will be discussed next, along with descriptions of how different theoretical models cope with all these different nuclear medium effects.

1.5.2 Theoretical Models

The Distorted Wave Impulse Approximation (DWIA) Model

This model has its starting point at the Impulse Approximation (IA). This neglects medium effects initially by using the free production transition operator, but does account for fermi motion. The most recent exponents of this method have been Li *et al.* [Li93]. They used the Blomqvist-Laget transition operator [Blo77]. This takes care of the initial interaction. The next step is to account for FSI. This is done by distorting the outgoing waves of the produced particles by the application of optical potentials. This method leads to the DWIA model.

An optical potential, when applied to the plane wave of an outgoing particle, distorts that wave producing a scattered particle. The potential has a real and an imaginary part. The real part corresponds physically to elastic scattering of the particle with some particle or particles in the residual nucleus. The imaginary part corresponds to the possibility of the particle being either inelastically scattered or absorbed somewhere in the residual nucleus. The optical potential has an energy dependence. That is, the chances of a certain thing happening to the produced particle in the nucleus depend on the energy it possesses. Parameters for this potential are extracted from pion and nuclear scattering data.

Li *et al.* have carried out a fully non-localised DWIA calculation and compared results both to Tomsk data [Gla79a] and to MIT data [Pha92]. They ensured non-locality of the transition operator by integrating over the whole range of momenta a distorted outgoing particle wave could have. They found that non-local effects are significant in (γ,πN) calculations. In their comparison with experiment, Li *et al.* found a rough agreement with Tomsk data, but overestimated with respect to the Bates results.

One major drawback with this method is that it does not take modifications to the Δ propagation into account. We shall now look at a model which attempts this, albeit in a phenomenological way.

The Δ-Hole Model

This model concentrates on the produced Δ and takes it to be the dominant initial process. The Δ and its associated hole then propagate through the nucleus and the medium effects are accounted for within the form of this propagator. This approach was first used in pion scattering [Koc84] and has most recently been studied in the present context by Sato and Takaki [Sat93].

In their approach the free resonance in the transition operator is replaced by a Green function representing a sum of several factors, namely:

- The free resonance term
- A rescattering term including coherent π^0 production followed by pion charge exchange
- A term to account for Pauli blocking of the Δ decay
- New decay modes term, determined from pion-nucleus scattering

A comparison with MIT data again showed a sizeable overestimate by the model at forward angles. Sato *et al.* suggested this could be due to an additional reaction mechanism with a strong angular dependence. A comparison with DWIA did however show that the medium effects on Δ propagation are extremely important.

Full Microscopic Model

This model starts from the basic couplings between photons, pions, nucleons and resonances. From this point, Carrasco and Oset [Car94] used field theoretical methods to establish the photon self-energy. The pion and Δ interactions within the nucleus are treated as pion-hole and Δ-hole effective interactions which already contain the Pauli exclusion effect. An attempt is made to simulate Final State Interactions such as inelastic rescattering within the nucleus or absorption of particles before they escape the nucleus. A Monte Carlo type simulation is then run including all these factors to generate events and simulate a real reaction experiment.

An obvious disadvantage with this nuclear matter approach is that there is no nuclear structure input. This has so far proved acceptable when comparing to inclusive measurements but may cause problems with fully exclusive comparisons, where the data is sensitive to the structure of the nucleus.

The main advantage of this model is its ability to differentiate between and separate the various reaction channels. Oset *et al.* distinguish between so-called direct and indirect photon absorption. The first is a one-step absorption onto one or two nucleons, the second is a two-step process with an emitted pion from the first step being reabsorbed later. Because of this ability to distinguish reaction types, some interesting results have emerged. In their paper [Car92b], a comparison of these interactions on different nuclei was carried out. The results suggest indirect absorption has a much stronger dependence on the nuclear mass compared to the A dependence of pion absorption experiments on nuclei. They therefore suggest that further investigation of these reactions would be of great value in determining more about the pion absorption mechanism. A Monte Carlo cascade treatment by Oset and Carrasco has been used in this thesis to compare to the data. Although this approach treats FSI semi-classically, it has proved useful in comparisons within the intermediate energy range.

1.6 Complementary Reactions

It is worthwhile, finally in this chapter, to take a look at some of the complementary processes in the photonuclear field. Many of these share considerable common ground with pion photoproduction and comparisons between different reactions can only help our understanding of what goes on inside the nucleus.

In the past there has been a lot of work in the study of pion absorption on nuclei [Smi89, Hym90, Ran90, Ste90]. This is analogous to photon absorption in that both are bosons and both are considerably lighter than nucleons. However whereas the photon interaction is electromagnetic, the pions interact with nucleons via the strong interaction. This means the interaction probability is so large that most interactions occur at the nuclear surface leading to an $A^{2/3}$ dependence of the cross-section. Effectively, the nuclear interior is "screened off" from the pions which cannot probe them. Since the photon does not experience this screening it makes for a more useful probe of the nucleus, with pions being produced throughout the nuclear volume. This leads to a greater sensitivity to the pion production and absorption mechanisms.

Another reaction which is of great interest for comparison is the inclusive

(γ,π). A comprehensive study by Arends *et al.* [Are91] for different target nuclei has discovered a mass dependence of $A^{0.6}$ for this reaction. It is suggested that this is due to a volume effect followed by strong final state interactions. A comparison between exclusive (γ,πN) and inclusive (γ,π) would be of benefit in trying to establish the importance of FSI in both pion production reactions.

As mentioned earlier in section 1.2 the (γ,NN) reaction is an interesting one for comparison to (γ,πN). Indeed that is why the current experimental collaboration has been undertaking both experiments concurrently. Since the emission of back to back nucleons is a result of two body absorption of the photon (QD model), a comparison between this and πN production (one body absorption via the QFPP model) would be extremely useful in determining the relative strengths of these two mechanisms.

Finally, in electron scattering experiments, we have a process involving a virtual photon, which can be usefully compared to current photonuclear experiments. The virtual photon has both a longitudinal and a transverse component. The longitudinal part is sensitive to nuclear degrees of freedom, whereas the tranverse part is sensitive to pionic parts of the nuclear wavefunction. Experiments are usually carried out in parallel kinematics, thus eliminating interference between the two components. Such experiments [Die90] have shown evidence of both one and two body absorption within the Δ resonance region, as well as many body absorption and an influence from meson exchange currents. A comparison with possible future triple coincidence experiments (e,e$'$NN) and (e,e$'\pi$N) would give more information regarding these different mechanisms than previously attained.

Chapter 2

Experimental System

2.1 Overview

The data presented in this thesis was accumulated during an experiment performed at the Institut für Kernphysik in Mainz, Germany. The microtron electron accelerator at Mainz (called MAMI-B) is used in conjunction with the Glasgow University Photon Tagging Spectrometer to create a high quality source of photons, which is the lynchpin of the A2 (real photons) experimental program.

The results presented here are part of an ongoing collaboration using the A2 experimental hall, and involving the Universities of Edinburgh, Glasgow and Tübingen. This collaboration is currently investigating the many facets of the absorption of photons on nuclei through both (γ, pN) and $(\gamma, \pi\mathrm{N})$ reactions.

The emitted particles from these photonuclear reactions are detected by two main detector arrays, placed on either side of the target. On one side is PiP, a scintillator telescope which detects pions and protons. On the other side is TOF, a time-of-flight array of scintillator detectors used to detect charged and neutral particles. There are also ΔE detectors in place for purposes of particle identification and event triggering. The signals from these detector systems are collected and processed by the associated electronics system, and transferred via controlling software to a computer system for both on-line analysis and storage. The rest of this chapter will describe this experimental set-up in more detail.

2.2 The Mainz Microtron Facility

The Mainz microtron facility, MAMI-B, has been in operation since 1990, and provides an extremely good quality, 100% duty factor electron beam. It consists of three racetrack microtrons (RTMs) which, when combined, give a stable 855 MeV beam. The current of this beam can be as large as one hundred microamps, but was considerably less for the present experiments due to restrictions in the photon tagging technique.

2.2.1 Racetrack Microtron Review

The racetrack microtron (see figure 2.1) is a relatively recent development in electron accelerators, and is an elegant way of overcoming problems associated with linear accelerators (linacs). Linacs typically have a very low duty factor, and this has been vastly improved for RTMs. In fact at Mainz, the MAMI-B microtron has a 100% duty factor, effectively producing a DC beam. This is essential for coincidence experiments to reduce problems with high random backgrounds and dead times, meaning experiments can be done both quicker and more accurately.

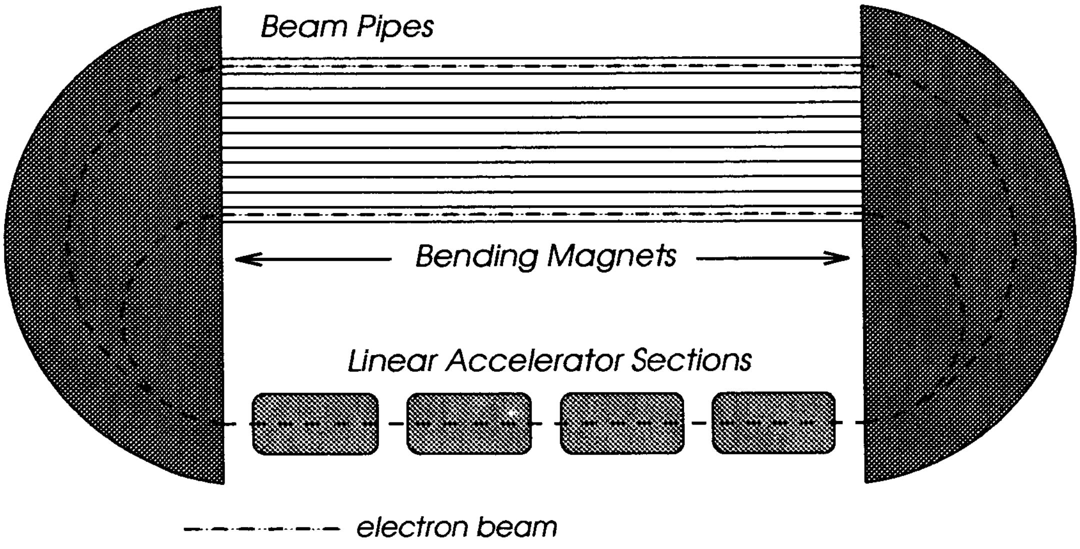

Figure 2.1: *A schematic diagram of a racetrack microtron.*

In a RTM, an electron beam is injected into a linac. The electrons are accelerated down waveguides by a radio frequency (RF) electric field supplied by klystrons. They are then recirculated by bending magnets. As the electrons do "laps of the racetrack" they gain in energy accordingly. With increased energy comes increased orbit length, meaning the electrons' paths diverge and they can then travel through separate beam pipes. This means that they can be steered and focused separately, a procedure which is completely computer controlled. Obviously, an electron can do many laps of the racetrack, therefore reducing the energy gain required at each pass. It is this feature that facilitates the 100% duty factor, since the klystrons can be operated in continuous mode. Although the beam does retain the "pulse-like" nature of the RF electric field, this Gigahertz modulation is typically far too fast to be observed by particle detectors. Thus we effectively have a DC electron beam.

2.2.2 The MAMI-B Microtron

The MAMI-B facility is shown in figure 2.2. In the production of the electron beam at Mainz, three RTMs are used together. Initially a 100 keV electron gun, followed by three linac sections provides 3.5 MeV electrons which are injected into the first RTM. This has 18 turns and increases the electron energy to 14 MeV. They are then extracted and injected into the second, 51 turn RTM which provides a 180 MeV beam. This in turn is guided into the third and final RTM which produces a 855 MeV beam from its 90 orbits. This beam can have currents up to 100 μA, and has a resolution of 60 keV.

The electrons are then steered and focussed using various dipole and quadropole magnets into one of the halls as shown for experimental use.

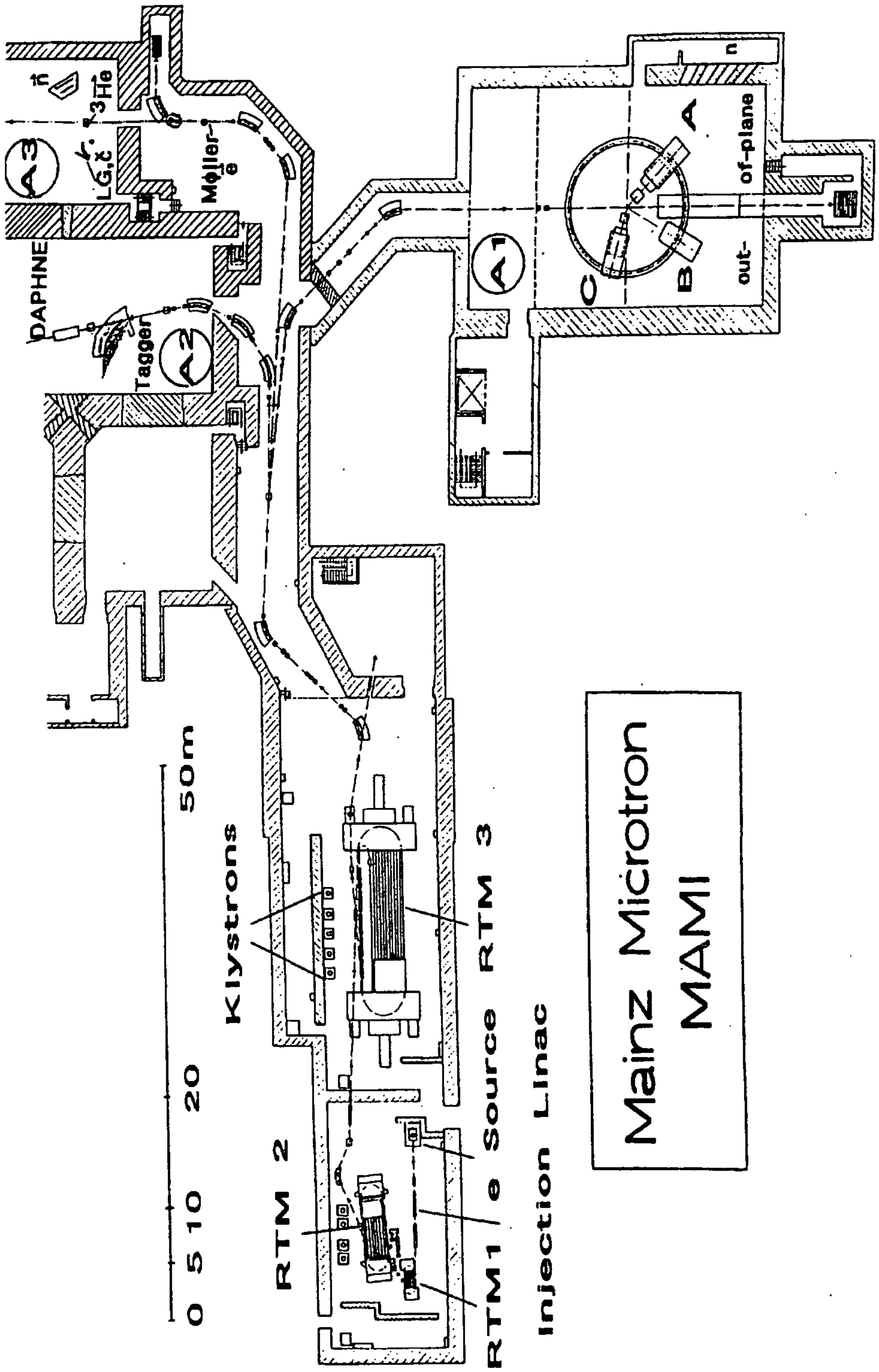

Figure 2.2: *The microtron (MAMI-B) at the Institut für Kernphysik in Mainz.*

2.3 Photon Tagging System

2.3.1 Production of a Photon Beam

The high quality, stable electron beam produced by the MAMI-B facility has been described in the previous section. This beam is then guided into the A2 hall, where the photon tagging system transforms this electron beam into a usable photon beam.

The electron beam is directed onto a thin foil radiator which produces a photon via the bremsstrahlung process. The type of radiator which is used must be chosen with care. A suitable balance must be achieved between the desire for a high rate of photons being produced (photon flux) and the desire for a high efficiency for the tagging of these photons. The photon flux depends on the thickness of the radiator in radiation lengths, meaning radiators made of a high Z material would have to be very thin, which is technically hard to achieve and difficult to handle. Unfortunately, radiators with a low number of nucleons have the drawback of larger multiple scattering contributions, reducing the tagging efficiency. In balancing these two factors, a middle ground was sought and as a result a 4 μm, 3×10^{-4} radiation lengths Nickel foil radiator has been used for these experiments.

2.3.2 The Tagging Spectrometer

The tagging spectrometer and focal plane detector are shown overleaf in figure 2.3. Since many different experiments have been planned in the A2 collaboration, the design of the spectrometer and focal plane detector (FPD) had to be flexible and wide ranging enough to accomodate all of them [Ant91]. As a result, the spectrometer is able to cover a large energy range at one magnet setting. The electron energies which can be measured are between 40 MeV and 790 MeV, which is ideal for our purposes as this nicely covers both single and double pion production thresholds.

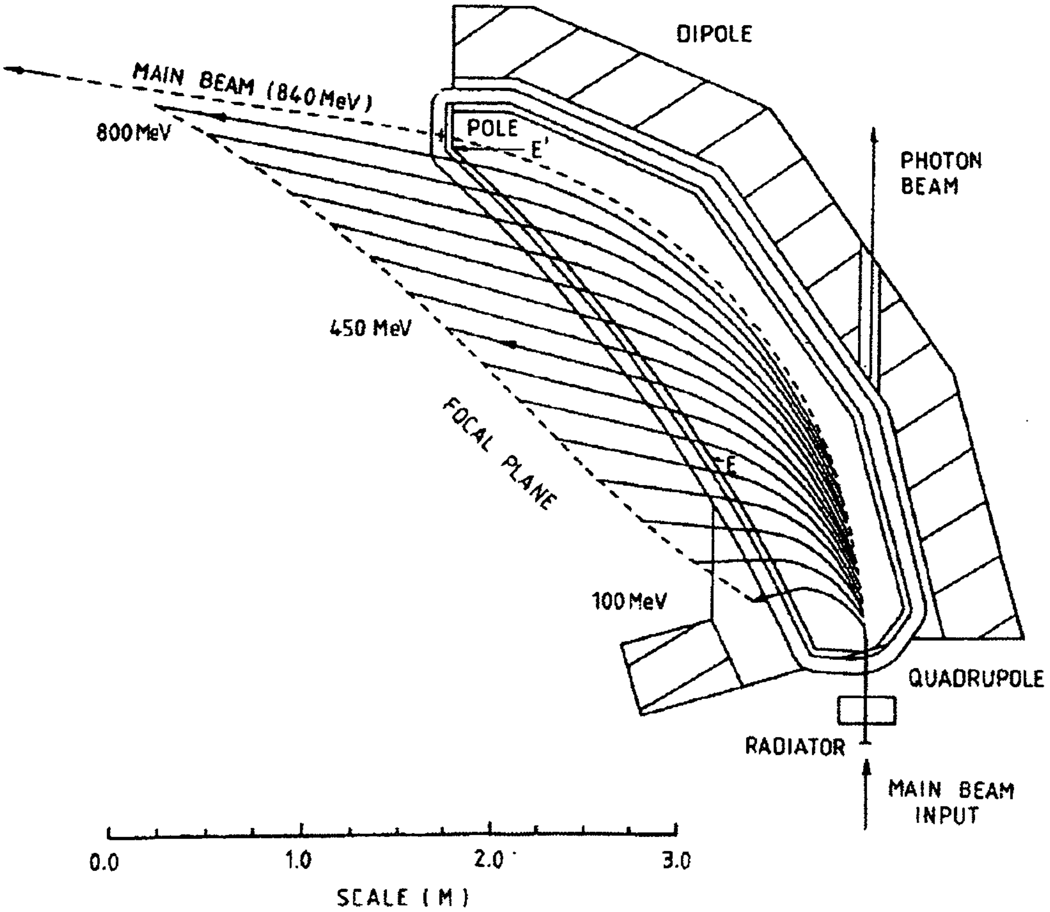

Figure 2.3: *The photon tagging system*

With respect to the physical design of the spectrometer, it must have a large enough entrance solid angle to accept most of the residual electrons from the radiator foil. It must also have a good vertical focussing capability to reduce the pole gap required. To these ends a quadropole-dipole magnet design was chosen. The quadropole magnet gives improved vertical focussing, while the dipole magnet bends the residual electrons round into the focal plane. It also has the advantage of directing the electrons that did not undergo bremsstrahlung radiation interactions into the beam dump.

2.3.3 The Focal Plane Detector

It is essential to this technique to determine the energy of the residual electron accurately, since the photon energy is simply calculated from:

$$E_\gamma = E_e - E_{e'} \tag{2.1}$$

where E_e is known to be 855 MeV in this case. This is done by establishing at what point the electron crosses the focal plane of the spectrometer. To achieve this a large FPD consisting of 352 scintillator elements is positioned in the focal plane. This enables photon energies between 40-790 MeV to be determined with a resolution of about 2.2 MeV [Hal90].

Each scintillator element is connected via a light guide to a photomultiplier tube (PMT). The signal from this enters a constant fraction discriminator which produces an associated logic pulse. This information is then stored in on-line computers via the FASTBUS scalers and the time-to-digital-converters (TDCs). The scaler information is used to determine photon flux, and the TDC signals are used to establish a coincidence between a residual electron hit in the FPD and a reaction in the target caused by a photon. In this way, the electron "responsible" for the photon which is interacting with the target can be identified, and the photon's energy established.

2.3.4 Photon Collimation and Tagging Efficiency

Since the distance between the radiator and the target is several metres, the photon beam must be collimated to ensure a small beam spot is incident on the target. A small beam spot is advantageous because it reduces error in establishing the exact point of the reaction in the target, and subsequently reduces the error in the outgoing particles' trajectories.

There were in fact three separate Lead collimators used on the photon beam. The first (5cm long and 5mm diameter) was placed two and a half metres from the radiator to ensure a small beam diameter. The second, of similar proportions, was placed just downstream of the first to remove electrons and positrons created at the first collimator. Finally, the third one, diameter 30mm, was placed near the target to prevent any remaining charged particles triggering the ΔE detectors near the beam. This arrangement gave a beam spot of diameter 20mm on the target. One added advantage of collimation is to allow the various particle detectors to be placed closer to the beamline, and therefore closer to the target.

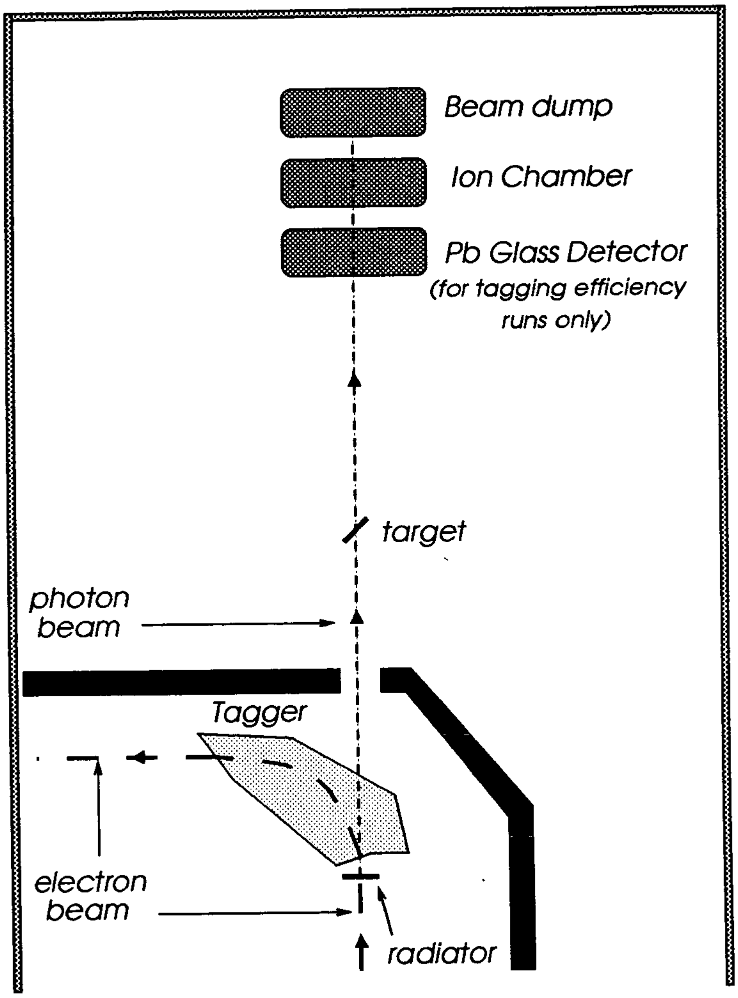

Figure 2.4: *A schematic diagram of the beamline*

During a typical experiment, the photons which did not interact with the target were dumped at the far end of the experimental hall. A schematic diagram of the beamline is shown in figure 2.4. In front of this beam dump was an ionisation chamber which was used as a monitor of the photon flux. This was only a rough guide, and the tagging efficiency was calculated later using the scaler values from the FPD.

The tagging efficiency, ϵ_{tagg}, for the system is given as the ratio of electron hits on the FPD which have a coincident photon, to the total number of electron hits at the focal plane. To measure this value, a Pb glass detector is placed in the photon beam well downstream of the target. Its position and size ensure that it detects virtually all the photons in the beam, as long as the beam current is lowered to give a reasonably low count rate. This also helps reduce possible random coincidences in the FPD.

A photon incident on this detector creates a trigger, which then looks for a coincidence hit in one of the tagger elements. The tagging efficiency is then given by:

$$\epsilon_{tagg} = \frac{\text{number of coincidence hits}}{\text{total number of tagger hits}} \tag{2.2}$$

This efficiency was measured periodically throughout the experiments, and analysis has revealed a fairly stable value of around 55% at all photon energies.

2.4 Targets

There were several targets used in this experiment. Lithium-6, Carbon-12 and Calcium-40 were all used, with the Carbon target receiving the majority of beam-time. A CH_2 target was also used for calibration data. CH_2 is a good source of Hydrogen (i.e. protons) and since the kinematics of the $p(\gamma,\pi n)$ are well defined and the Carbon background can be removed efficiently, this can be used to calibrate the detector systems.

The various targets were mounted on a ladder which was run by a stepper motor. This could be controlled by computer from outside the hall to rotate the target and move it vertically. The target is set at an angle to the beam so that it intercepts all of the photons, thus increasing the likelihood of a reaction. This angle must be chosen carefully. Angles close to 0° will have a large beam spot on the target, which will lose angular resolution. Angles close to 90°, however, experience a different problem. Since most pions are detected normal to the beam direction, a large angle will mean larger pion energy loss in the target, reducing energy resolution.

This angle choice must be taken in conjunction with the target thickness. Obviously a thicker target presents more nuclei per square centimetre to the beam, therefore increasing the number of reactions. Unfortunately, it also increases uncertainty in the reaction vertex, again reducing angular resolution. In the end, the following thicknesses and angles were used for the experimental targets:-

Target	thickness	angle
Lithium-6	10.5 mm	30°
Carbon-12	5.0 mm	20°
Calcium-40	2.2 mm	30°
CH_2	10.0 mm	20°

Table 2.1: *Summary of targets*

2.5 The Particle Detector System

2.5.1 General Requirements

There are many different reactions which can occur between a photon and a nucleus, and this leads to many different reaction products being emitted. Atomic processes such as (γ,e) also give a large electron background. Any system used to detect particles from such an experiment as this must, therefore, satisfy certain criteria.

The most important of these criteria is the ability to identify the particle in question. Since electrons, protons, pions and neutrons are all emitted, a detector must be able to distinguish between them. Determination of the particle's energy to a reasonable precision is also essential. In the present set-up, energy is established either by measuring the energy deposited in a detector or by time-of-flight methods. The third criteria is that of angular resolution. For comparison with theory, the angle of the emitted particle must be known accurately.

The arrangement of detectors for these experiments is shown in figure 2.5. There are three detectors , namely the ΔE-ring, PiP and TOF. All three arrays consist of combinations of scintillator blocks, although they are used in various ways to detect different particles.

The basic idea behind scintillator particle detection is fairly straightforward. If a charged particle enters a scintillator block, the particle ionises causing the scintillator to emit light. This light travels down to the ends of the block and is focussed at each end by a light guide onto a PMT. This converts the light into an electrical signal and amplifies it. We now have an electrical pulse which represents the amount of light emitted by the particle. This, in turn, reflects the amount of ionisation which took place, and indirectly, gives the energy of the particle. Also, the time difference between when the light reaches either end of the block can be used to give an indication of the particle's position. These basic features have been used and expanded upon in different ways to detect a variety of particles in the three detectors which are now described in the next three sections.

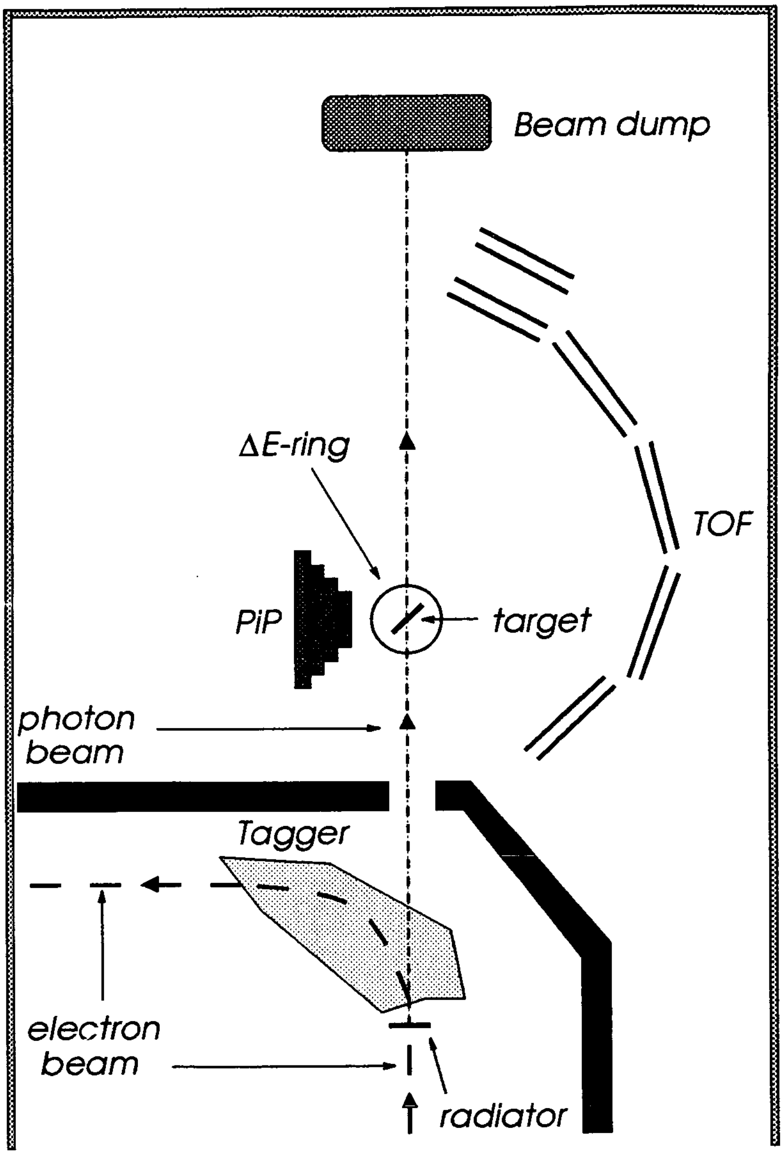

Figure 2.5: *The detector arrangement in the A2 hall*

2.5.2 The ΔE Detector

The ΔE detector is really two separate detectors with two distinct and different purposes. A schematic diagram of the array is shown in figure 2.6. The detector ring is centred on the target position with each side of the ring consisting of seven scintillator blocks.

On the PiP side, a charged particle passing through the scintillator will give a signal, this is used as a "start time" for an experimental event. This is a good approximation to the actual time an event started due to the proximity of the detector to the target. The detector blocks are made thin enough to allow a pion through without seriously affecting its energy.

The signal from this array can also be used in conjunction with a PiP signal to eliminate random and background signals which do not show the expected energy loss or path of a pion. This combination can also be used to identify particles by plotting dE versus E for PiP (this is discussed further in chapter 3).

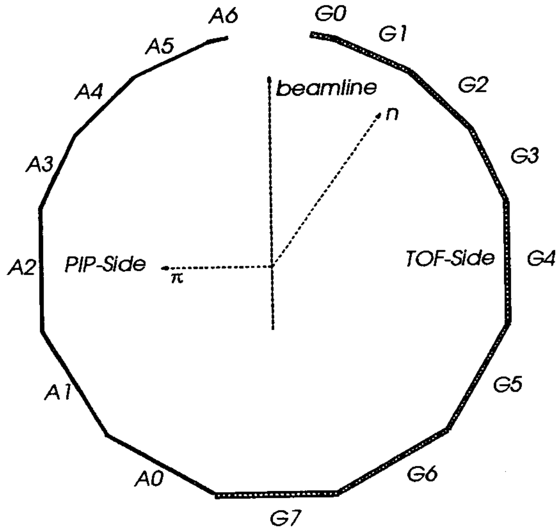

Figure 2.6: *The ΔE detector*

The detector on the TOF side is used for the detection of neutrons. Since these particles are neutral, they are detected following scattering off protons in the detector, which then give a signal. To distinguish these from actual protons emitted from the target, the ΔE array is employed. Since a neutron detected in TOF will not have given a signal in the ΔE but a proton will have, the ΔE detector is used to veto protons or other charged particles. The signal from the TOF side of ΔE can also be used in the dE-E method of particle identification.

2.5.3 The PiP Detector

The PiP detector is a segmented scintillator telescope. It can be used to detect protons and pions. In these experiments, it has been used exclusively to detect positive pions (see the next chapter for details). It consists of five separate layers of scintillator. The first of these is a thin ΔE layer consisting of four vertical scintillator strips of dimensions 2mm thick x 20cm wide x 42cm high. As can be seen from figure 2.7, the main body of PiP consists of four horizontal layers, the dimensions of which are given below.

- **E1 Layer:** 4 blocks each of 100cm x 11cm x 13.5cm
- **E2 Layer:** 4 blocks each of 130cm x 17.5cm x 17.5cm
- **E3 Layer:** 5 blocks each of 160cm x 17.5cm x 17.5cm
- **E4 Layer:** 6 blocks each of 190cm x 17.5cm x 17.5cm

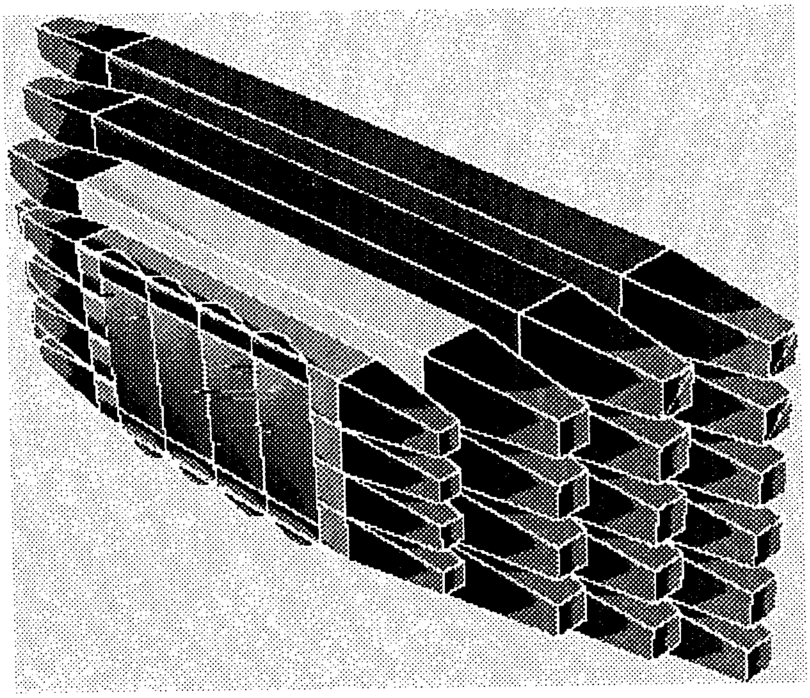

Figure 2.7: *The PiP detector*

Each successive layer is larger than the one in front, in order not to lose any of the solid angle acceptance of particles from the target, which is roughly 1 steradian [Bra91]. The light produced in the blocks is guided into photomultiplier tubes at either end of each block using light guides. The E blocks use 130mm EMI 9823KB photomultiplier tubes and the ΔE blocks use 50mm EMI 9954KB tubes.

Each block is wrapped in Aluminium foil, black card and black tape in order to reduce the possibility of signals emanating from external light sources. The whole system is also shielded by 5mm steel plating to further reduce light leaks. The detector is mounted on a strong steel framework with the associated electronics mounted on racks at the rear of the detector.

2.5.4 The TOF Detector

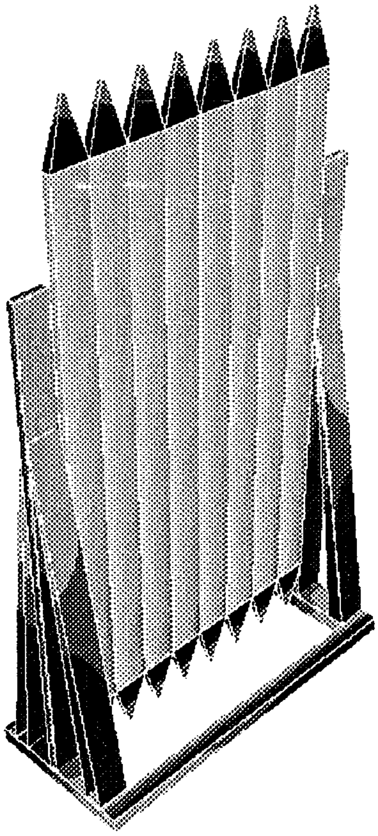

Figure 2.8: *A TOF stand*

The TOF array consists of ninety-six scintillator bars in all, these bars being mounted vertically on movable frames, eight at a time, with the frame able to hold up to twenty-four bars. A typical TOF stand is shown in figure 2.8. The dimensions of a single bar are 300cm x 20cm x 5cm. Using light guides, the light is directed into 3" Phillips XP 2312B photomultiplier tubes at either end of each block.

The mobility of the frames is essential to optimise solid angle and neutron detection efficiency, since different experiments have different kinematics and therefore require very different arrangements of the neutron detectors [Bra91].

As mentioned earlier, TOF detects neutrons via a proton knockout in the detector. Plastic scintillator is well suited to this process as it contains a large amount of Hydrogen (i.e. protons) and therefore the efficiency for neutron detection is relatively high.

2.6 Technicalities of Data Collection

As described earlier, a particle which enters a detector block will cause ionisation, resulting in signals in the relevant PMTs. The information held in these pulses must be transformed into a useful form for off-line analysis at a later date.

Technically, this is done in three stages. Firstly, the associated electronics must identify events of interest from the sea of background and random signals. The analogue information at this point must then be converted into a digital format. This information is then stored by the data acquisition system.

The identification of interesting events is done by the trigger electronics. When this recognises such an event, it starts Analogue-to-Digital Converters (ADCs), which digitise the pulse information in two ways. The height of a pulse from any PMT must be converted. This is done in Charge-to-Digital Converters (QDCs) which are gated by a trigger. Phillips FASTBUS 10c2 10-bit QDCs were used for this purpose. Similarily, the time difference between when the pulse occurs and the start-time for the event must be recorded. To do this, leading edge discriminators are used. These give a logic pulse output when the PMT pulse reaches a certain threshold. This logic pulse is used to stop a Time-to-Digital Convertor (TDC) which has previously been started by a signal from the start detector. For this purpose Phillips FASTBUS 10c6 10-bit TDCs were used. Figure 2.9 shows the typical link between a scintillator block in any of the three detectors and its associated ADCs.

While this digital information is being read out of these modules by the data acquisition system, the experiment must be disabled (this period of disablement is called *"dead-time"*). For this reason it is obviously beneficial to keep the number of randoms to a minimum i.e. make the triggers as efficient as possible. Once this digital data is stored, it can be used at a later date in off-line analysis to establish the kinematics of the reaction event which has taken place.

The rest of this section is split into two parts. The first deals in more detail with the complex trigger system, and the second describes the features of the data acquisition system.

2.6.1 Triggers

For this experiment there are three events of interest. The most important of these is a positive pion entering PiP with an associated particle entering TOF. The other two are cosmic rays in PiP (used for calibration); and flasher events in PiP and TOF, used for monitoring possible gain shifts in the PMT (more of these uses later).

The vital feature of trigger logic in any experiment is the timing. It takes a certain amount of time to decide whether to accept or reject an event. Meanwhile, the signals from the PMTs have to be delayed in order to coincide with the QDC gates and give a correlated time in the TDCs.

This has led to a two-tiered trigger system. There is a first level trigger which makes a speedy, simple decision. This can gate the ADC to start converting the event for storage. This trigger also has the option of initialising the second level trigger instead of the readout process, if more investigation of the event is required. The second level trigger can then either accept the event and commence data acquisition (which takes some time) or reject the event, resetting the ADCs, ready for the next event.

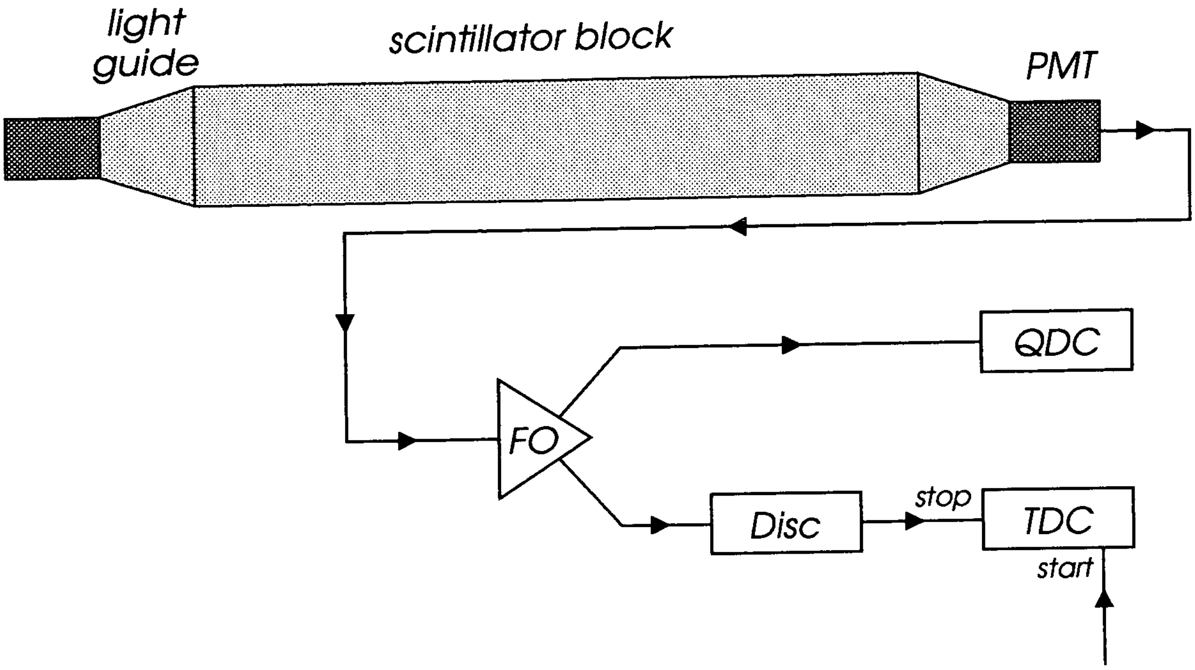

Figure 2.9: *A scintillator block and instrumentation*

The trigger logic is housed mainly in the Camac and NIM modules in the racks at the back of PiP. This is also fed signals from TOF and tagger electronics, essential for trigger requirements. The data acquisition computer is also housed in the PiP racks and receives inputs from all these modules.

First Level

There is one main experimental first level trigger and three lesser ones in this experiment. Signals from these are input into a Programmable Logic Unit or PLU (in this case, a Lecroy 4508) which decodes them and acts according to the various inputs. A description of how the triggers are created and how the PLU responds is given for each trigger next:

- **The PiP particle trigger:** This trigger is activated when a charged particle enters PiP from a reaction in the target. It is generated by demanding coincidence signals from the PiP-side ΔE, the PiP ΔE layer and the E1 layer of PiP. The timing of this trigger is correlated to the reaction time, and hence is used as the event start-time. QDC gates and TDC starts are generated from this but their contents are not read out. Instead, the second level trigger is called into action to determine which type of event has occured.

- **The flasher trigger:** PiP and TOF both have flasher units fitted. These consist of a Light Emitting Diode (LED) which sends a known amount of light into each PMT; and a PIN diode which monitors the LED's activity. By comparing the PIN diode signal to the PMT signal one can monitor the gain of the PMT and thus check its stability. Each time the flasher flashes, a trigger is created. If the PLU receives this trigger, it gates the ADCs and allows the contents to be read out and stored.

- **The cosmic trigger:** Cosmic rays which traverse a whole layer of PiP are used for calibration purposes. Therefore, a coincidence between the top and bottom blocks of any one layer is used to create this trigger. Again, if the PLU receives this, it enables readout immediately.

- **The Pb glass trigger:** This is created during tagging efficiency runs when a photon is detected in the Pb glass detector. As above, this trigger leads to immediate ADC readout and storage.

Once any of these triggers has been received, the PLU disables or "latches" its inputs. In other words, the inspection of events is put on hold until the current event has been processed fully. In the unlikely event of two triggers occurring simultaneously, the event is rejected and the system reset, ready to go again.

Second Level

When a charged particle is identified in PiP, the second level trigger is brought into play. This again helps in reducing random background events being stored needlessly. The first of the four second level triggers is the electron reject. There is a large amount of background electron events in PiP. These electrons generally stop very quickly in the detector. As a result, a hardware cut on a dE v E plot will eliminate most of them. This is done by demanding that a weighted sum of the PiP ΔE and E1 signals is above a certain discriminator threshold. If a signal is received in the E2 layer, this cut is overridden as the E1 signal is no longer representative of the particle's total energy.

Since we are looking for $(\gamma, \pi\mathrm{n})$ events, coincidence signals must also be received from TOF and the tagger. The tagger trigger comes from a gated OR of all the FPD elements. This must occur within 80 nsecs of the PiP signal. In practice this is virtually redundant because the chances of having no tagger hits in 80 nsecs at normal beam currents is negligible. The TOF OR is similar to the tagger one, it being a gated OR of all the TOF blocks, requiring a signal within 400 nsecs of the PiP trigger. This is a very useful trigger in eliminating dead-time, because the vast majority of PiP events have no correlated hit in TOF.

The final trigger is the PiP pion afterpulse trigger. Positive pions are identified by detecting the e^+ from the decay:

$$\pi^+ \rightarrow \mu^+ \rightarrow e^+ \tag{2.3}$$

After an initial pulse in PiP, the PiP blocks are inspected for 6 μsecs for an afterpulse. This should be plenty of time since the mean life of this decay is 2.2 μsecs. If an afterpulse is detected the trigger is created. The height of the afterpulse is stored and the time it occured is recorded in a special multi-hit, long range TDC. A diagram of this is shown in figure 2.10

These second level triggers are all fed into another PLU which monitors and decodes the signals. If an acceptable combination is received, data acquisition

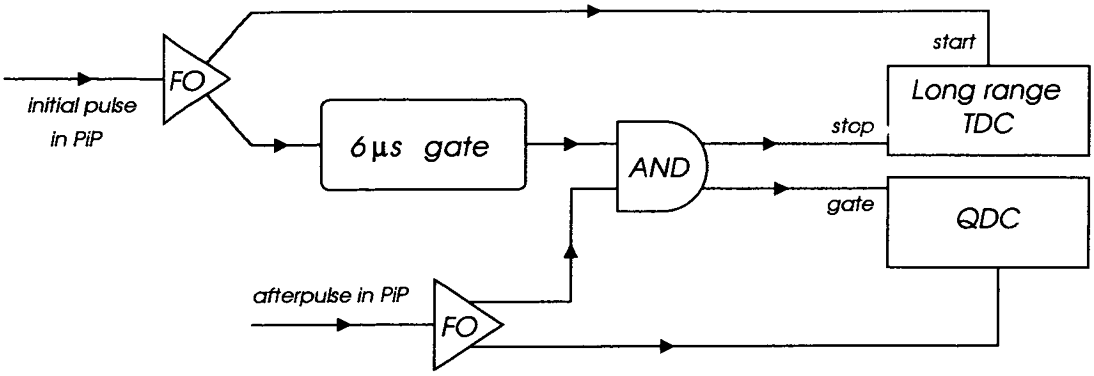

Figure 2.10: *The afterpulse trigger logic*

commences, otherwise the ADCs are fast cleared and the trigger logic is unlatched. At this stage the dead-time has been heavily reduced. The data acquisition also affects this dead-time considerably, as will be examined in the next section.

2.6.2 Data Acquisition

The data acquisition system is the part of the set-up responsible for controlling the collection of information from the electronics modules. It must be capable of doing three things. First, it must be able to initialise the electronics modules, and load up any programmable settings they might need. Secondly it must be able to read out data from the modules. Lastly it must be able to order this information into a useful format, and transfer it for storage and on-line analysis.

The computer used is an Eltec E7, housed in a VME crate. This runs an OS9 operating system and acquisition software "ACQU" [Ann] written in the computer language C. Two-way interfaces with the electronics crates enable information to be sent both to and from the relevant modules. The data thus collected is then sent via the ethernet to a VAX station for on-line analysis and storage.

The ACQU code has several different parts. The **vme_supervise** initialises the hardware, loads programmable settings and monitors the system. Different trigger settings can be introduced using this by changing the PLU requirements. The **acqu** process is the one which loops round and reads out the modules. It provides a list of ADC indices and contents, then returns to wait for another event. The **store** process transfers this data list over to the VAX on-line analysis computer, and **control** interfaces with the user to start new runs or pause acquisition.

Once the data has been sent to the VAX machine in the experimental control room, the **vme_server** process writes it to disk. The **sort** process is used for elementary diagnostic analysis and **control** is used to display graphs etc. generated by this. In this way, the efficient running of the experiment can be tested quickly and effectively, so that any problems can be ironed out.

Chapter 3

Calibration of Detectors

3.1 General Remarks

Once the experimental run is over we are left with a handful of data tapes containing vast amounts of raw information. This information is in the format of ADC identification numbers and each ADC's contents. The next job is to convert these vast arrays of numbers into meaningful information such as a particle's type, position, angle and energy. This requires calibration of the detector systems and will be the subject of this chapter.

As explained earlier (in section 2.6) an ADC can store information of two distinct types. As a QDC it stores a digitised version of the pulse height of a photomultiplier tube. This can be used to establish a particle's energy. Acting as a TDC however, it can record digitally the time of the pulse relative to some start time for the reaction. This information is useful for determining a particle's position and thereby angle relative to the target. The initial treatment of both these types of information will be looked at next, followed by an in depth look at each detector calibration method. The chapter will then conclude with a discussion of how to check and monitor the performance of the detectors.

3.2 Initial Corrections to Data

The value stored in a QDC is not in fact directly proportional to the signal from the PM tube. This is due to an ever-present constant offset or pedestal. The value for this can be trivially obtained by viewing a QDC's raw spectrum and the pedestal value can be subtracted off to give the proper pulse height.

From these pulse heights at either end of a block we must establish the light deposited in that block. However a simple summing of the pulse heights is not enough because light attenuation in the block affects the amount collected at each PM tube. In other words, there is a position dependence on the light collection. As a first approximation we assume this attenuation to be exponential. This leads to the relation:

$$Light\ produced \propto \sqrt{(pulse\ height\ 1)\ *\ (pulse\ height\ 2)} \tag{3.1}$$

i.e. the light generated in the block is proportional to the geometric mean of the pulse heights. In actual fact, the light attenuation is not exponential and we are left with a residual droop correction to make. This is done from the data by fitting a polynomial to a plot of the geometric mean versus position along the block. This now gives us the relation:

$$Light\ produced = constant \times \frac{\sqrt{(pulse\ height\ 1)\ *\ (pulse\ height\ 2)}}{f_{droop}(x)} \tag{3.2}$$

where *constant* is the constant of proportionality between light generated and pulse height geometric mean and $f_{droop}(x)$ is the droop correction dependent on position along the block, x.

Another effect that has to be compensated for is that of quenching of the pulse signal. When a particle reaches the end of its track in a plastic scintillator its energy loss per unit length increases rapidly. This leads to a higher ionisation density in the scintillator which gives this "quenching" effect whereby the light output is no longer proportional to the energy deposited by the particle. This effect is dependent on particle type and also on scintillator type. We derive the energy deposited from the light measurement and this can in general be solved by iteration [Cra70], although in the case of lighter particles such as pions a constant factor added to the last scintillator layer value is enough.

Any particle emitted from the target will also lose energy between the target and the detector in the air in between. It will also lose energy between layers of the given detector. This energy loss is calculated using the range method. Expressed simply:

$$T = (\frac{R}{a})^{\frac{1}{k}} \tag{3.3}$$

where a and k are parameters relating to particle type and medium traversed, T is the particle's kinetic energy and R is its range. Trivially the energy loss is the difference between initial and final kinetic energies calculated before and after the particle's journey through the given medium.

The signals in the TDCs are derived from leading edge discriminators. These were chosen for financial reasons but they lead to a problem. In these discriminators the time recorded depends on when a signal reaches and exceeds a certain threshold. Therefore if a large and a small pulse were to arrive at the same time, the small pulse would appear to arrive later since it will take longer to reach this constant threshold. This effect is called *walk* (see figure 3.1) and can be quite large but can be corrected for.

We can use the formula:

$$t' = t + r(1 - \sqrt{\frac{a_0}{a}}) \tag{3.4}$$

where t and t' are the measured and adjusted times (in TDC channels), a and a_0 are the pulse height and discriminator threshold (in QDC channels) and r is the pulse rise time (the time it takes the pulse to increase by a defined amount of its size). There will be more details of how this analysis was done in each detector in the relevant sections ahead.

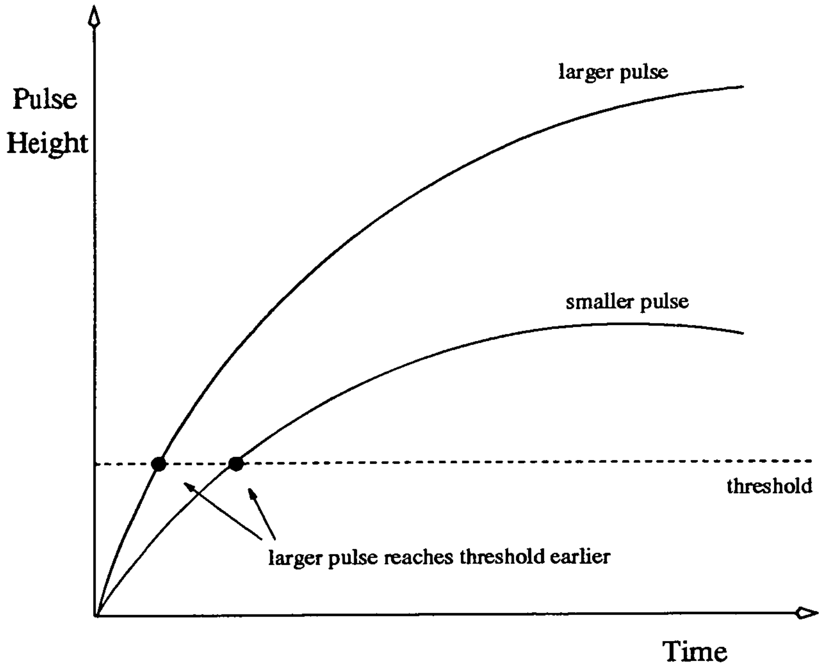

Figure 3.1: *Schematic showing walk effect*

3.3 The Photon Tagger

The photon tagger uses three hundred and fifty-two Focal Plane Detector (FPD) elements to measure the energies of residual electrons from the bremsstrahlung radiation created at the radiator. The paths of these electrons are bent in the spectrometer's magnetic field, and the place of arrival at the focal plane determines the electrons' energies. The strength of this magnetic field is continually monitored using a Nuclear Magnetic Resonance (NMR) probe inside the spectrometer. This value combined with accurately recorded field maps gives the magnetic field distribution. With this information, the small range of electron energies for each FPD element can be calculated. Given this and the value of the original electron beam, the relative photon energy is easily calculated.

3.4 The PiP-Side ΔE-Ring

The ΔE-ring on the PIP side of the target is essential to the whole identification of reactions in the target. This ΔE gives the start time for an event. The event start time should have a fixed relation to the actual reaction start time, however in practice, due to several factors it does not. The three factors to be corrected for are the difference of the transit time for particles from the target to the detector; walk effects (as described earlier) in the discriminators; and misalignment in the relative timing of the seven detector elements in the ring.

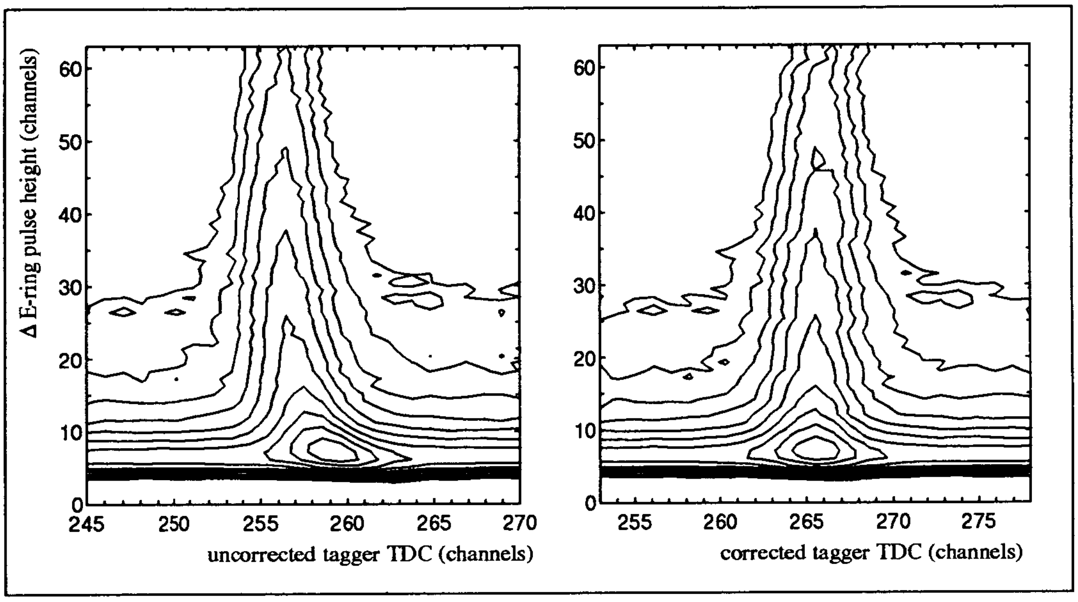

Figure 3.2: *Walk correction in the start detector*

The first of these, the transit time, depends on the particle's velocity over the target-detector distance. It transpires that this difference is negligible for the energy range of pions we are investigating in this thesis (30 MeV to 180 MeV). To establish the walk correction, the pulse height from a ΔE element was plotted against a tagger element TDC. The difference in the transit times of the photon (travelling from the radiator to the target) and the electron (travelling from the radiator to the tagger's FPD) should be constant as both particles are relativistic. It is clear from the curving ridge of figure 3.2 that they are not. However, walk in the tagger TDC is minimal due to using dual high/low threshold discriminators and because the electrons have a small range of pulse heights. This leaves the main cause for the difference with the Start Detector pulse height as the walk in the Start Detector discriminator. With the threshold obtained, the rise time is calculated to correct for this walk. As can be seen in the corrected TDC plot, the ridge is now straight indicating the validity of the corrections used.

3.5 PiP Calibration

The PiP detector is used to detect pions. Their energy is derived from the light collected within the detector's scintillator blocks. Their position is obtained from the time difference between signals in the PM tubes at either end of a block. Pion identification is carried out by using the afterpulse method.

3.5.1 Position

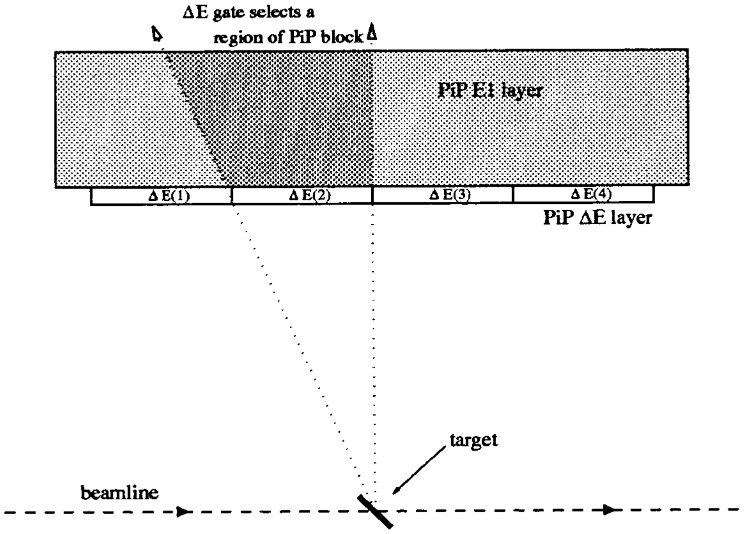

Figure 3.3: *ΔE Gating for PiP position calibration*

The position of a particle hitting a PIP block relative to the block's centre is given by the time difference of the block's pulse at either end:

$$\begin{aligned} t_2 - t_1 &= 2d/v + constant \\ \Rightarrow d &= [factor \times (t_2 - t_1)] + constant \end{aligned} \tag{3.5}$$

where d is the distance from the block centre. The next step is to establish what these calibration coefficients actually are.

First we plot four time difference spectra for an E block, each one requiring a hit in a different one of the ΔE (vertical) elements (figure 3.3). When shown together the overlap of adjacent spectra indicates the join between two adjacent ΔE strips (see figure 3.4). Thus we have the values in time difference channels which relate to three well-defined positions at the overlaps. In the past, Monte Carlo simulations have shown this method to be accurate enough for our purposes [Wal89].

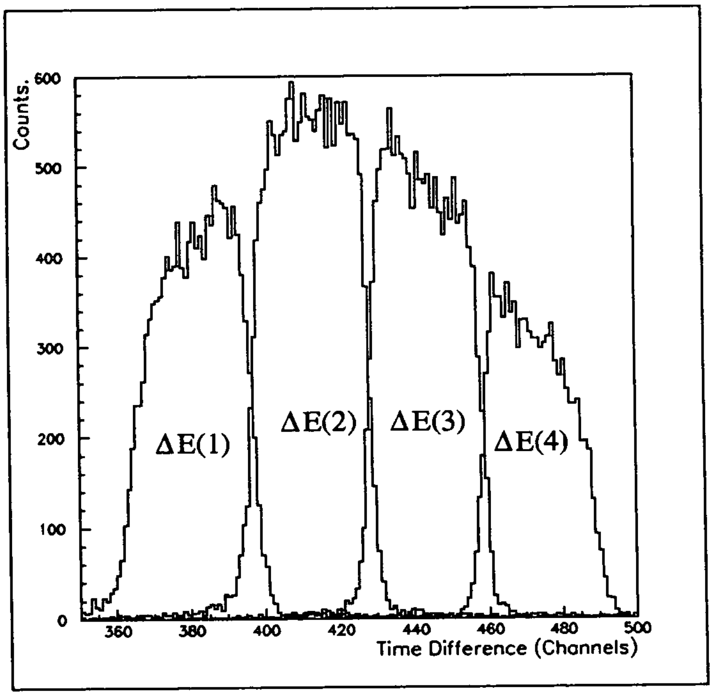

Figure 3.4: *The four differently gated time spectra*

The ΔE elements are simply calibrated using the conjugate of this process.

That is to say, gating on a hit in a different E block and plotting the time difference in the ΔE element. With this horizontal and vertical calibration done the particle's trajectory can now be expressed in terms of θ (the horizontal angle of the particle relative to the beamline) and ϕ (the azimuthal angle of the particle from the horizontal reaction plane).

3.5.2 Energy

An initial energy calibration for the PIP detector was done using cosmic rays as follows. These highly energetic, minimum ionizing muons travel downwards through a layer of PIP. If such an event is detected during an experiment it is recorded and the path length of the muon through the detector is calculated from its angle. If we normalise the pulse height mean $(\frac{\sqrt{pulse\ height_1 \times pulse\ height\ 2}}{cm})$ and plot it against position, we can derive a droop correction as described earlier. A plot of corrected pulse height mean has a characteristic Landau distribution. The light output half way up the leading edge of this distribution is known to be equivalent to 1.87 $\mathrm{Me}V_{ee}$/cm. Furnished with this knowledge we now have an energy calibration for the PIP detector. This can be checked by the analysis of Hydrogen data from a CH_2 target which has well-known two body kinematics. This is described fully in section 3.7.

3.5.3 Pion Detection

The identification of positive pion events in PiP is a two part process. Firstly, both positive and negative pions are separated from protons and electrons. Secondly the π^+ particles are distinguished from the π^-. The pions can be extracted from the collection of PiP signals using a dE-E plot, a typical example of which is shown in figure 3.5.

This shows the amount of energy deposited in the thin ΔE detector, dE, against the total energy of the particle, E. Because particles of different mass deposit different amounts of energy in the ΔE, this plot splits up the different

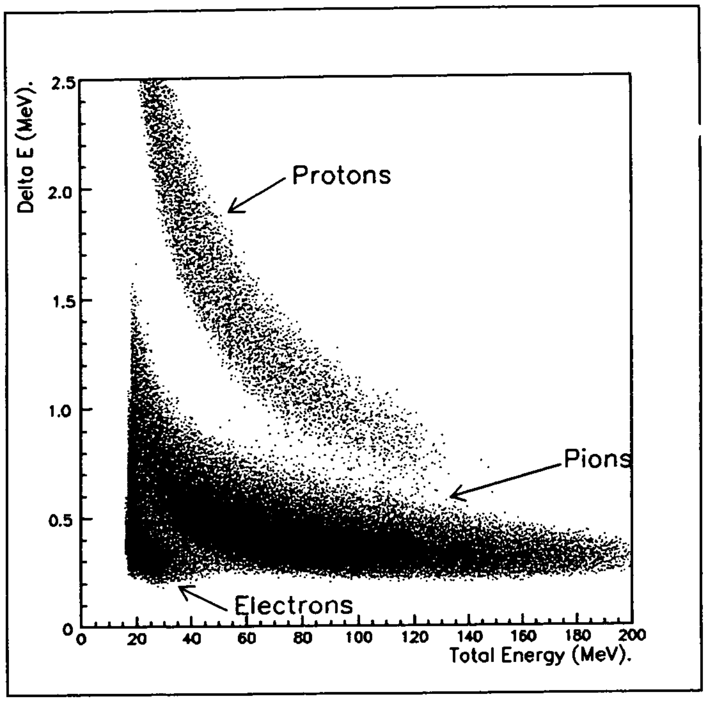

Figure 3.5: *Particle separation by dE-E plot*

particles into separate ridges.

The pion ridge shown contains both π^+s and π^-s and the positive pions can be distinguished by their decay mechanism as follows. The decay of the π^+ particles takes place in two stages, namely:

$$\begin{aligned} \pi^+ &\rightarrow \mu^+ + \bar{\nu}_\mu \\ \mu^+ &\rightarrow e^+ + \nu_\mu + \bar{\nu}_e \end{aligned} \tag{3.6}$$

Inside the detector negative pions are quickly absorbed onto nuclei in the scintillator material whereas positive pions are allowed to decay. The first part of the above decay has a half-life of 26 nsecs which is too small to be resolved by the detector. We can however make use of the second part of the decay which has a half-life of 2.2 μsecs. In this decay, most of the positrons are produced with high enough energy to exceed detector thresholds.

As described in section 2.6, a long-range TDC is used to record these afterpulses from the muon decays. At the point of an initial pulse in the detector the TDC is started and left open for an inspect time of 6 μsecs. It is stopped every time it receives an afterpulse for up to three afterpulses. This inspect period leads to a number of random afterpulses being detected. These randoms are reduced by several means.

Firstly, if another particle enters PiP within the inspect time it will give a signal in the ΔE detector on the PiP side. Thus we can use the ΔE to veto any second particle signal by simply insisting no ΔE signal is present. Also we expect a pion to decay near to where it stopped in the detector. Therefore in off-line analysis the blocks in which both the pion signal and the afterpulse were detected can be compared. If they are not in the vicinity of each other the event is rejected.

We can now use the PiP energy calibration described previously to relate the light collected in the detector to the pion's energy. This is unfortunately not the case if one of two things happen. An energetic pion could simply pass straight through all the layers of PiP. The energy needed for this is about 180 MeV. Since this would mean no afterpulse would be detected, it is easy to eliminate such events from the data. A more complex problem can occur if the pion inelastically scatters off an atom in the scintillator material. If energy is absorbed or given out in such a process the light output is no longer proportional to the pion's energy. Such events "contaminate" the pion data and have to be weeded out.

In order to gauge the importance of this problem, work has been carried out on simulating pion events in PiP [Mac95]. As pions increase in energy they are more likely to undergo inelastic processes. A calibration reaction p(γ,π^+n) was used to collect a sample of "pure" pion events. These events have a PiP response consistent with that expected from the two body kinematics of this reaction. The PiP layer responses for these events were then used as a benchmark for events from reactions with the other targets. If the difference between expected and measured PiP layer response was greater than approximately 20%, the event was assumed to have undergone an inelastic interaction and was subsequently rejected.

3.6 TOF Calibration

The TOF array is used to detect neutrons on the opposite side of the experiment from PiP. The angle of the neutron is calculated from the position of the bar in TOF which is hit and where along its (vertical) length the hit occurs. The time of flight technique is used to establish the neutron's energy, making timing measurements and walk corrections of paramount importance. A ΔE detector on the TOF side is used as a veto to select neutrons.

3.6.1 Position

The position calibration is relatively simple for the TOF array. We plot the time difference between signals at either end of a bar then assume the ends of this distribution correspond to the ends of the bar. The actual positions of the ends of each bar are accurately measured with an ultrasound device. This comparison gives us the azimuthal out of plane angle, ϕ, and the neutron's angle in the reaction plane relative to the beamline, θ, is simply determined from which bar gave a signal.

3.6.2 Energy

The timing is essential to the energy calibration of TOF. Walk corrections were carried out using LED flashers which were actually installed in the array to monitor possible gain drifts in the bars (more of this later in section 3.7). These LEDs simultaneously flash a pulse into each bar and start the corresponding TDC. This gives a fixed time difference between when the light was emitted and when it was detected, causing a peak in the TDC spectrum. If we then vary the amplitude of the signal this peak shifts because of walk in the discriminator. As before, by plotting QDC against TDC we can see this walk, extract the rise time and correct for this effect. Figure 3.6 shows that this correction straightens out the ridge, confirming its validity.

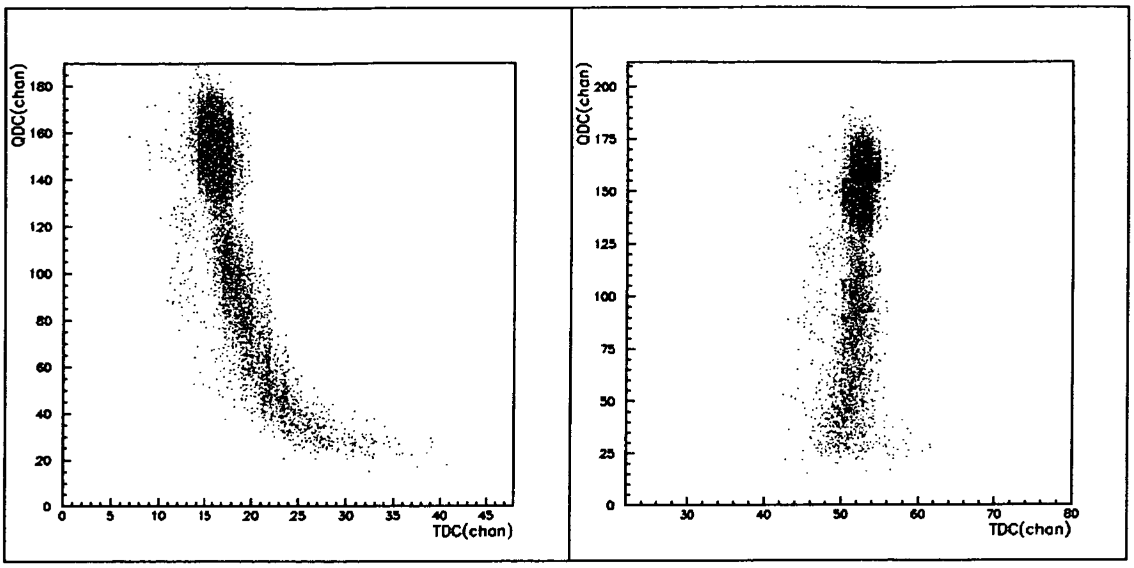

Figure 3.6: *TOF walk correction*

With the walk correction done we can establish time of flight for the neutron:

$$tof = t_{mean} - t_{zero} \tag{3.7}$$

where t_{mean} is the average time of the two signals in the PM tubes of a bar. It can be converted from channel space to nanoseconds using a precise pulser to establish the relationship. t_{zero} is the point in the t_{mean} spectrum which corresponds to zero time of flight. It is found using the "gamma flash" of relativistic particles.

These particles form a spike in a TDC spectrum because they have all travelled similar flightpaths at the same speed, c. If we plot t_{mean} - $(flightpath/c)$ instead of just t_{mean} (see figure 3.7) this spike or gamma flash is projected back onto t_{zero} and the time of this can simply be read off the axis.

Once we have the time of flight of a neutron it is a small step to find its kinetic energy, T, via the relations:

$$\beta = flightpath/(tof \times c)$$

$$\begin{aligned} \gamma &= \frac{1}{\sqrt{1-\beta^2}} \\ T &= (\gamma - 1) \times m \end{aligned} \tag{3.8}$$

with m the neutron's rest mass. This method is not exact for charged particles which lose energy during flight. A correction has to made if such particles are to be considered.

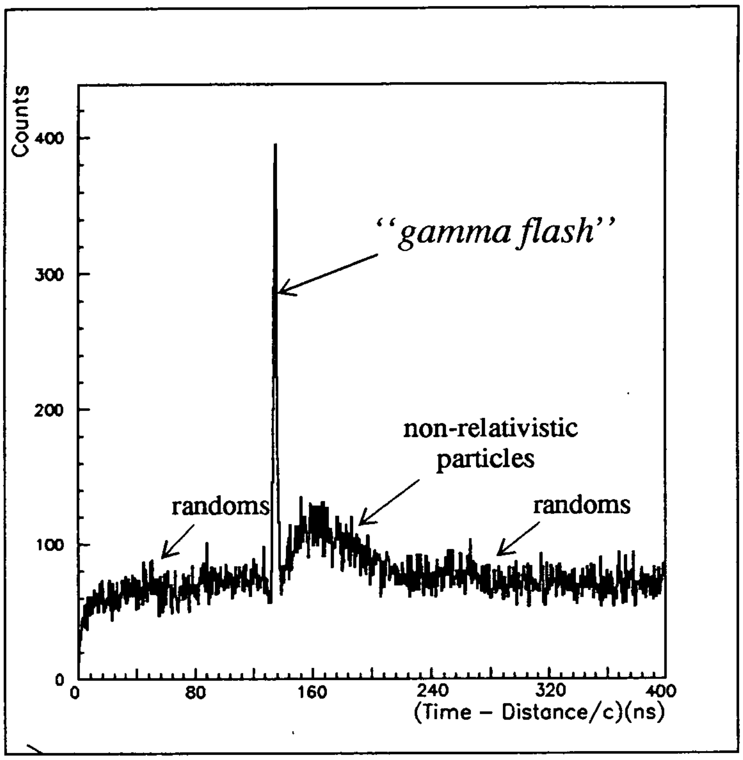

Figure 3.7: t_{zero} *calculation*

Just because the energy of the neutron is derived from its time of flight, this does not mean that the light collected in the detector is not used. It is needed to establish neutron detection efficiency. This efficiency depends on the software threshold imposed on each bar. These thresholds should be uniform in MeV_{ee} for every bar end, and to ensure they are we use a similar technique to that which used cosmic rays in PiP. Instead of cosmics, an Am/Be radioactive source was used which provides gamma rays with a known Compton Edge at 4.2 MeV. Similar to the Landau distribution of cosmic rays, this fixed point enabled the calibration coefficients to be found.

3.7 Detector Performance and Monitoring

3.7.1 Calibration Reaction

To check and refine all these calibrations, a calibration reaction p(γ,π^+n) was carried out. This was done using the Hydrogen in a CH_2 target. Since there is no residual nucleus in the Hydrogen case the two body final state is well-defined. In other words if the gamma energy, E_γ, and one other variable (say, pion solid angle Ω_π) is known, all other kinematical variables can be derived. In this way we can compare derived values for variables such as pion energy (T_π), neutron energy (T_n) and neutron angle (Ω_n) with the directly measured values.

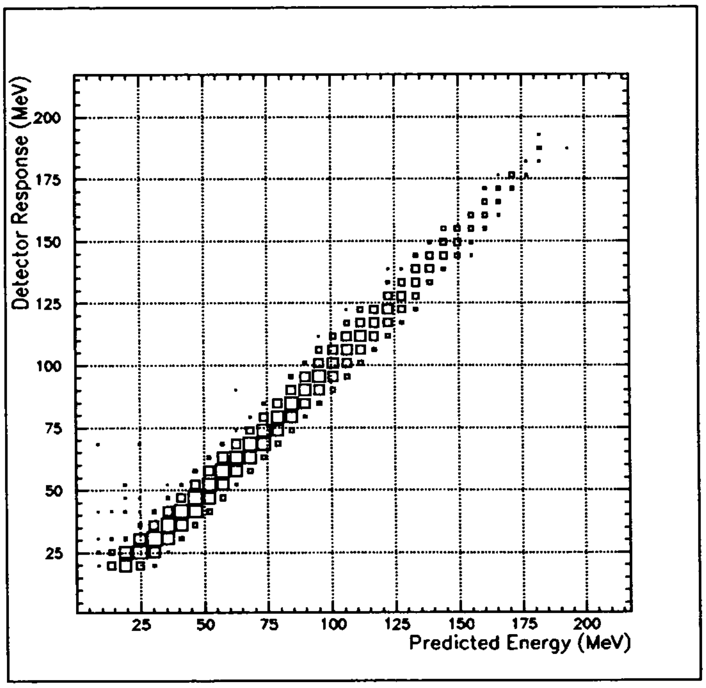

Figure 3.8: *Predicted vs measured pion energy ridge*

As well as checking our previous calibrations this can also be used to establish the energy and angular resolution of each detector which will eventually lead to the overall resolution of the experiment. This is vital information affecting how well we can describe the experiment which has been carried out.

First the measured values were plotted against their predicted counterparts, an example of which is shown in figure 3.8. From this, the difference between measured and predicted was plotted (see figure 3.9). The resolution of the predicted energy values, σ_{pred}, is derived from a Monte Carlo simulation, and the resolution of the difference, σ_{diff} between measured and predicted can be simply read from the plot. With these two values, we can unfold the measured resolution, σ_{meas} by using:

$$\sigma_{meas} = \sqrt{\sigma_{diff}^2 - \sigma_{pred}^2} \tag{3.9}$$

Using this method, a value for the pion energy resolution of 7 MeV FWHM (Full Width Half Maximum) was obtained.

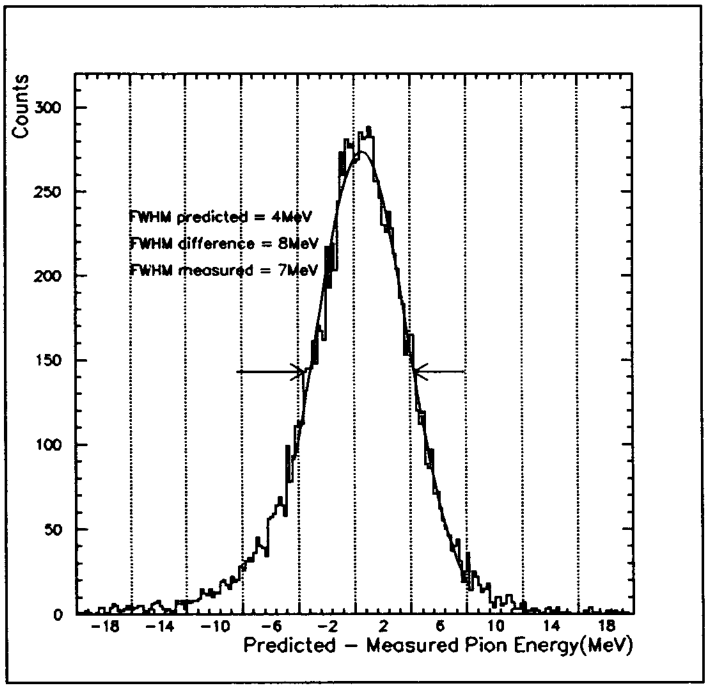

Figure 3.9: *Pion energy resolution peak*

The pion angular resolution depends on the position resolution of the ΔE and E layers of PiP. The horizontal E layers have a position resolution of about 3 cm giving a full width angular resolution of about $\Delta\theta_\pi \sim 3°$. The vertical ΔE layer has a much poorer position resolution of 9 cm leading to a full width angular resolution $\Delta\phi_\pi \sim 10°$.

In a similar process to the pion energy case, the neutron's energy resolution can be unfolded from equation 3.9 to give $\Delta E_n \sim 3.5$ MeV (see figure 3.10). The neutron angular resolution is mainly derived from the TOF bar width of 20 cm. At a distance of 4 metres this gives a full width angular resolution of ~ 2°.

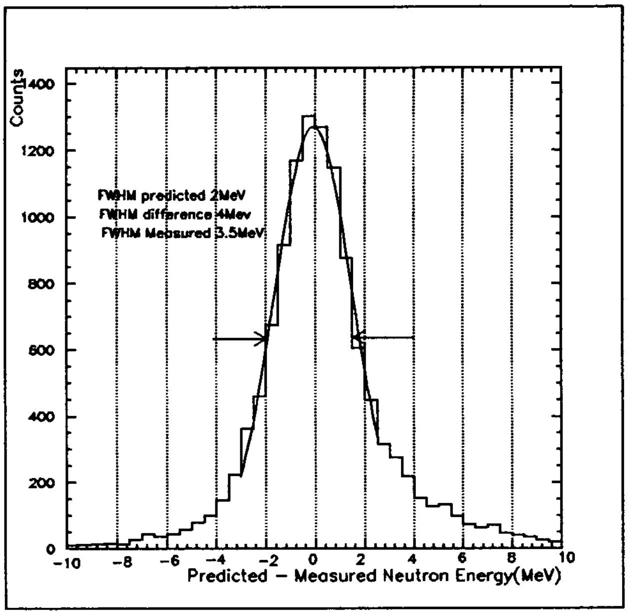

Figure 3.10: *Neutron energy resolution peak*

In the next chapter we will see how measurements and resolutions are combined into meaningful quantities such as missing energies and cross-sections and how the overall accuracy of the experiment can be gauged.

3.7.2 Gain Monitoring

Having established the performances of the different detectors, it is equally important to monitor these performances over time. If a detector's response varies during an experiment perhaps due to overheating, equipment damage, humidity etc., then this can seriously affect the quality of the data set and this has to be compensated for.

The monitoring of the gains of each block in PiP and TOF is done using LEDs. These are implanted in the plastic scintillator and fire light pulses of known amplitude into each block. By periodically monitoring the pulse and the detector's response to it, a ratio for any relative gain shifts can be established. The beauty of the LED system is that it produces a very narrow peak meaning the gain can be watched over short timescales (a matter of minutes) as well as longer ones (months or even years). It transpired that gain shifts over the length of our experiment were minimal needing only a small correction of less than 2%.

Chapter 4

Data Analysis

4.1 General Data Reduction

So far we have seen how the current experiment has been set up and performed, and how each detector system has been calibrated. The next step is to take the data and convert it into some meaningful and useful form for presentation and for displaying the most amount of information about the reaction under investigation. Here we introduce the concept of the cross-section. In this thesis I will present differential cross-sections for the (γ,π^+n) reaction on ^{6}Li, ^{12}C and ^{40}Ca targets in comparison with the theoretical Oset *et al.* simulation code. To reach this stage various things have to be done, namely:-

- Selection of the π^+n channel
- Account for randoms in the data and background values
- Account for detector efficiencies
- Incorporate knowledge of photon flux and target density
- Make calculations with the Oset code for comparison

This chapter will deal with each of these items in turn starting here with a brief synopsis of the analysis code and the method of selecting the correct reaction channel.

4.1.1 ACQU Analysis Code

The ACQU [Ann93] analysis code was developed at the University of Glasgow as a general code for the analysis of all experiments in the A2 PiP-TOF collaboration. Each experiment has different problems however, and this "bare-bones" code must be adapted and developed by the individual user to suit their own needs. The general ACQU code does all the things common to such analysis codes such as reduced data output, tape handling and spectra display options. Further work is done by code written by the user in 'C' in the form of user-defined spectrum (uds) functions.

In the case of the (γ,π^+n) experiment a tree-like structure of code has been developed. This takes the experiment as a whole at the top of the tree structure. This is then split into the four separate detector systems (including the ΔE) which are further divided into layers and then into blocks - the basic constituents of each detector. The code in this format has a neatness and efficiency, looping round each block in a layer, each layer in a detector and each detector in the experiment in turn.

Information in the ADCs and TDCs is analysed in this way with data being processed and the vast array of calibration coefficients being included at this stage. The output then fills the data structure ready for histogramming and further detailed analysis by these uds functions. At this stage the data can also be loaded into the CERN analysis package PAW++ [PAW] for advanced analysis and presentation purposes.

4.1.2 Data Reduction

From the vast amount of data we obtain, we must try and isolate (γ,π^+n) events. This has already been partially done at this stage using hardware cuts and specific triggers (as explained in section 2.6). However one must be cautious in using these hardware cuts since there is a possibility of removing valid events. It is always better to do further cuts on the data using the software since such cuts are reversible. Consequently, the hardware cuts are not made too severe.

The first reduction at this stage is to remove calibration events from cosmic rays and flasher LEDs. This is simply done by reading the trigger type for an event and rejecting events with a cosmic or flasher trigger. Next we must identify positive pions in PiP and neutrons in TOF.

The pions are selected in PiP by cutting on the pion ridge in the dE-E plots as described in section 3.5. These are positively charged pions due to the requirement of an afterpulse in the trigger. This still lets in a lot of low energy electrons which are cut out using a software threshold on the pion energy of $T_\pi > 30$ MeV. This leaves us with around 90% of events as pure π^+. The remainder can be dealt with by random and background subtractions as explained in the next section.

Neutrons are selected in TOF using the ΔE ring on the TOF side as a veto detector. If a signal is detected in a TOF stand we look at the respective ΔE signal. A spectrum of such signals has a peak due to charged particle signals. We only keep the event as valid if there is no signal in the peak area of the ΔE spectrum. There are of course some random events under this peak and a correction must be made for such rejected events. The photons, also neutral, can be easily rejected because their relativistic nature means they give signals that contribute to the gamma flash peak of the TOF spectra.

4.2 Subtraction of Randoms and Background

At this stage we had identified what we believed to be (γ,π^+n) events but there still remained a residual contamination of the data by randoms and background. Randoms are uncorrelated hits in any one of the detector systems which provide a trigger for the experiment. The tagger has random electron hits on its focal plane, PiP contains random particles which can generate an afterpulse and TOF has random particles firing blocks in its array.

The method of eradicating the effects of these randoms is to take a separate sample of purely random events. These samples are given a relevant negative weight and combined with the data sample to provide a so-called "random subtracted" data set.

These randoms cause multiple hits in each of the detectors i.e. for every afterpulse in PiP there could be five hits in the tagger and say two in TOF. The way to analyse these multiple hits is to take each combination separately and weight the combination according to whether each hit was a random or a prompt (correlated) hit. How these weights are derived for each detector is described in the following three sections.

There is also the subtraction of background to take into account. Background is caused by interaction of the beam with the air surrounding the target. To establish the extent of this the experiment is run with the target removed for a time. Normalising this target-out run for the different photon flux, we can then subtract it from our correlated data set.

4.2.1 Tagger

Randoms in the tagger are caused by uncorrelated electrons striking the focal plane. The weighting of randoms in the tagger is relatively simple. The tagger time spectra have peaks corresponding to correlated tagger hits. As you can see from figure 4.1, under this prompt peak lies a component of random hits. In general the random background here is not flat but exponential [Ann93], however in the experiment, the rates were kept low enough to be able to approximate a flat random component. To subtract these randoms we defined two large areas of purely random counts either side of the prompt peak. The size of these ensured greater statistical accuracy. Next we simply note during analysis which area a hit has come from and weight it according to relative size with the prompt weight made equal to one and the random weight defined as:-

$$weight^{\gamma}_{ran} = \frac{-1.0 \times \Delta T_{prompt}}{\Delta T_{random_1} + \Delta T_{random_2}} \tag{4.1}$$

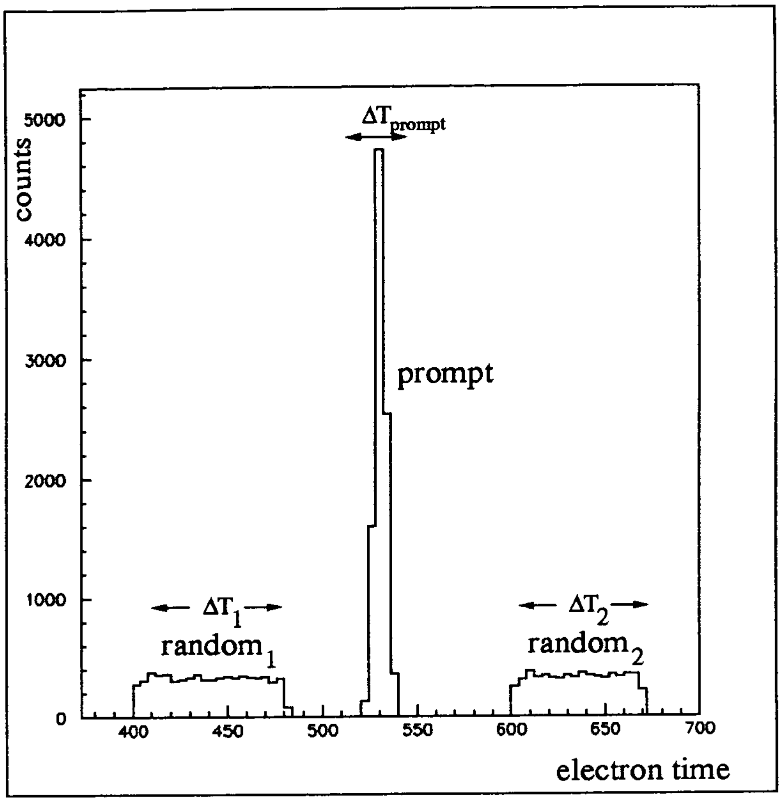

Figure 4.1: *Prompt and random regions in the tagger*

4.2.2 PiP

Randoms in PiP are defined not as "false" particles being detected but as "false" afterpulses caused by an uncorrelated particle being detected in PiP during the afterpulse inspect time. These randoms form a flat component underneath the exponential decay of the pions in the long-range TDC (see figure 4.2)

The calculation of these weights is complicated by the fact that we cannot obtain a solely random sample of events. The method adopted was as follows. The decay graph is split up into two regions nominally named *mostly prompt* and *mostly random.* We then give the respective afterpulses relative weights proportional to these two regions:-

$$weight^{\pi}_{ran} = \frac{-weight^{\pi}_{pro} \times (b-a)}{(c-b)} \tag{4.2}$$

However since there are prompts in the *mostly random* region (and vice versa)

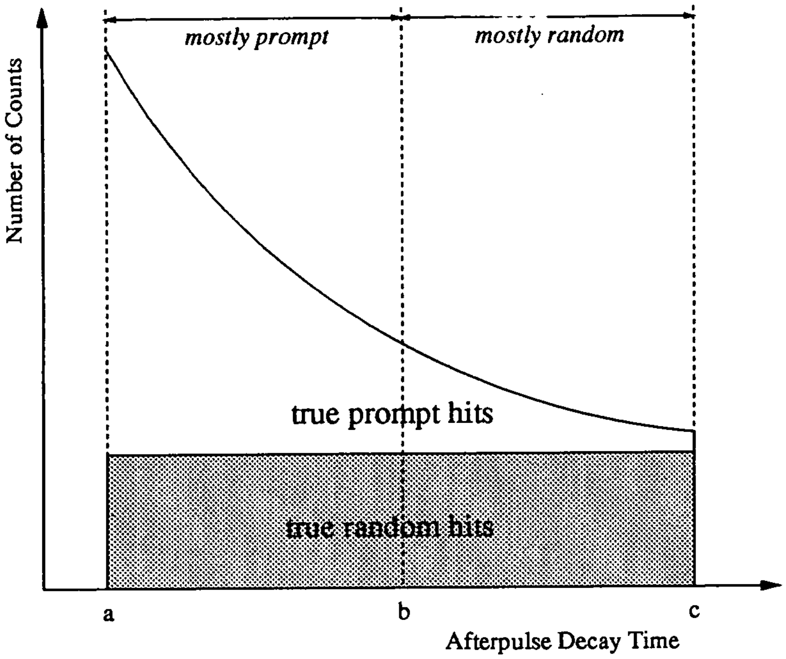

Figure 4.2: *Prompt and random regions in PiP*

we are removing some bona fide prompt events in doing this. To compensate for this we have to set the weight for the prompts at greater than one. Exactly what we set it to is established as follows. If we make the demand that the weighted sum of all events must give us the correct number of prompt events (the number of events above the flat background), then the size of the prompt weight can be derived as [Owe94]:-

$$weight^{\pi}_{pro} = \frac{1 - e^{-(c-a)}}{\{(1 - e^{-(b-a)}) - \frac{(b-a)}{(c-b)}(e^{-(b-a)} - e^{-(c-a)})\}} \tag{4.3}$$

4.2.3 TOF

Randoms in TOF are dealt with similarily to those in the tagger. A sample of purely random events is easily obtained from a time of flight spectrum. These randoms correspond to events beyond the valid time range i.e. a neutron with such a low energy would not be able to achieve the threshold imposed on the detector's signal. Since the "real" events occupy a lot of the range of the TDC these random areas are smaller and must be weighted accordingly. In parallel with the tagger case we define the prompt weight as one and the random weight as:-

$$weight^n_{ran} = \frac{-1.0 \times \Delta T_{prompt}}{\Delta T_{random}} \tag{4.4}$$

4.3 Efficiency Calculations

We have now obtained a background and random subtracted set of data for the reaction channel of our choice. To reach the point of describing the experiment with cross-sections and meaningfully comparing the data with theory we have to establish the relation between our data and what actually occurred in the experiment. In other words we have to establish the efficiencies of each of the detector systems in detecting their specific particle. These efficiencies were calculated in different ways for each of the three systems and this section describes each of these methods in turn.

Once these efficiencies are established they are read in during analysis at the same time as the event weights described earlier to give an overall normalised weight for each subevent. With these weights we can then move on to presenting cross-sections and realistically comparing our data with theory.

4.3.1 Tagger

The method for establishing the tagging efficiency is described in section 2.3. The efficiency is given as:

$$\epsilon_{tagg} = \frac{\text{number of coincidence hits}}{\text{total number of tagger hits}} \tag{4.5}$$

where a Pb glass detector is used for a time to detect the number of photons in the beam. This tagging efficiency is dependent on the energy of the photon. This is because the higher the photon's energy in the beam, the smaller the angular cone going forward and the less collimation it undergoes. Figure 4.3 shows the tagging efficiency as a function of photon energy. The two areas of low signal in this plot ($\sim$ 600 MeV and $\sim$ 740 MeV) are due to the phototubes in those areas having worn out slightly, thus giving reduced values for efficiency.

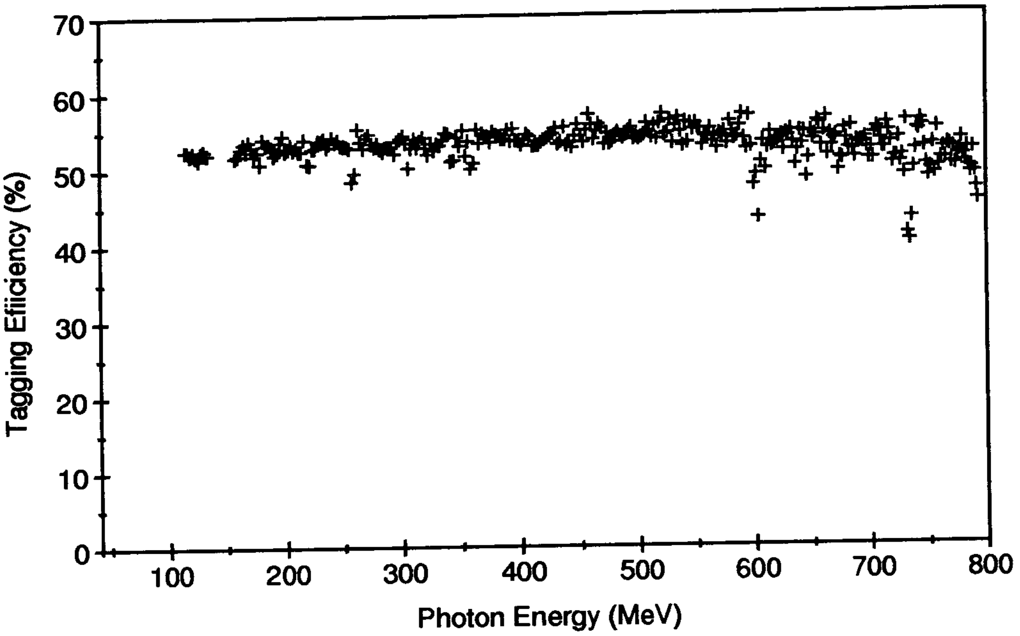

Figure 4.3: *Tagging efficiency versus photon energy*

4.3.2 PiP

Section 3.5 described how pions were detected using the PiP detector and how contaminating data was extracted from the data set, but how efficient is PiP at detecting these particles? We can express the pion detection efficiency as the probability that the pion generates an afterpulse $P_{\pi^+}(after)$ and that it also does not inelastically scatter within the detector $P_{\pi^+}(no\_scatt)$. The laws of probability lead us to:

$$\epsilon_{\pi^+} = P_{\pi^+}(after \cap no\_scatt) \qquad (4.6)$$

$$= P_{\pi^+}(after).P_{\pi^+}(no\_scatt|after) \quad (4.7)$$

where $P_{\pi^+}(no\_scatt|after)$ is the probability that the pion hasn't scattered given that there was an afterpulse. These two probabilities were calculated as follows.

Using the Hydrogen data and the calibration reaction a data set with no afterpulse required was obtained. For a certain predicted pion energy the number of detected neutrons was then noted. This was repeated with the afterpulse condition imposed and the probability of generating an afterpulse is simply the ratio of these two amounts of detected neutrons.

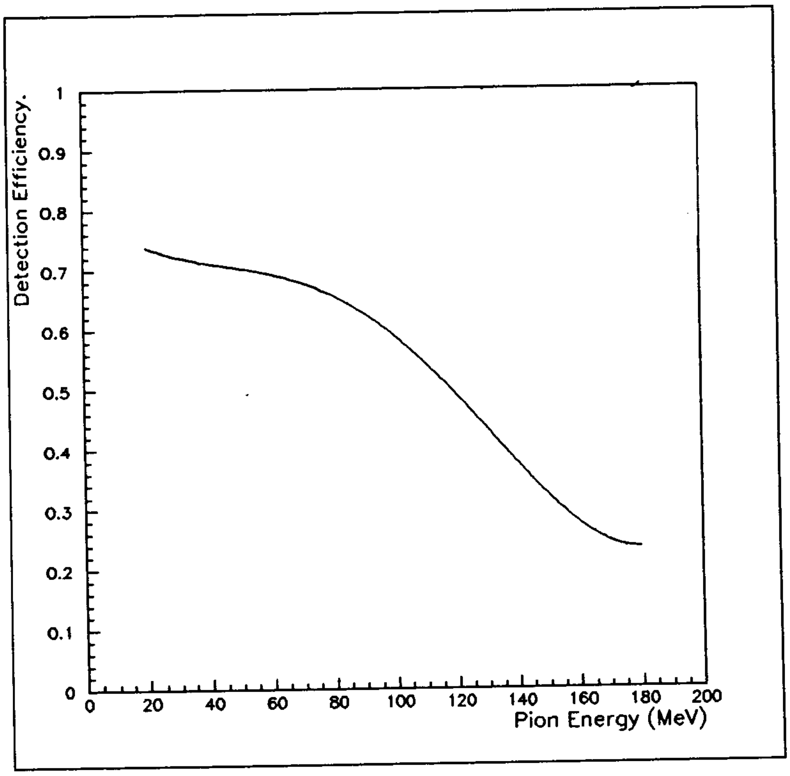

Figure 4.4: *Pion detection efficiency*

The second probability was established in similar fashion. Data were taken with an afterpulse condition on the Hydrogen target. For a set pion energy the number of neutrons was again noted. This is effectively the number of afterpulse events. The number of non-scattering afterpulse events was found from the number of events under the peak in the missing energy spectrum of the reaction. Again the probability required is just the ratio of these two numbers.

When the two probabilities are combined they give a pion energy dependent efficiency as shown in figure 4.4. The physical reason for this energy dependence is straightforward. With increased energy the pion is more likely to scatter inside the detector, either losing energy in inelastic processes or leaving the detector all together thus reducing detection efficiency.

4.3.3 TOF

Neutrons, being neutral particles, are not detected directly in TOF because they do not ionise in the scintillator material. Instead they knock out protons in the material whose ionisation is subsequently detected. This means a neutron will only be detected if it knocks out a proton of sufficiently high energy to exceed the detector's threshold. This leads to a relatively low neutron detection efficiency in TOF and an efficiency which is also energy dependent.

The average neutron detection efficiency was calculated using the STANTON [Cec79] cascade code. With a threshold imposed on the TOF bars of 5 MeV_{ee}, the results of the efficiency calculation were as shown in figure 4.5.

As can be seen in this spectrum, a rough value for the efficiency is 5%. To improve this value the TOF stands were doubled up one behind the other and even four layers deep at forward angles. In such a set up, a neutron can conceivably pass through one bar into another. The overall detection efficiency ϵ_n for a number of layers n can be obtained from the recurrence relation :

$$\epsilon_n(N) = \epsilon_n(N-1) + \epsilon_n^{bar}(1. - \epsilon_n(N-1)) \tag{4.8}$$

$$\epsilon_n(0) = 0.0 \tag{4.9}$$

where ϵ_n^{bar} is the efficiency of a single TOF bar.

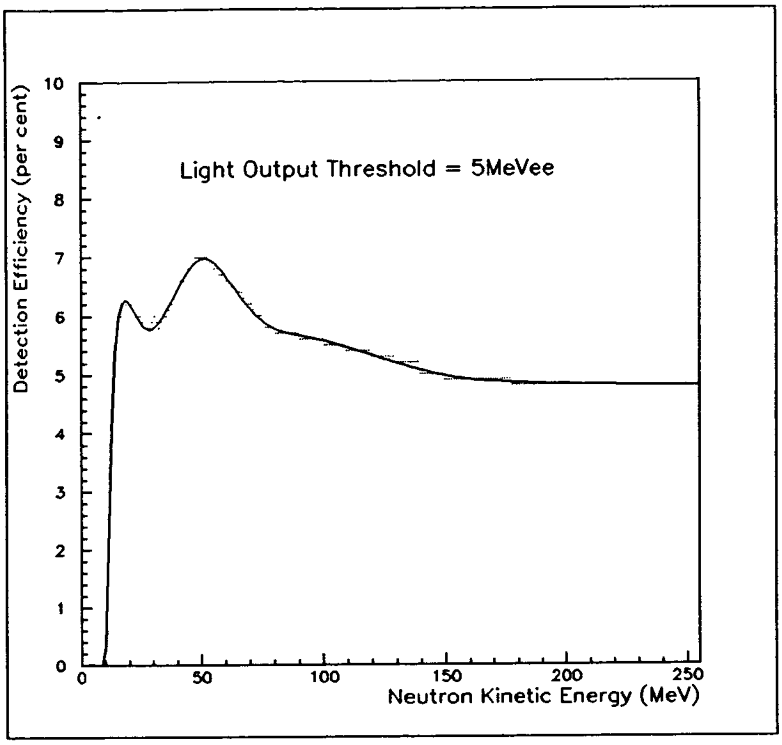

Figure 4.5: *Neutron detection efficiency*

4.4 Cross-Section Calculations

4.4.1 Derivation of Cross-Sections

With all the weights and efficiencies calculated we are now in a position to derive cross-sections. A cross-section for a reaction can be seen as an expression of the probability of that nuclear reaction occuring within certain conditions. These conditions are a well defined geometry, the flux of incident photons and the type and size of target. The cross-section is measured in units of area (typically in barns or millibarns, 1 barn = 10^{-28} m^2) and is dependent on the energy of the incident photon.

The cross section σ can be derived from the yield $\mathcal{Y}$ (the total number of nuclear reactions taking place) by the relation:

$$\mathcal{Y} = N_\gamma . n_{targ} . \sigma \tag{4.10}$$

where N_γ is the number of incident photons and n_{targ} is the number of target nuclei per unit area.

Here, n_{targ} is given by:

$$n_{targ} = \frac{N_A.\rho_s}{A} \tag{4.11}$$

where N_A is Avogadro's number (6.02×10^{23}), A is the atomic weight of the target nucleus and ρ_s is the target mass per unit area presented to (i.e. normal to) the photon beam. This is just the actual target density ρ weighted by an effective thickness of target, $\frac{t}{sin\theta_{targ}}$, where t is the actual target thickness and θ_{targ} is the angle between the target and the photon beam.

In practice it is more common to measure differential cross-sections than total cross-sections. This is because differential cross-sections tend to provide more information about the reaction than the more general total cross-sections. In the current experiments we have been analysing (γ,π^+n). This has two outgoing reaction products each of which are defined by three kinematical variables namely their energy and their polar and azimuthal angles. This gives a total of six kinematical variables. If we specify five of these six variables then the sixth cannot vary and we have defined a region of phase space to look at our reaction. Defining a cross-section with respect to these five variables we create a triple differential cross-section i.e.

$$\frac{d^3\sigma}{dT_\pi d\Omega_\pi d\Omega_n}$$

where $d\Omega_{subscript}$ is the solid angle segment for the subscripted particle in question, defined as:

$$d\Omega = sin\theta d\theta d\phi \tag{4.12}$$

and $dT_{subscript}$ is the region of kinetic energy of that particle. This cross-section is merely an example, obviously other combinations of the six kinematical variables are also possible.

This well defined triple differential cross-section leads to problems of its own.

From the original cross-section concept (all particles, all angles, all energies) we have differentiated down to specifying most of these variables to within small limits. Experimentally this can lead to very few events being present in each segmented "bin" of energy, angle etc. This in turn can lead to very poor statistics and the usefulness of the data in such a form can be questioned. To overcome this, it is common to integrate or sum over one or more of the kinematical variables leaving a more sensible double differential cross-section i.e.

$$\frac{d^2\sigma}{dT_\pi d\Omega_\pi} = \int \frac{d^3\sigma}{dT_\pi d\Omega_\pi d\Omega_n} d\Omega_n \tag{4.13}$$

What is essential in such an integration is to specify the region of integration so that meaningful comparison with theory can be achieved.

In this thesis the data will be presented as double differential cross-sections $\frac{d^2\sigma}{dT_\pi d\Omega_\pi}$ which were evaluated as:

$$\frac{d^2\sigma}{dT_\pi d\Omega_\pi} = \frac{\Delta\mathcal{Y}}{N_\gamma . n_{targ} . \Delta T_\pi . \Delta\Omega_\pi} \tag{4.14}$$

where the yield is established from the fully weighted data. The photon flux during the experiment was typically of the order of 10^6 per second for each element in the focal plane. The value N_γ was obtained from combining the values in the tagger scalers, $N_{e'}$, with the tagging efficiency value, ϵ_{tagg}. The values of n_{targ} were calculated for the three targets used and are tabulated overleaf in table 4.1.

Target	n_{targ}
^{6}Li	9.89×10^{23}
^{12}C	1.23×10^{23}
^{40}Ca	1.02×10^{22}

Table 4.1: n_{targ} *for the targets*

As can be seen from the cross-section evaluation, we have integrated over the range of neutron angles ($15° < \theta_n < 150°$) and energies (15 MeV $< T_n <$ 150 MeV), effectively just requiring a neutron to be present somewhere in the TOF array within the limits of the reaction plane. The other variables' ranges and bin sizes were as shown in table 4.2.

Variable	Range	Size of Bin
T_π	30-180 MeV	5 MeV
θ_π	50-130°	40°
ϕ_π	(-15)-15°	30°
ϕ_n - ϕ_π	170-190°	20°

Table 4.2: *Binning choices for variables*

The double differential cross-sections are displayed as a function of pion energy. The condition of a ± 10° difference in the azimuthal angles of the pion and neutron is imposed to only select neutrons roughly emitted in the same reaction plane as the outgoing pion.

The target-out data was analysed and proved to be only about 2% the size of the various target-in data. This was therefore neglected as this value is much smaller than systematic errors in the overall measurement which are to be discussed next.

4.4.2 Statistical and Systematic Uncertainties

For the results to have any real meaning they must come with some estimate as to their accuracy. That is to say, we must express the uncertainty in the data in some way. There are two distinct types of uncertainty involved in such experiments, namely statistical (which arise from probability and the amount of data taken) and systematic (which stem from the ability of the detector system to identify and measure the particles accurately).

The first of these, statistical uncertainties, stems from the idea that we are merely measuring the probability of something happening. To more accurately assess the probability of whether something will happen it makes sense to repeat the experiment many times. In this case the longer the experiment is run the more data is collected and the more precision we can ascribe to the measurement of the reaction. Thus more data means less statistical uncertainty. This statistical error can be simply evaluated. If we have N counts then the statistical error is commonly given by $\sqrt{N}$. However since events have been weighted in the experiment to allow for random subtractions, efficiencies etc. this case is no longer quite so simple. Now, instead of a number of counts we have a sum of weights:

$$W = \Sigma(weights) \tag{4.15}$$

and the statistical uncertainty, σ_W, in this value is given by:

$$\sigma_W = \sqrt{\Sigma(weights)^2} \tag{4.16}$$

which reduces to $\sqrt{N}$ if the weights are equal to one. The size of bin which is used to collect the data affects the level of statistical error and in practice bin sizes are chosen to give a certain level of accuracy. In this case the data has been binned to keep statistical uncertainty below 15%.

The problem of systematic uncertainties is more complex than the statistical case. They arise from the ability of the detectors to measure and identify particles. In other words, these errors stem from the uncertainties in the detector efficiency measurements and the position and energy calibrations. Each systematic uncertainty is discussed in turn below and then these separate errors are combined in quadrature.

- **The Tagger:** The tagging efficiency was measured regularily during the experiment with an uncertainty of about 3% for a single focal plane element. This can be reduced by summing over a number of data files to achieve an error of ~ 1%. There is a small error associated with the detected number of electrons in the focal plane, but as this number is of the order of 10^9, the contribution from this to the overall uncertainty is negligible and was therefore ignored.

- **Pion Detection:** The amount of data used in the pion detection efficiency calculation results in a systematic uncertainty of around 5% in the pion energy. This is compounded by an error from pions which may decay in flight before reaching PiP. Demanding consistent signals between ΔE and PiP reduces this but the uncertainty is still at the level of 5% to 10%, and is energy dependent.

- **Neutron Detection:** The STANTON cascade code which was used to establish neutron detection efficiencies has a quoted systematic uncertainty of 5%.

- **Target-based Errors:** The target density n_{targ} was calculated from measurements of the mass, size and angle of the target. Each of these was measured to a great degree of accuracy. The target angle was computer controlled and tests showed it to be accurate to within 0.2°. The overall uncertainty in n_{targ} is estimated at somewhat less than 1%. A further error arises from having an extended beam spot incident on the target. In other words, the beam is not point-like and an uncertainty as to the exact position of the reaction within the target is introduced. This was found to be negligible compared to the other uncertainties in position and was therefore neglected.

- **Position and Angular Uncertainties:** The position calibrations of PiP and TOF carry systematic errors which in turn lead to errors in the calculated angles of the particles and therefore in the size of the solid angle cut imposed. This error is approximately 6%.

- **Uncertainties from Randoms:** Random contamination is still present in the data and carries an uncertainty with it. Events may be falsely identified or discarded due to randoms in any of the detectors. Because of this, an error of approximately 5% is introduced.

To reduce the overall uncertainty, the data was normalised to previous known Hydrogen cross-sections. This overcomes many of these previously listed errors. The normalisation factor was found to be 1.25 [Mac95] from comparison with the Blomqvist and Laget model [Blo77] and the data of Betourne *et al.* [Bet68]. Betourne's results have a quoted error of 4% and the statistical error in the normalisation was 10%, all of which gives an overall value of ~ 12% uncertainty.

Since the value of this error has been established using the Hydrogen data for calibration, the only other consideration is whether similar errors apply for reactions within the various other nuclear targets which have been used here. As it turns out, most of these uncertainties are unchanged in such circumstances, however one or two are modified slightly.

Unlike the case of the well defined kinematics of the Hydrogen reaction, the double differential cross-sections of the nuclear (γ,π^+n) depend on the neutron solid angle measurement. The uncertainty in the azimuthal TOF calibration is now included and this is estimated at 5%. Also, pions decaying in flight may have been rejected in the calibration due to unmatching or unphysical kinematics in the Hydrogen case but this is not necessarily the case for other nuclei. Without this constraint a further error is introduced, being estimated at 7%. The effect of these two further uncertainties is to give a total systematic uncertainty for each of the targets of approximately 15%.

4.5 Theoretical Calculations

The theoretical comparison to the data in this thesis has been carried out using the Monte Carlo cascade code developed by Carrasco and Oset [Car94]. The theory behind this microscopic code is described in more detail in section 1.5. This code has advantages and disadvantages associated with it when comparing to this kind of experiment. The microscopic nature of the theory and the starting point of basic interaction forces is useful for examining medium effects in the nucleus. Specifically, the way it deals with pion and isobar interactions and the way in which the Δ propagates within the nuclear environment are of interest.

Unfortunately as explained in section 1.5 there are drawbacks. This microscopic approach means that the interactions occur in a Fermi sea in the nucleus. This does not contain any information on the nuclear structure. Thus comparison with for example specific shell removal in the data is not really meaningful. This is highlighted by looking at missing energy spectra for both data and theory as shown in figure 4.6, where missing energy, E_{miss}, is defined as:-

$$\begin{aligned} E_{miss} &= T_{\gamma} - T_{\pi} - T_{n} - T_{recoil} && (4.17) \\ &= E_X + Q && (4.18) \end{aligned}$$

where T_{part} is the kinetic energy of the respective particle and E_X is the excitation of the residual nucleus. The figure clearly shows (especially in the Carbon case) very different missing energies for data and theory.

The way round this problem is to compare the two over larger missing energy ranges, chosen to include all the shells. We must be careful when doing this, however. The Oset code produces π^+n events not only from quasi-free pion production on protons, but also as a result of FSI. At higher energies, it is not clear how the code treats such events, and careful consideration of the code in such circumstances must be given. A discussion of all these results and some conclusions are contained in the next and final chapter.

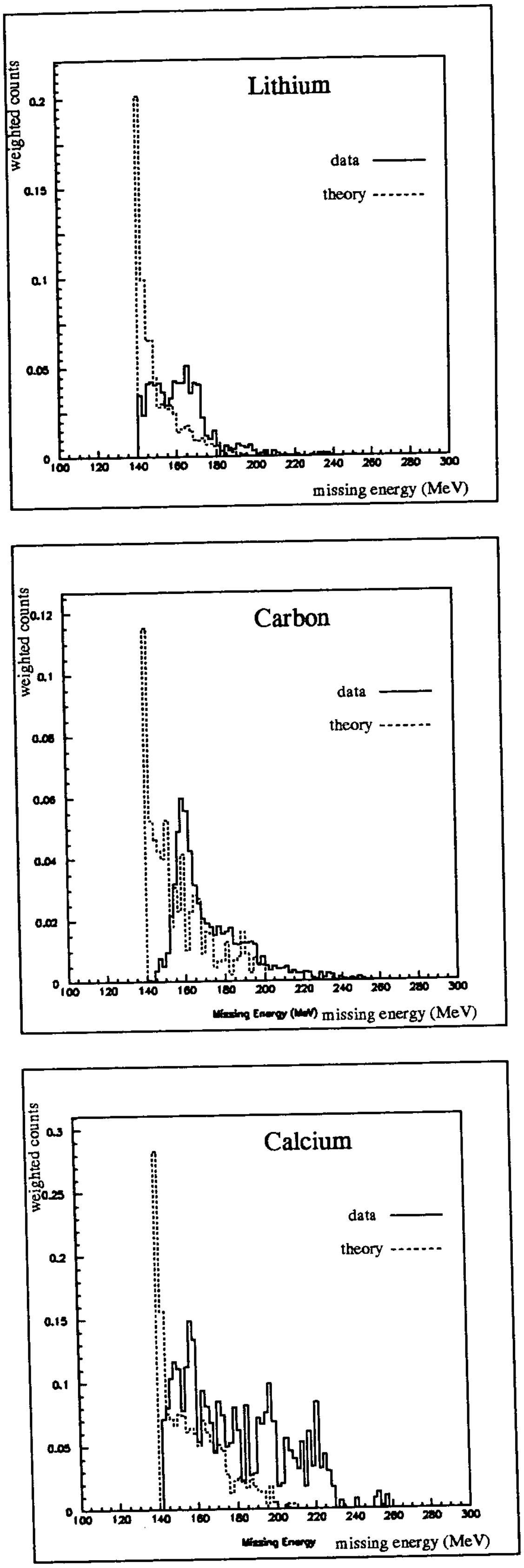

Figure 4.6: *Comparison of missing energies*

Chapter 5

Discussion of Results

5.1 Introduction

In this chapter the experimental results are presented along with results from the Oset *et al.* simulation code. There is a discussion concerning the trends and features of both, as well as some analysis of trends in the cross-section according to the mass of the targets and the incident photon energy. A discussion of the data in the context of previous results is also done. Finally, some conclusions are drawn as to the success or otherwise of the current experimental work, and some possible future experimental work suggested.

The way in which the data are presented has been chosen according to various factors. It is hoped that a balance has been reached between experimental constraints such as statistics, geometry of detectors etc. and theoretical considerations, that is, how to glean the most amount of information out of the data in the most effective way.

The data has been presented in four different photon energy ranges, with pion angles being split into forward and backward sections. It has also been integrated over the missing energy range, and over the angular and energetic ranges of the neutron. This sizeable binning of the data aids the comparison with the theory by reducing nuclear structure dependence and by ensuring good enough statistics for meaningful comparison.

5.2 Comparison of Data and Oset Code

The cross-sections that follow are split into 40 MeV photon energy regions, from E_γ = 240 MeV to E_γ = 400 MeV. The three targets are in order of increasing mass (Lithium in figures 5.1 to 5.4, Carbon in figures 5.5 to 5.8 and Calcium in figures 5.9 to 5.12) with the pion forward angle results ($\theta_\pi = 70 \pm 20°$) first, then the backward angles ($\theta_\pi = 110 \pm 20°$).

As mentioned earlier, the pion azimuthal angle is ± 15° from the reaction plane (this is restricted by the height of PiP) and there has been a restriction imposed on the difference between the two particles' azimuthal angles of ϕ_π - ϕ_n = 180 ± 10°. This is partly to avoid statistics being too low and partly because the theoretical code predicts very low amounts of reaction products outwith this planar limit.

The pion angle, θ_π, has been divided in two, effectively splitting PiP in half. This was done because investigations suggested that statistics would not suffer too greatly and it would allow the relative cross-sections of the two angular ranges to be examined. Previous investigations by Pham *et al.* of the $^{16}O(\gamma,\pi^- p)$ reaction [Pha92] found that the data agreed with a DWIA model for backward angles but were a factor of three too low at forward angles. Similarily, the overall magnitude of the experimental cross-sections was about three times lower at forward angles compared to backward angles. Although this is a different reaction under study, one would expect the trends to be similar, and a confirmation or otherwise of those findings is of great interest. The results are described for each target in the following sections.

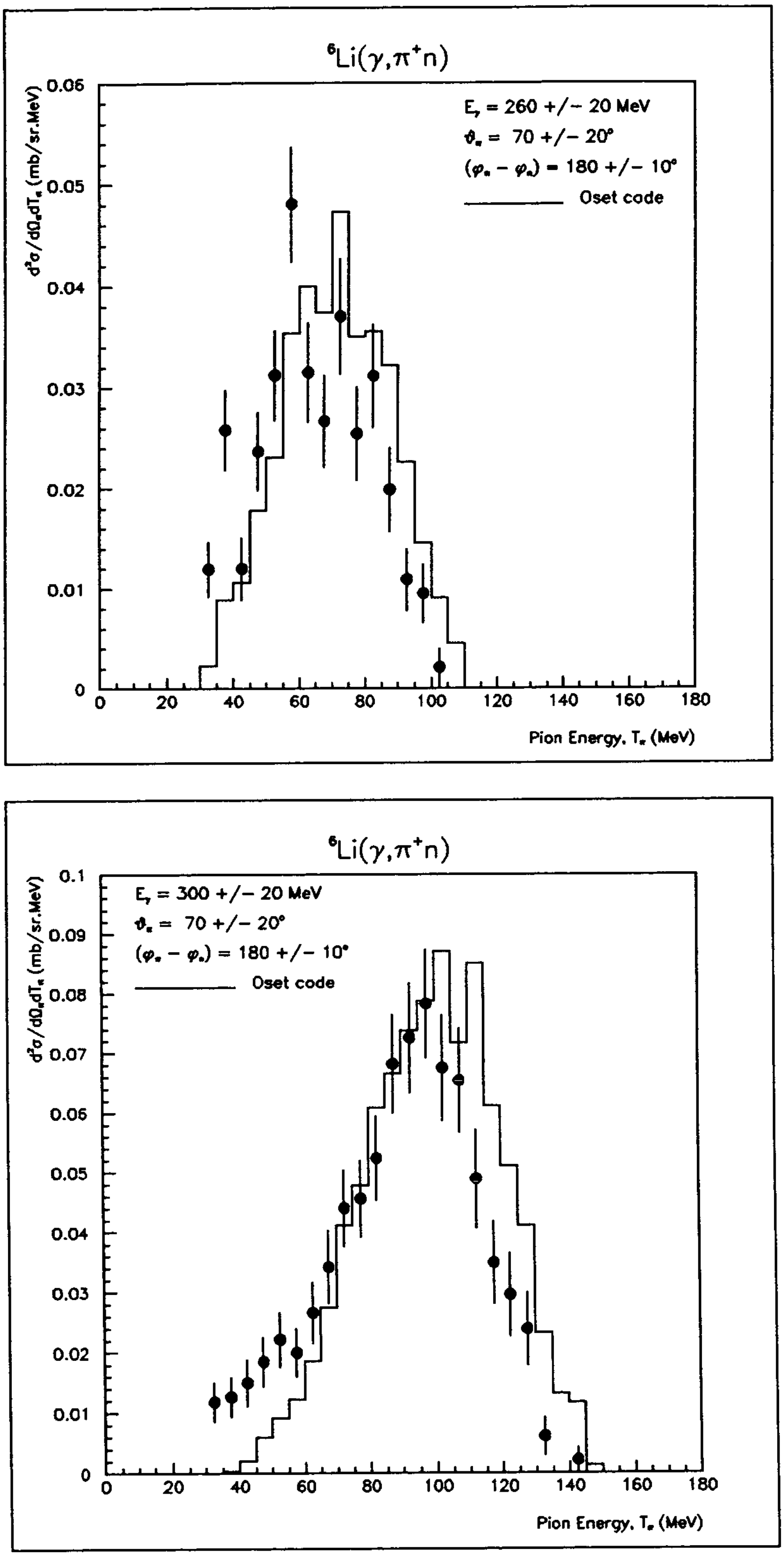

Figure 5.1: *Cross-sections for Lithium*

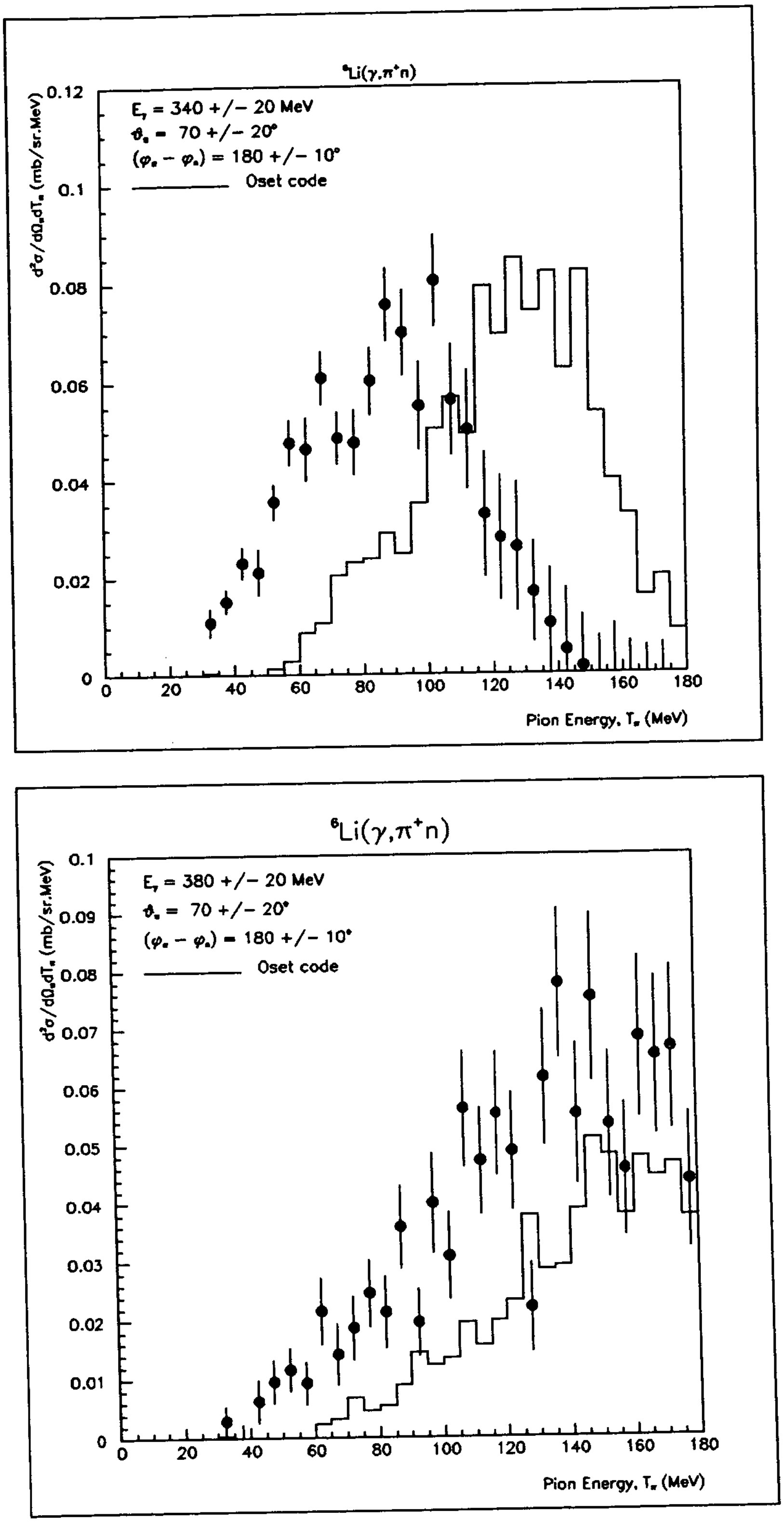

Figure 5.2: *Cross-sections for Lithium*

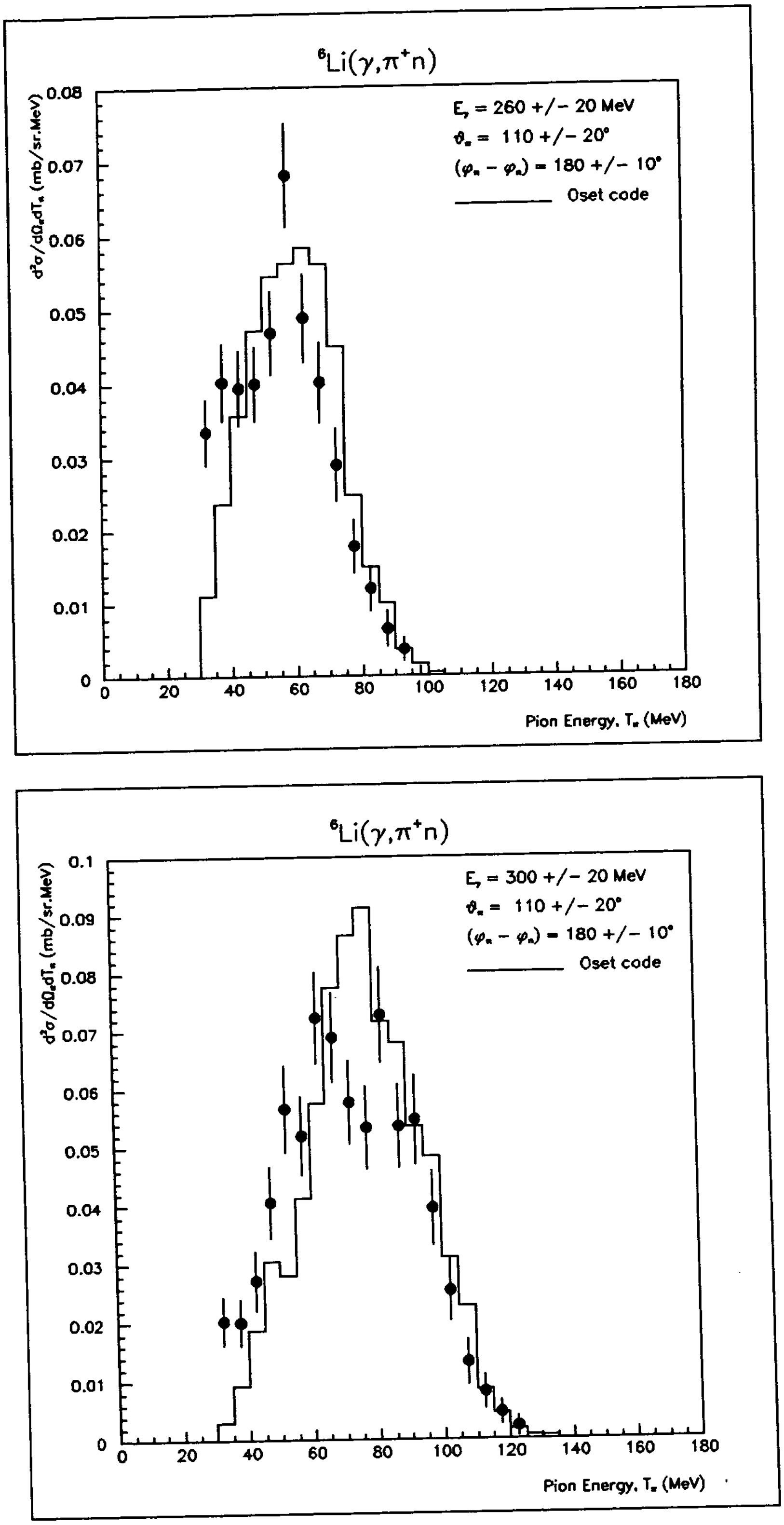

Figure 5.3: *Cross-sections for Lithium*

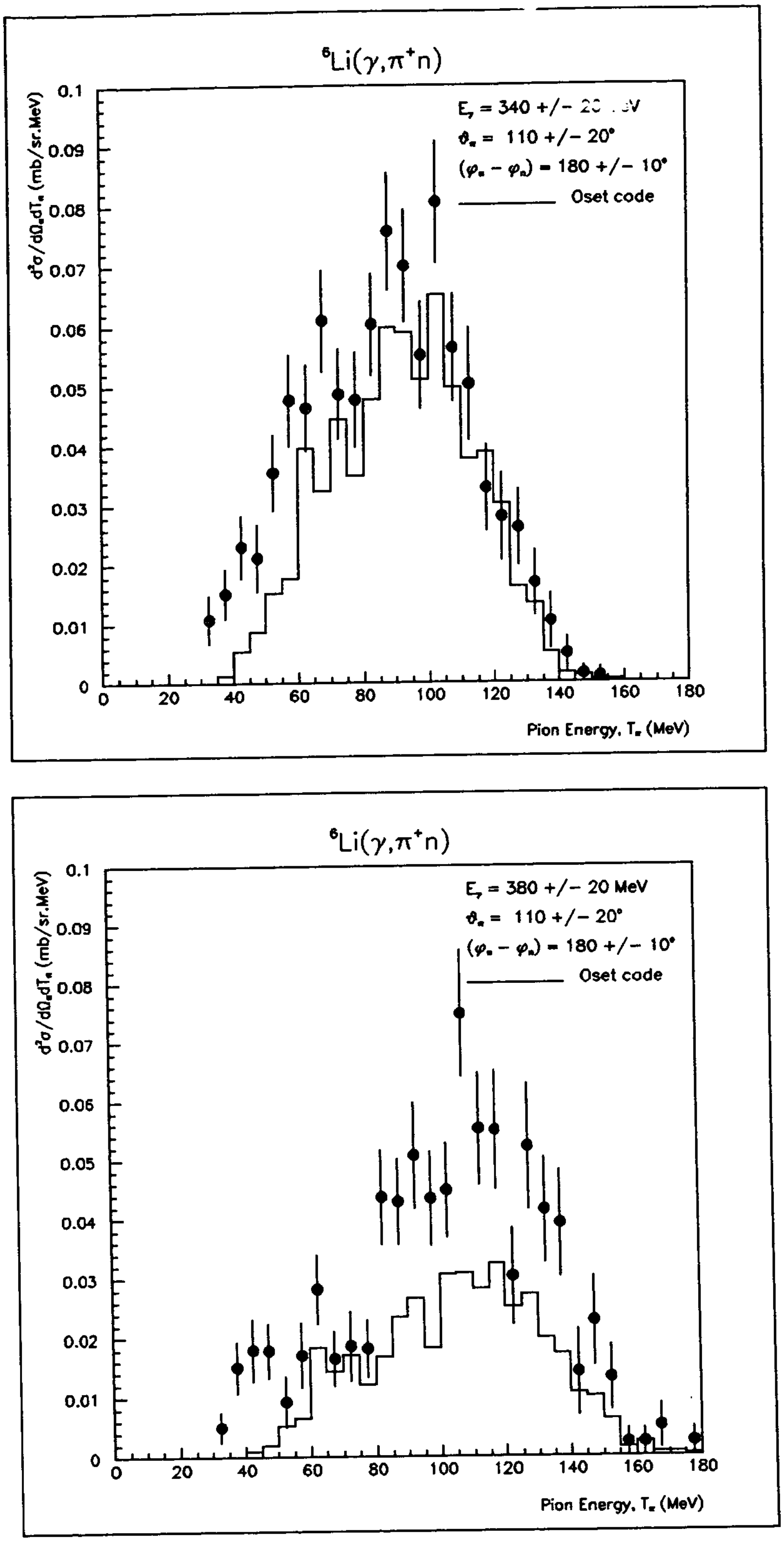

Figure 5.4: *Cross-sections for Lithium*

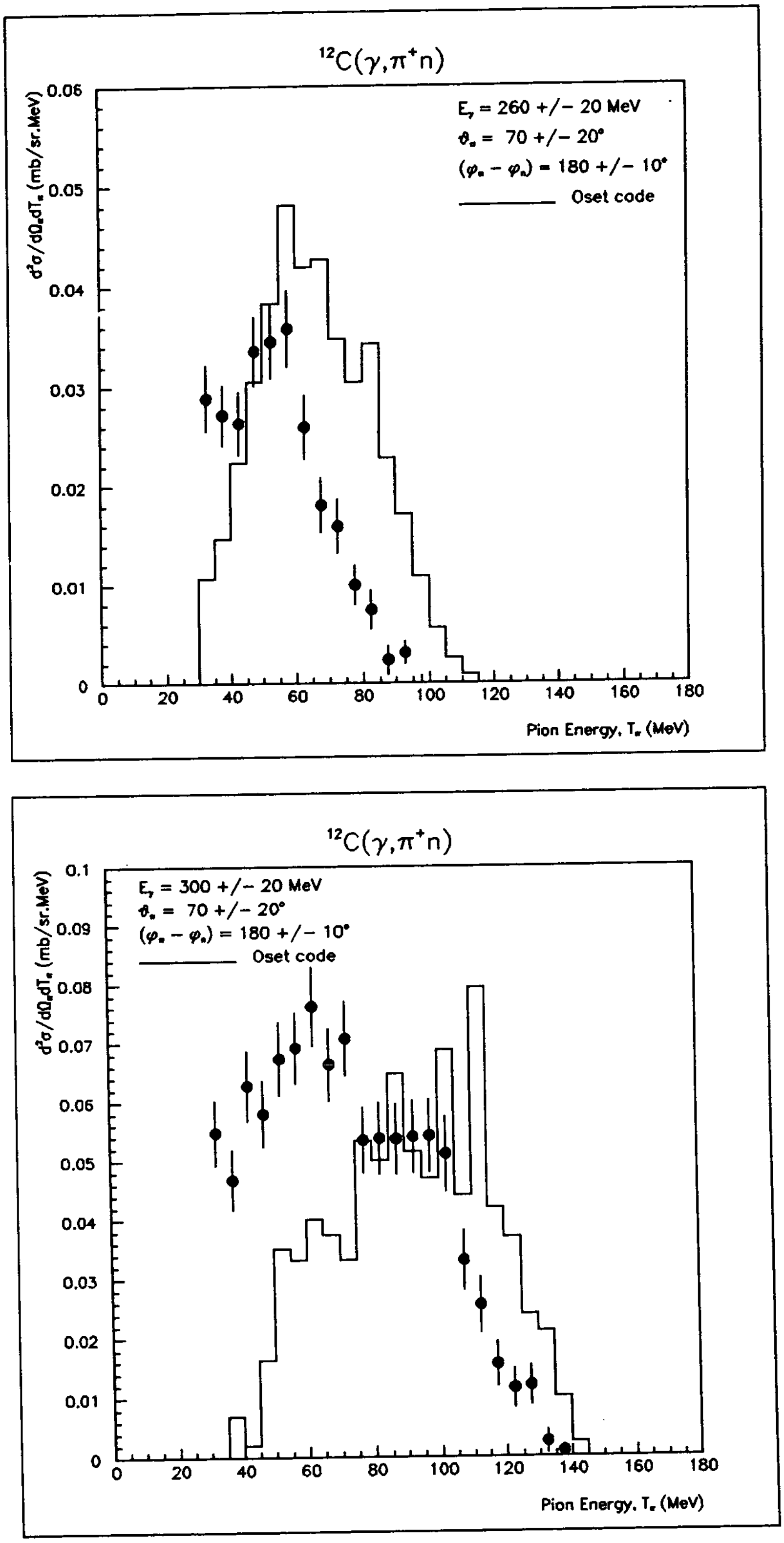

Figure 5.5: *Cross-sections for Carbon*

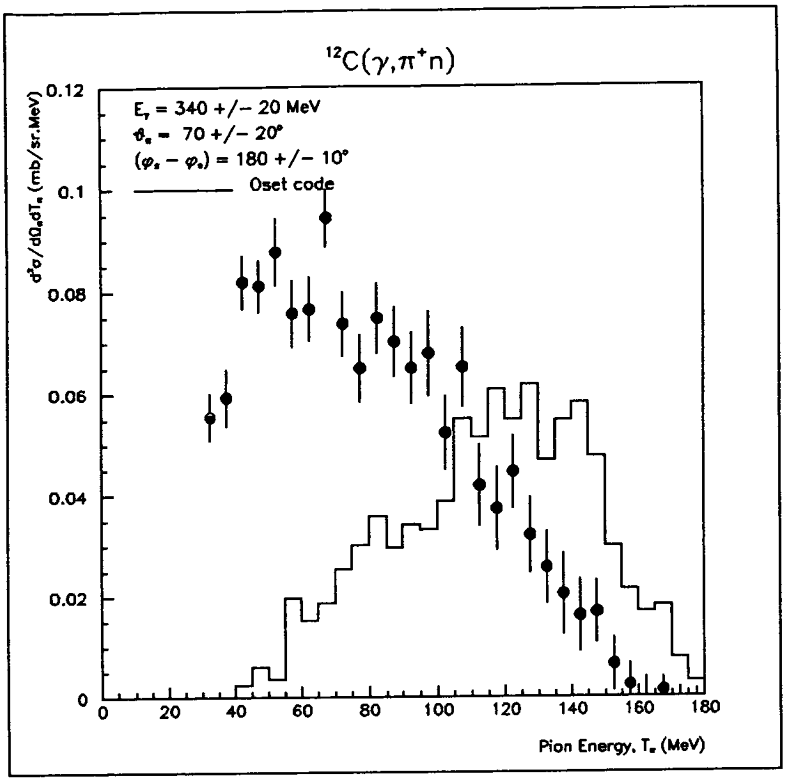

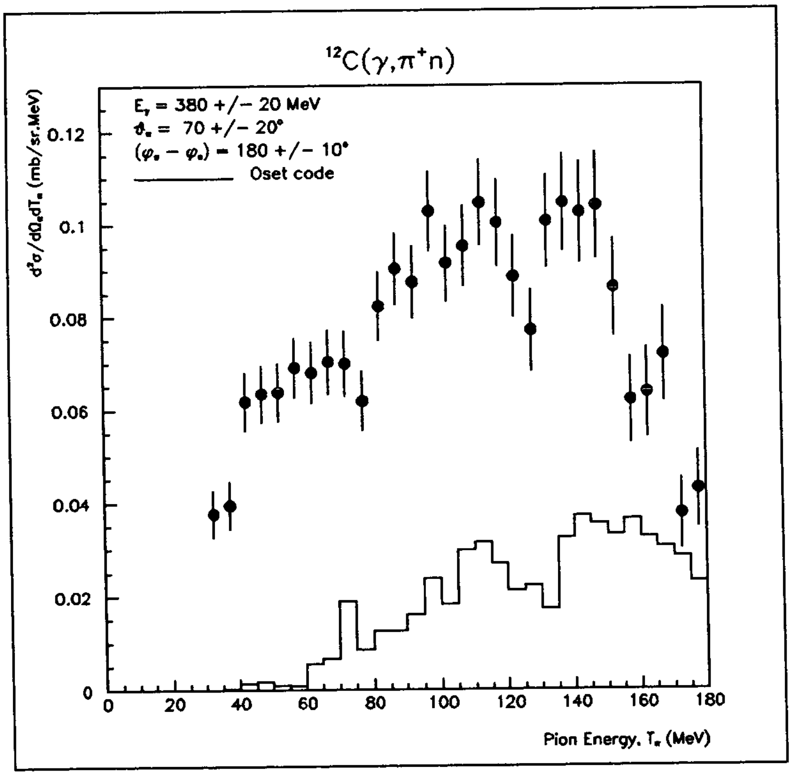

Figure 5.6: *Cross-sections for Carbon*

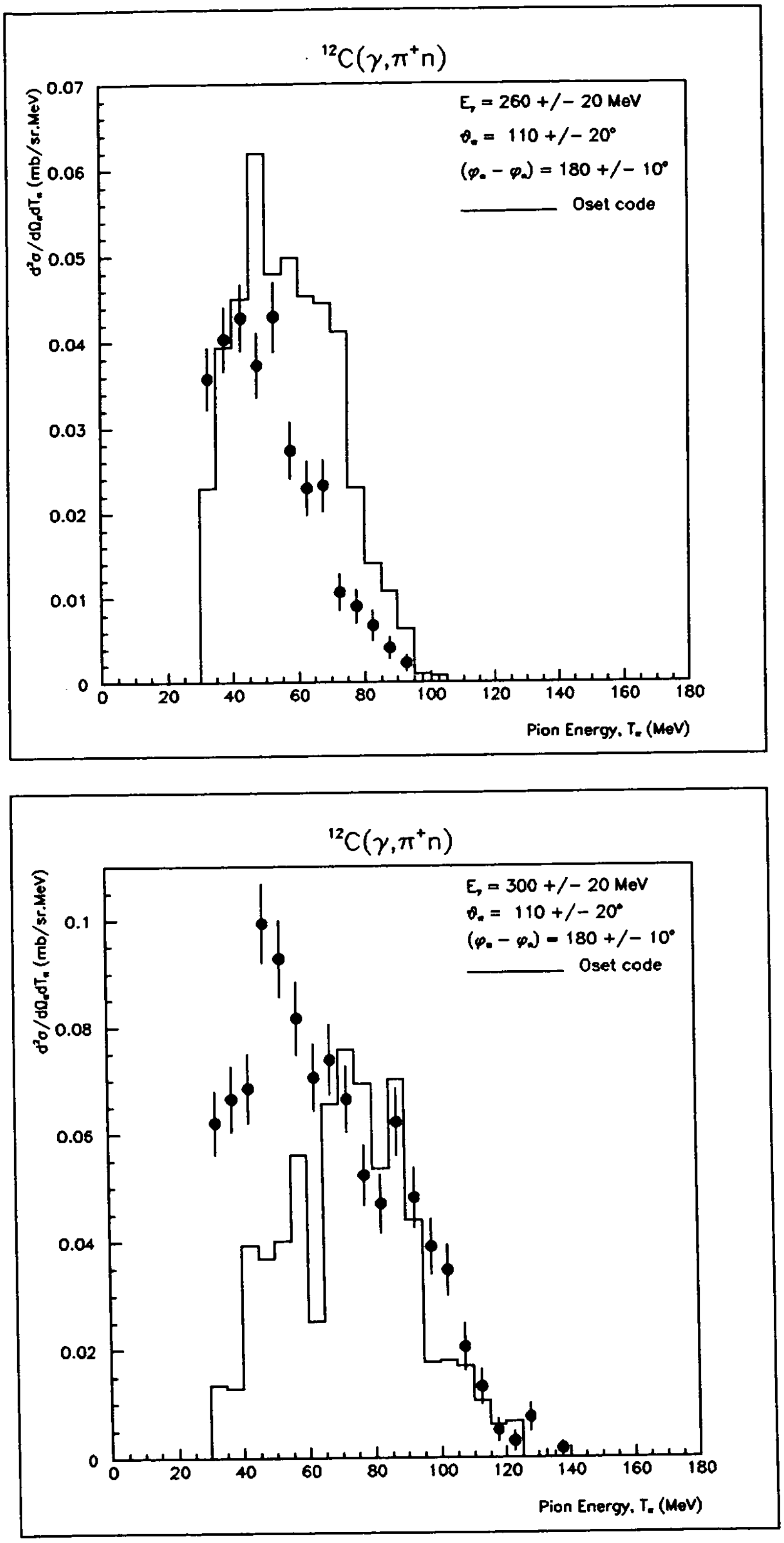

Figure 5.7: *Cross-sections for Carbon*

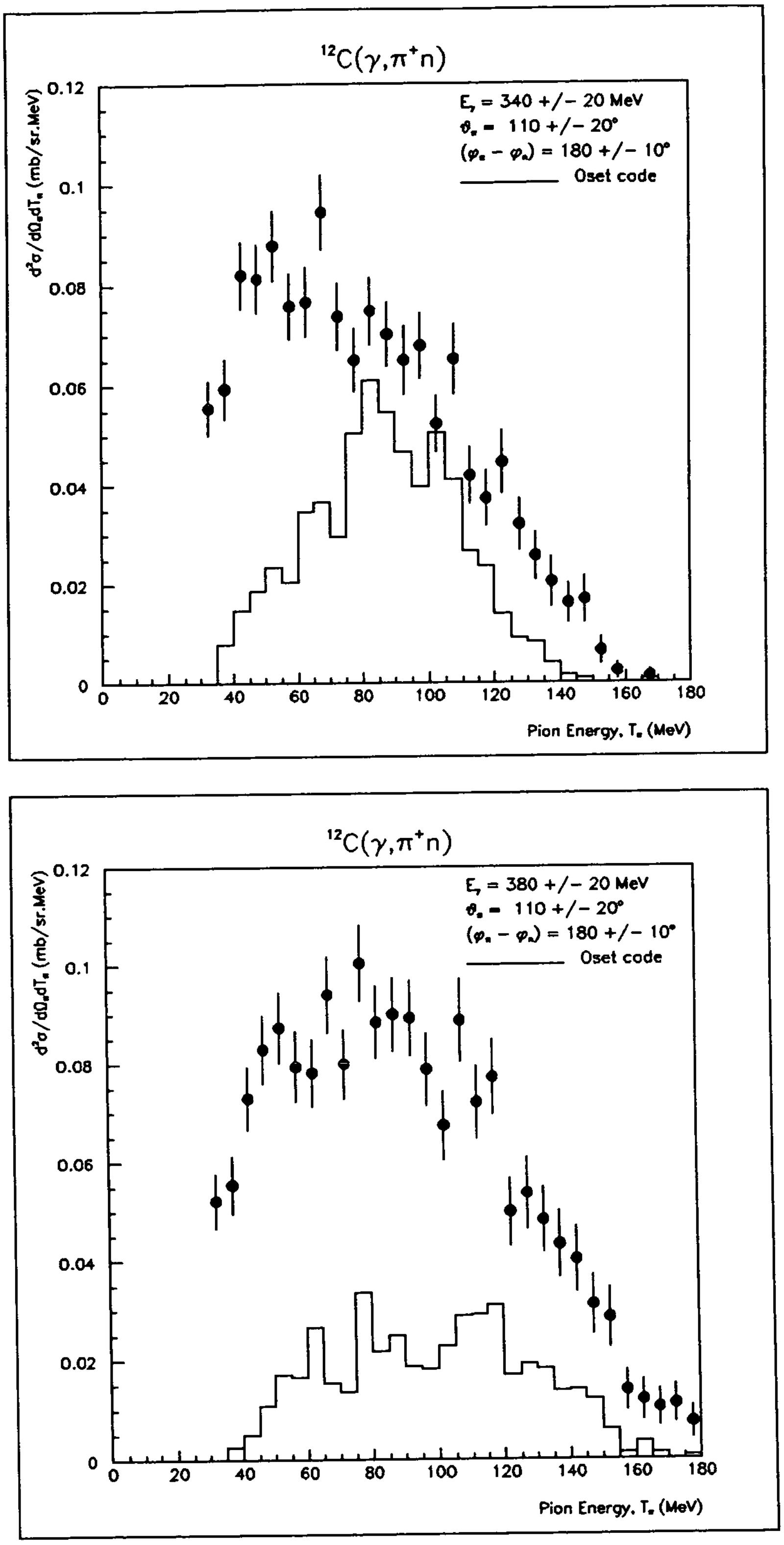

Figure 5.8: *Cross-sections for Carbon*

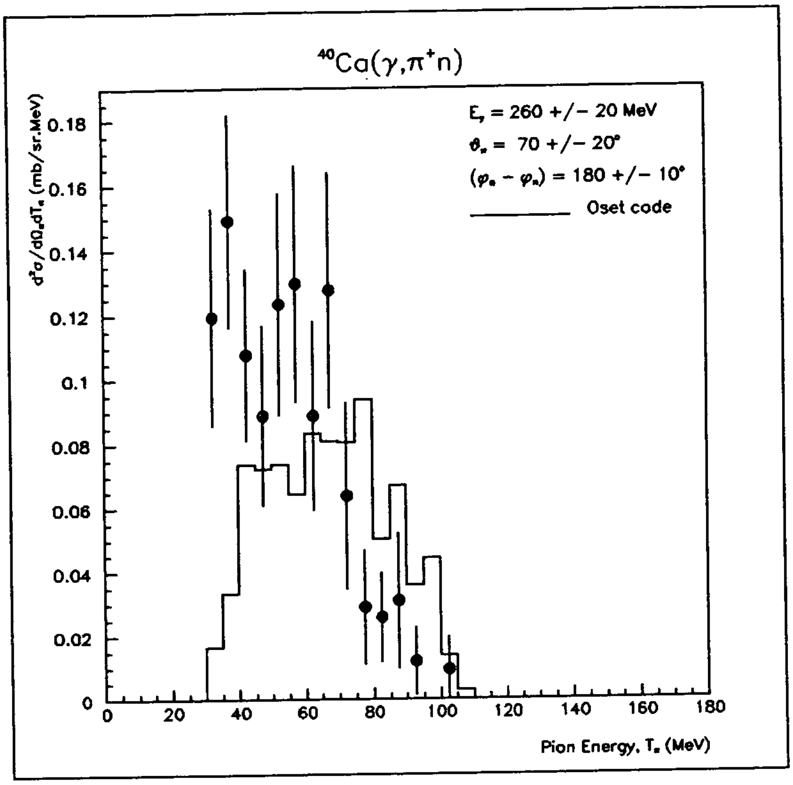

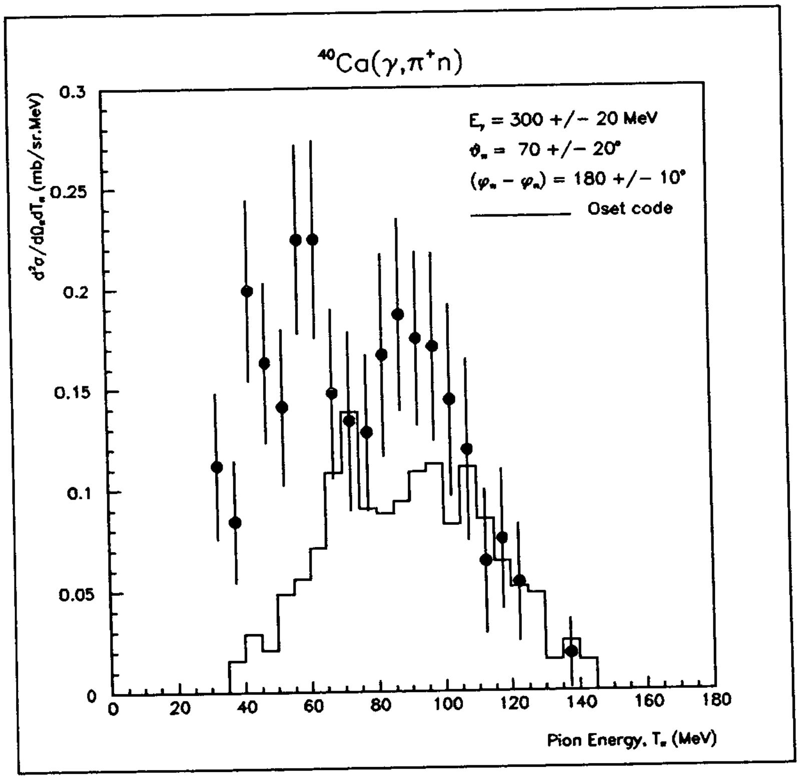

Figure 5.9: *Cross-sections for Calcium*

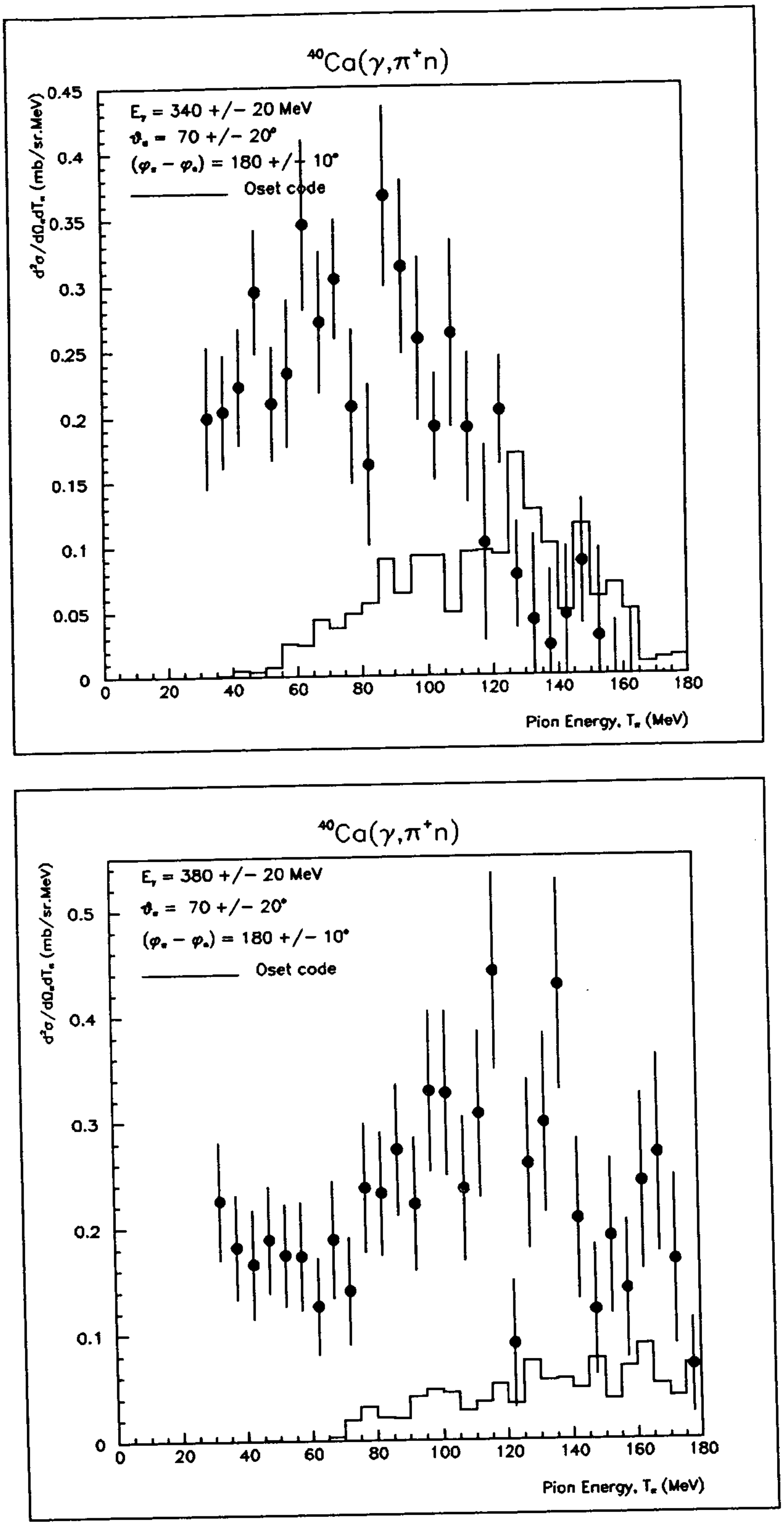

Figure 5.10: *Cross-sections for Calcium*

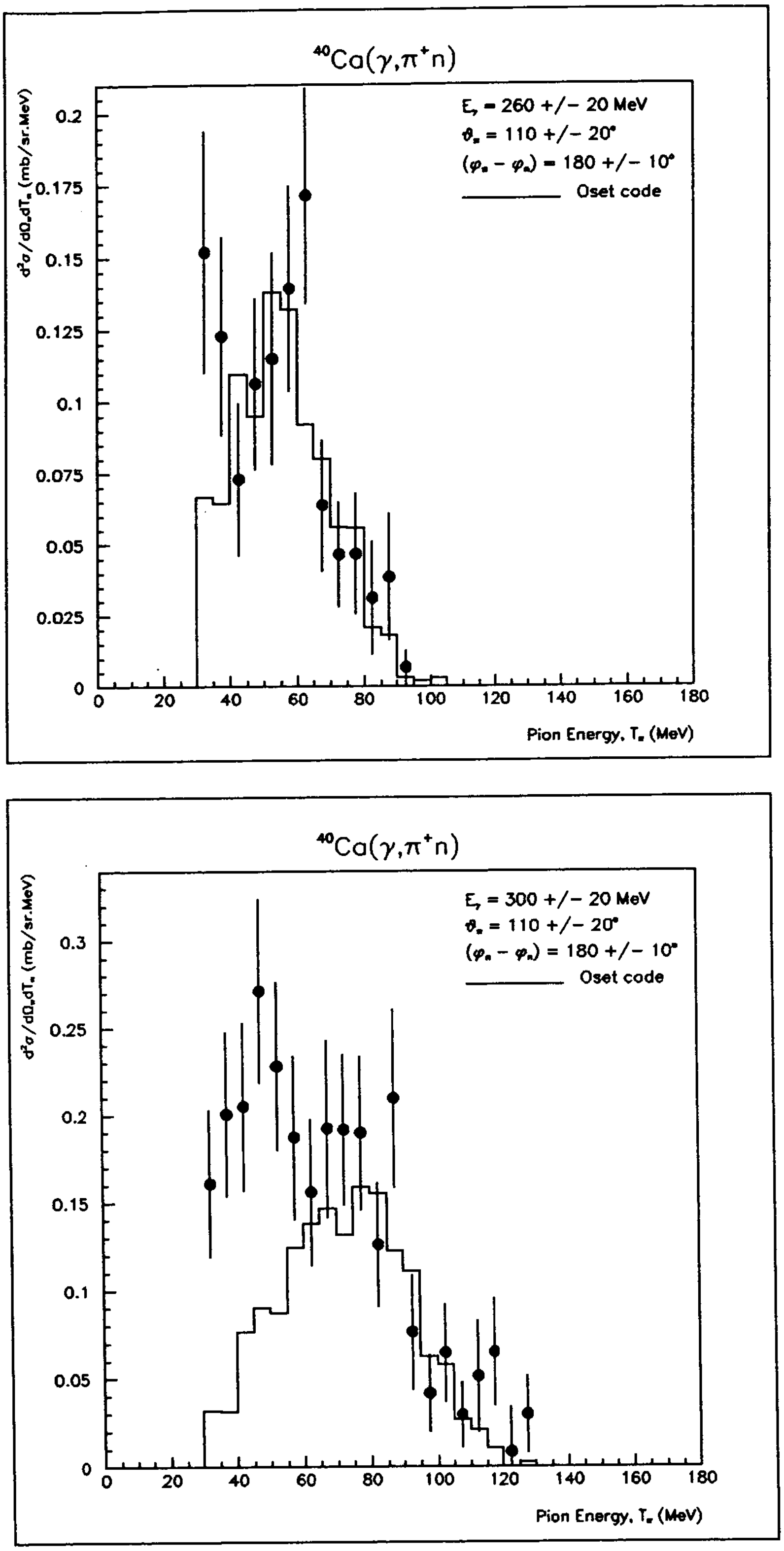

Figure 5.11: *Cross-sections for Calcium*

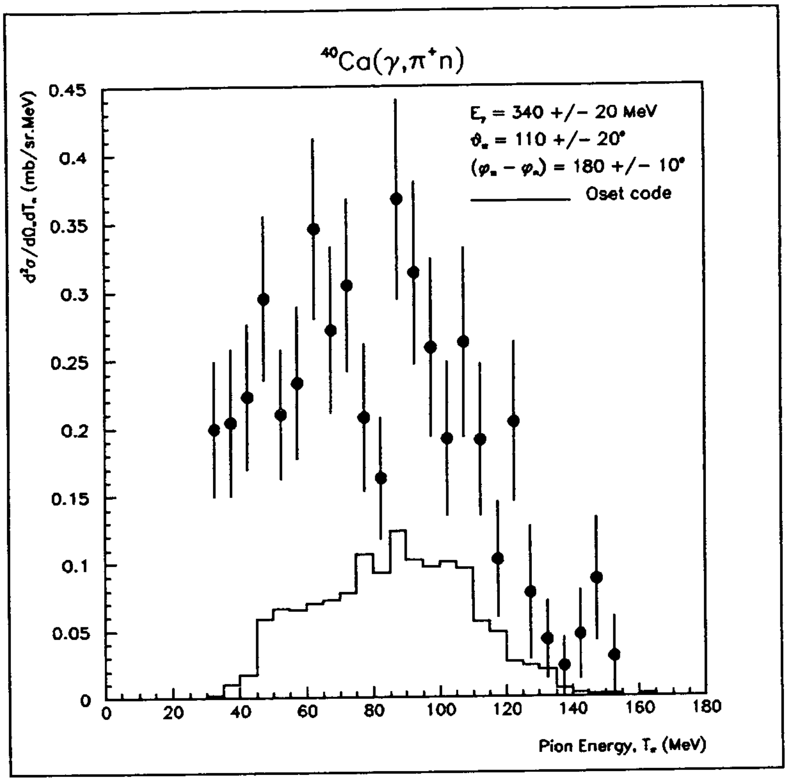

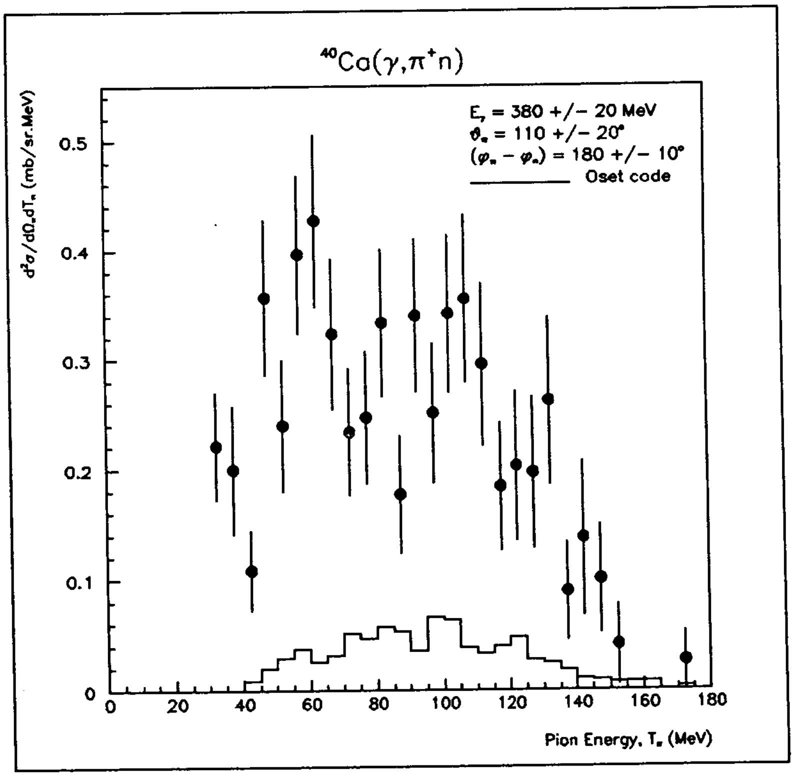

Figure 5.12: *Cross-sections for Calcium*

5.2.1 Lithium

The first thing to notice about the comparison of the Lithium data with the calculations made using the Oset *et al.* code is that there is good agreement indeed. At low photon energies (E_γ = 260 and 300 MeV), the shapes of the cross-sections as well as the magnitudes are reproduced to a considerable degree of accuracy. At E_γ = 340 MeV, the shapes of both forward and backward angle cross-sections are well reproduced but now the magnitudes of the theory are slightly lower than the data. Even at the highest energies the cross-section shapes are faithfully reproduced. At E_γ = 380 MeV however, one can see the magnitude of the theoretical code dropping away from the data considerably. Apart from this high energy effect though, the Lithium data and the theory are well matched.

It was thought before analysis that the Lithium data might compare least favourably with the theoretical predictions of Oset *et al.*. This was because of a combination of the lack of nuclear structure inherent in the theoretical code and the unique structure and highly deformed shape of the Lithium nucleus. This has not proven the case, and the good agreement between the Lithium data and the code is encouraging.

5.2.2 Carbon

The Carbon data has some additional interesting features in comparison with the calculations of the theory code. The first thing to notice is the offset (most noticeable at E_γ = 260 MeV) between the data and theory. That is, at the higher pion energies, the data and theory have similar shapes but the theory's shape is shifted along the x-axis to higher values by $\sim$ 30 MeV. As mentioned in the last chapter, this is due to the lack of nuclear structure in the Oset code. This effect shows up more in the Carbon data than either of the other targets. It is thought that this occurs because of the very strongly defined shell structure which is apparent in the Carbon missing energy spectrum (figure 4.6) which shows a much sharper peak than the other targets. As discussed in chapter 4, we have integrated over the missing energy range hoping to obtain the correct shape of the cross-section. In general, this has worked since the shapes of the calculated cross-sections follow the data fairly well with one noticeable exception. At low pion energies, the theory appears to considerably underestimate the cross-section. The theoretical predictions for higher energy pions fit the shape of the data well but there is a large discrepancy up to $T_\pi \sim 60$ MeV. The other feature to notice is the difference in the magnitudes of the theory and the data cross-sections at high E_γ. For the highest photon energy range ($E_\gamma = 380$ MeV), the data is greater than the code by a factor of three.

5.2.3 Calcium

The comparison between the Calcium data and the theoretical calculations shows the least agreement of the three targets. Many of the trends mentioned earlier can be seen to be continuing in the Calcium data. In the low photon energy spectra the code again underestimates the low energy pions but fits the high energy pions' shape well. This is clearly an extension of the feature seen in Carbon.

Similarily, the theory underestimates the overall magnitudes of the cross-sections at high E_γ. At low photon energies, the higher pion energy data shows fairly good agreement with the theory, but at the highest photon energy ($E_\gamma = 380$ MeV), the data is greater than the theoretical code by a factor of seven or eight. Despite this the overall shapes are reproduced reasonably well. These trends are discussed fully in the next section, with possible reasons and explanations being put forward.

5.3 Features of the Results

The results have been described in the previous section, now we must look more closely at them and analyse them thoroughly. Firstly, we shall look at some of the underlying trends in the presented data and theory. We must then find reasons for these features both in relation to each other, and compared with previous experimental and theoretical results.

The first tendency shown in the results is for the data to exceed the theoretical predictions for increasingly higher photon energies. For all three targets, the lower photon energy plots (E_γ = 260 and 300 MeV) show good agreement between data and theory. As photon energy increases, the theoretical code of Oset begins to fall short of the data points. This increases, so that at the highest E_γ the code is consistently lower than the data.

To highlight this trend, graphs were plotted of integrated cross-section versus photon energy for each target. Figure 5.13 shows that for Lithium the agreement between data and theory is very good at low E_γ but diverges at higher E_γ. Both data and theoretical cross-sections do show similar behaviour at all energies though, with the cross-section decreasing at E_γ = 380 MeV, beyond the Δ resonance region. This is not the case for Carbon (figure 5.14). Again, at lower E_γ the agreement is reasonable, but at higher E_γ, where the theoretically predictioned cross-section decreases, the data cross-section continues to rise. This is a feature which continues for the Calcium target (figure 5.15). Here again the data continues to rise and the theory falls at higher photon energies.

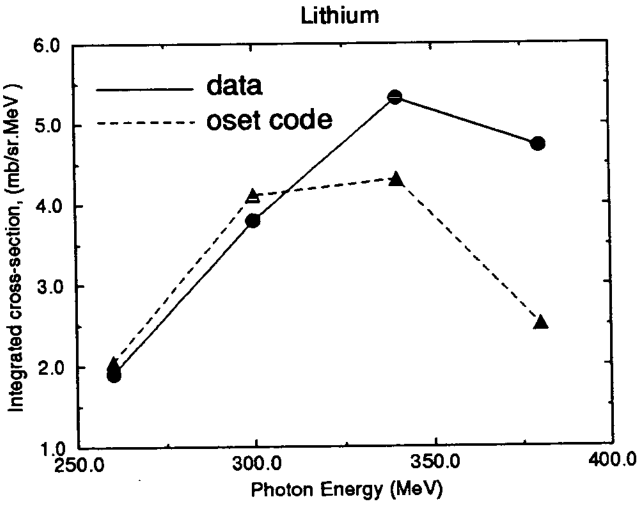

Figure 5.13: *Integrated Cross-section vs Photon energy*

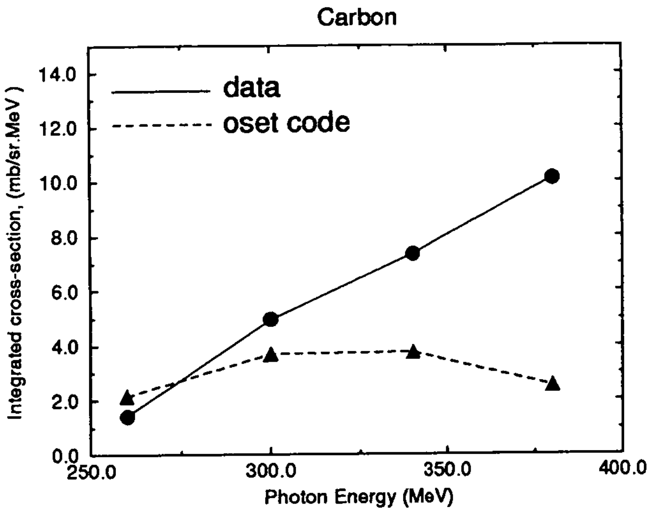

Figure 5.14: *Integrated Cross-section vs Photon energy*

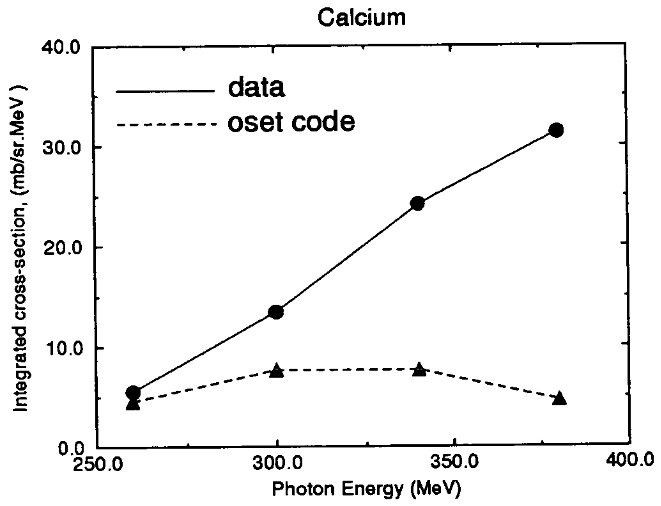

Figure 5.15: *Integrated Cross-section vs Photon energy*

An even more noticeable trend in the results, and the one on which most attention will be focussed, is that of the increasing divergence between the data and the theoretical code for increasing mass of the target, A. Plots of integrated cross-section versus target mass A for each of the four photon energy ranges are shown in figures 5.16 to 5.19.

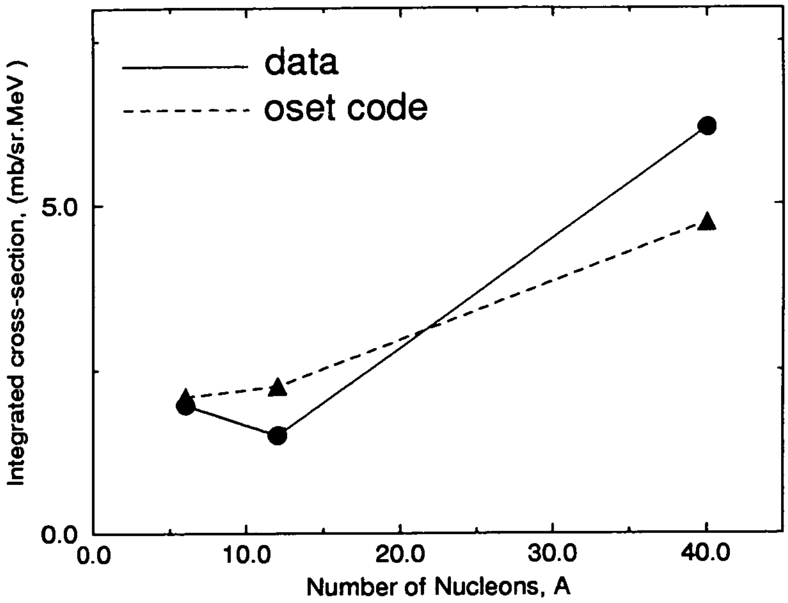

Figure 5.16: *A dependence for 240 MeV < E_γ < 280 MeV*

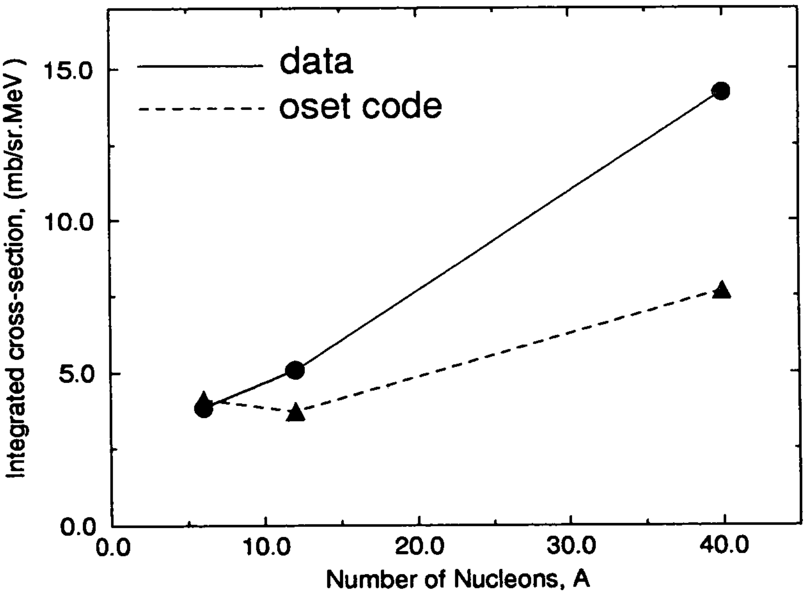

Figure 5.17: *A dependence for 280 MeV < E_γ < 320 MeV*

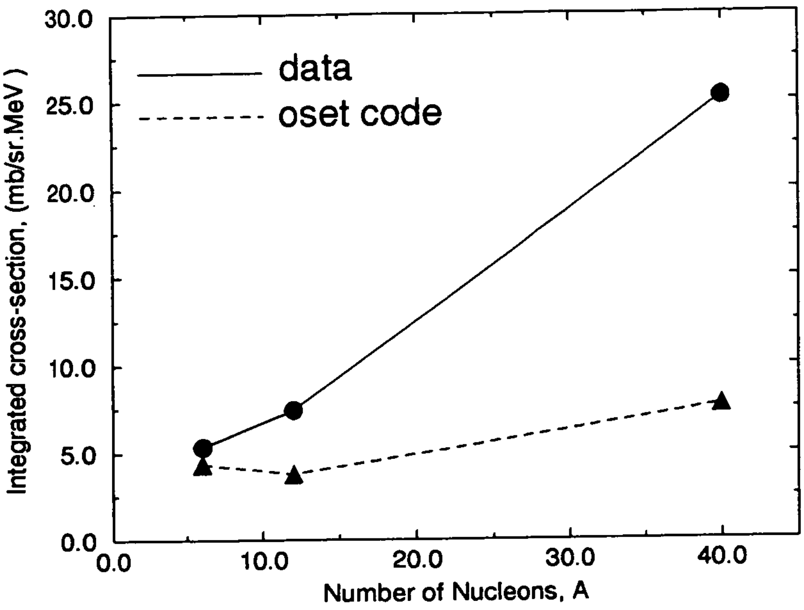

Figure 5.18: *A dependence for 320 MeV* $< E_\gamma <$ *360 MeV*

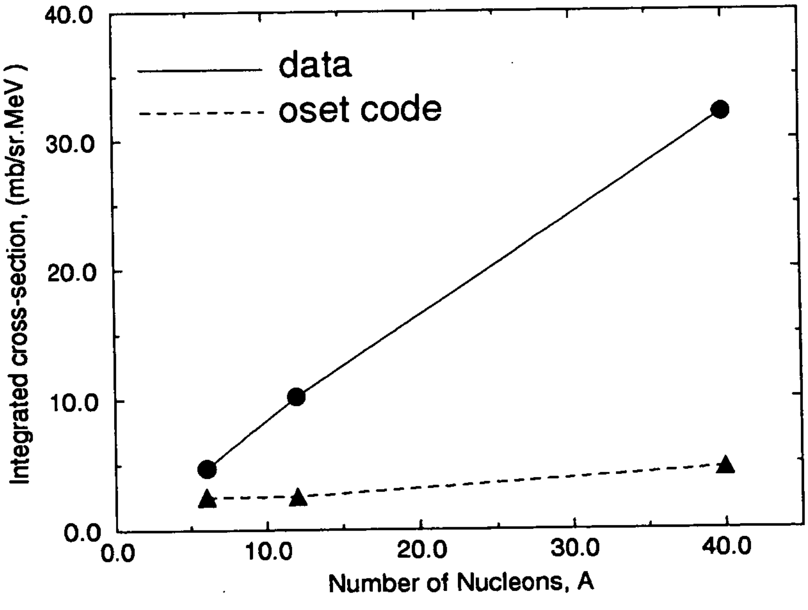

Figure 5.19: *A dependence for 360 MeV* $< E_\gamma <$ *400 MeV*

These plots consistently show a roughly linear dependence on A for the data cross-sections. This is clearly not the case for the theoretical cross-sections, especially at high photon energies. In general, the theory predicts the Lithium cross-sections well, with the greatest difference at the highest photon energies where the data is a factor of 1.5 or 2 times larger than the theoretical code. One can see looking at the Carbon data that at higher E_γ the discrepancy is considerably larger, with the data 3 times larger than than the code. This trend is continued for Calcium, where there is a large difference between the magnitudes of the data and theory cross-sections at high E_γ. The highest photon energy range (E_γ = 380 MeV) shows the data being a factor 7 or 8 times larger than the theoretical predictions. This is indeed a striking difference.

We must now look carefully at the make-up of the theoretical predictions used here. The theoretical work done by Carrasco and Oset is a microscopic approach. They include all the elementary interactions between nucleons, mesons and isobars. In this theory, they can distinguish between direct absorption, where a photon is initially absorbed on a nucleon and thus excites it; and indirect absorption where a photon is absorbed on a nucleon followed by the emission of a pion which then excites one or more nucleons by being reabsorbed later in final state interactions. They also include the possibility of pion rescattering inside the nucleus. In their paper [Car92b] they predict that for increasing A in the (γ,π) reaction, the indirect absorption begins to dominate (even to the extent of this type of absorption having a mass dependence $\sim$ $A^{1.24}$). Essentially their theory predicts overwhelming pion reabsorption and rescattering as final state interactions for targets with large A. This is borne out in the calculations used in this thesis. The effect of these final state interactions (pion rescattering, pion absorption etc.) increases in the code considerably with increasing photon energy and A. The smaller target of Lithium has a relatively low number of particles affected (in the region of $\sim$ 25%). This increases for Carbon to $\sim$ 40% and in the case of the Calcium target as many as 60% of particles undergo some form of final state interactions at high E_γ. This could go some way to explaining the difference between the theoretical calculations and the data presented here. Indeed, this is a possible explanation for the difference in the cases of Carbon and Calcium between the data and theory for pions of low energy. The theory predicts a much smaller cross-section for such pions compared to the data, and this ties in with the large amount of pion reabsorption and rescattering which is present in the theoretical calculations.

More light can be shed on this problem by examining the work of Arends *et al.* [Are91]. For single arm (γ,π^+) measurements, Arends *et al.* found a mass dependence of $A^{0.6}$. They suggested that this value could be attributed to the photon absorption being a volume effect (as expected) but with strong FSI taking place and many of the pions being reabsorbed inside the nucleus. The data presented here, however, shows a roughly linear dependence on A for the (γ,π^+n) reaction. This contradicts the results of Arends *et al.* and would suggest much less severe pion absorption and rescattering is involved in these reactions than was previously thought. The comparison is not a direct one since the Arends *et al.* value for A dependence is based on single-arm measurements, but one would expect similar trends to apply in both cases.

As well as this single-arm data, some coincidence results were also obtained during the same set of experiments [Are91]. This coincidence data, though small, does perhaps show one similarity to the current data. Their ^{16}O(γ,pπ) results are compared to a theoretical code PICA, which includes FSI in its calculations. The results clearly show the data exceeding these theoretical predictions for higher photon energies. At energies of E_γ = 390 MeV the Oxygen data is a factor 3 or 4 larger than the PICA code. Since the exact formulation of the FSI in the PICA intranuclear cascade code is not known, one must of course be wary of comparison. However further investigation into specific πN coincidence data would surely be of great interest in establishing the extent of FSI at higher energies, as well as higher A values.

If it should turn out that the probabilities for FSI are not particularily over-predicted by the code then one would have to look to medium modifications of the initial photon absorption process. Exciting possibilities are that the basic p(γ,π^+) reaction amplitudes could be increased in a nuclear medium; or that the dominant process becomes absorption onto nucleon pairs. There is also the possibility that collective effects could be present, giving rise to an initial absorption cross-section that varies as A^2. Answers to these questions will come about by studying a wider range of reaction channels.

A final comparison with previous data can be done here by looking at the work of Pham *et al.* at MIT-Bates [Pha92]. Their results were for ^{16}O(γ,π^-p) at $E_\gamma = 360$ MeV. The data were compared to a DWIA theoretical code at pion angles $\theta_\pi = 64°$ and 120°. The data showed good agreement with the theory at the backward angle but was a factor 3 smaller than the theory at the forward pion angle. The theory predicted similar magnitudes of cross-section for both angles, whereas the forward angle data was 3 times lower than the backward angle data.

Examining the results in this thesis, there is no indication of a similar phenomenon in the current data. For all targets at all photon energies the magnitudes of the data cross-sections are similar in size. This is also the case for the predicted theoretical cross-sections of the Oset *et al.* code. Thus, these results would appear to cast considerable doubt on the Pham *et al.* results in that no sign of a strong angular dependence on the cross-section for (γ,π^+n) is observed.

5.4 Conclusions

Some conclusions as to the success of the current work will be drawn in this final section. Both my own work and its part in the MAMI-B collaboration will be discussed and assessed.

The results in this thesis are among the first to come out of the recent PiP-TOF collaboration between the Universities of Edinburgh, Glasgow and Tübingen. This collaboration is an ongoing concern and the results presented here were obtained during an initial teething time for the experimental work at Mainz. It is believed that most problems have been ironed out and the scope for future work is great.

It has been shown that the PiP-TOF-Tagger detector set-up can effectively measure such photonuclear reactions to a reasonable degree of accuracy. The success of PiP in detecting postive pions is of special importance. Some improvements are still possible, with the development of polarised photons beams hopefully providing even greater choice of experiments.

The current data set is comprehensive, with some wide-ranging analysis being carried out on it to investigate many different reactions, including (γ,π^+p). The π^+p reaction channel is of particular interest in comparison with the π^+n data presented here with a view to furthering our understanding of FSI. Unfortunately such analysis is at a tentative stage, and currently outwith the scope of this thesis.

The data is not without its own problems though. In retrospect, more time spent on the Calcium target (and to a lesser extent, the Lithium target) would have certainly been advantageous in improving statistics. Similarily in the future one would look forward to results from studies of other varied targets with a wider spread of A values.

The data in this work has thrown up some interesting questions. The comparison with theoretical code of Oset *et al.* has been extremely useful, with the effectiveness of this being discussed in the previous section. Obviously more work needs to be done, both with Oset and other theorists to attempt to fully explain the processes involved inside the nucleus. The results here also cast doubt on previous experiments which found a large difference between the magnitudes of forward and backward angle results. More work could be done on this also.

In conclusion, I believe this work is of considerable importance and interest within the field of photonuclear physics. Hopefully it will provide a useful building block in the work between experimentalists and theorists as they try to further their understanding of the workings of the nucleus in photonuclear reactions.

Bibliography

[Ana76] P. S. Anan'in, I. V. Glavanokov *et al.*, *JETP* 23 (1976) 298

[Ana82] P. S. Anan'in *et al.*, *Sov. J. Nucl. Phys.* 36 (1982) 170

[Ana84] P. S. Anan'in *et al.*, *Sov. J. Nucl. Phys.* 39 (1984) 1

[Ana90] P. S. Anan'in and I.V. Glavanokov, *Sov. J. Nucl. Phys.* 52 (1990) 205

[Ann93] J.R.M. Annand and B. Oussena, *NIM* A330 (1993) 220

[Ann] J.R.M. Annand, I. Anthony and A. Sibhald, *ACQU Manual, Kelvin Lab Report*

[Ant91] I. Anthony *et al.*, *NIM* A301 (1991) 230

[Are82] J. Arends *et al.*, *Z. Phys. A* 305 (1982) 205

[Are91] J. Arends *et al.*, *Nucl. Phys. A* 526 (1991) 479

[Ber67] Berends, Donnachie, Weaver, *Nucl. Phys. B* 4 (1967) 54

[Ber] W. Bertozzi *et al.*, *Modern Topics in Electron Scattering*

[Bet68] C. Betourne *et al.*, *Phys. Rev.* 172 (1968) 1342

[Blo77] I. Blomqvist and J. M. Laget, *Nucl Phys. A* 280 (1977) 405

[Bra91] D. Branford (Ed.), *Future Detectors for Photonuclear Experiments* (1991)

[Car92a] R. Carrasco and E. Oset, *Nucl. Phys. A* 536 (1992) 445

[Car92b] R. Carrasco and E. Oset, *Nucl. Phys. A* 541 (1992) 585

[Car92c] R. Carrasco and E. Oset, *Phys. Rev. C* 45 (1992) 764

[Car94] R. Carrasco and E. Oset, *Nucl. Phys. A* 570 (1994) 701

[Cec79] R.A. Cecil *et al.*, *NIM* 161 (1979) 439

[Cha77] N.S. Chant and P. Roos, *Phys. Rev. C* 15 (1977) 15

[Che57] Chew, Low, Goldberger and Nambu, *Phys. Rev.* 106 (1957) 1345

[Cra70] R.L. Craun and D.L. Smith, *NIMS* 80 (1970) 239.

[Cro94] G.E. Cross, *PhD Thesis*, University of Glasgow, 1994

[Die90] A.E.L. Dieperink and P.K.A de Witt Huberts, *Annual Review of Nuclear and Particle Physics* Vol 40 (1990) 239

[Gla79a] I. V. Glavanokov, *Sov. J. Nucl. Phys.* 29 (1979) 746

[Gla79b] I. V. Glavanokov, *Sov. J. Nucl. Phys.* 30 (1979) 465

[Gla89] I. V. Glavanokov, *Sov. J. Nucl. Phys.* 49 (1989) 58

[Hal90] S.J. Hall and G.J. Miller, *Kelvin Lab Annual Report*

[Hym90] S.D. Hyman *et al.*, *Phys. Rev. C* 41 (1990) R409

[Koc84] J. H. Koch, E. J. Moniz, N. Ohtsuka, *Annals of Physics* 154 (1984) 99

[Li93] X. Li and L. E. Wright, *Phys. Rev. C* 48 (1993) 816

[Mac95] J. A. Mackenzie, *PhD Thesis* University of Edinburgh 1995

[Nag91] A. Nagl, V. Devanathon, H. Überall, *Nuclear Pion Photoproduction* (1991)

[Ose79] E. Oset, W. Weise, *Nucl. Phys. A* 319 (1979) 477

[Ose82] E. Oset, H. Toki, W. Weise, *Physics Reports* 83 (1982) 281

[Ose87] E. Oset, *Nucl. Phys. A* 468 (1987) 631

[Owe94] R. O. Owens, *private communication*

[PAW] PAW - Physics Analysis Workstation, *CERN Program Library entry Q121*

[Pha92] L. D. Pham *et al.*, *Phys. Rev. C* 46 (1992) 621

[Ran90] R.D. Ransome *et al.*, *Phys. Rev. C* 41 (1990) 1500

[Smi89] L.C Smith *et al.*, *Phys. Rev. C* 40 (1989) 1347

[Ste90] M. Steinacher *et al.*, *Nucl. Phys.* A517 (1990) 413

[Sat93] T. Sato and T. Takaki, *Preprint* (1992)

[Wal89] P. Wallace, *Ph.D Thesis*, University of Glasgow, 1989.

[Wat54] K. Watson, *Phys. Rev.* 95 (1954) 228